

POLITECNICO DI TORINO

Master of Science in
Environmental and Land Engineering

Master of Science Thesis

**Zerovalent iron nanoparticles for groundwater remediation:
characterization, transport tests and numerical modeling**



Host institution:



Supervisors:

Dr. Tiziana Tosco

Dr. Carlo Bianco

External supervisors:

Dr. Jürgen Braun

Dipl.-Ing. Anke Wiener

Candidate:

Fabiano Maccari

March 2018

Declaration of Authorship

I hereby declare that this master's thesis is entirely my work except where otherwise indicated.
Passages and ideas from other sources are acknowledged as references.

Torino,

Signature_____

Abstract

In the last decades, the widespread use of chemical substances across Europe has caused a large groundwater contamination in many areas. Among the available remediation techniques, *in situ* approaches are often preferred, because they are safer for the people and more cost effective; however, they generally present some difficulties in targeting the contaminated zone. A rather recent remediation technology, namely injection of nanoscale zerovalent iron, has gained much attention because it allows a direct treatment of the contaminant source. This technique aims at depositing the zerovalent iron in the pore space of the aquifer to form a well-spread reactive zone, able to degrade harmful compounds. The possible applications have been studied in depth by the EU funded project *NanoRem*, of which the present thesis represents a follow-up.

During this research work the iron particle and suspension properties have been investigated, with the purpose of understanding how they were related to the colloidal stability and to the mobility in the porous media. The commercial product NANOFE STAR has been used, whose suspensions were stabilized by the addition of carboxymethyl cellulose, a polymer mainly used as thickener and binder in many industrial sectors; the role of this polymer in determining the properties of the suspensions has also been analyzed.

After this phase of particle and suspension characterization, which also included some properties of the porous medium such as zeta potential, a selected iron suspension has been used for the conduction of column tests; the choice was based on particle stability and size appraised during the previous tests. The objective of these experiments was to assess the mobility of the suspension and to comprehend the deposition mechanisms occurring in two porous media with different granulometry. For this purpose, the test results have been modeled with the software MNMs, through which a quantification of the deposition processes was possible.

Indeed, the evaluation of the previous tests via analytical and numerical modeling allowed a deeper comprehension and a quantification of the observed phenomena. In particular, the determination of the parameters regulating the deposition processes in the columns allowed to run radial injection simulations for a hypothetical single-well field application. These simulations can predict the iron distribution achieved during an injection and evaluate other important parameters, like the consequent rise in the pressures in the porous medium. In conclusion, since the radial simulation with the selected suspension did not provide satisfactory results in terms of spatial iron distribution, a way of improving the particle transport has been sought via modeling increasing the CMC concentration in the suspension.

Sommario

Negli ultimi decenni, l'utilizzo diffuso di sostanze chimiche in tutta Europa ha causato in diverse aree una vasta contaminazione delle acque di falda. Tra le tecniche di bonifica disponibili, gli approcci *in situ* sono spesso privilegiati, perché sono più sicuri per le persone e più convenienti dal punto di vista economico; tuttavia spesso presentano qualche difficoltà nell'intervenire in modo mirato sulla zona contaminata. Una tecnologia piuttosto recente, ovvero l'iniezione di ferro zerovalente nanoscopico, ha acquisito molto interesse in quanto permette un trattamento diretto della sorgente contaminante. Questa tecnica mira a depositare il ferro zerovalente nello spazio dei pori della falda acquifera per formare una zona reattiva ben distribuita, in grado di degradare i composti dannosi. Le possibili applicazioni sono state studiate in modo approfondito dal progetto *NanoRem*, di cui la presente tesi rappresenta una continuazione.

Nel corso di questo lavoro di ricerca sono state indagate le proprietà delle particelle e delle sospensioni di ferro, allo scopo di comprendere come esse fossero correlate alla stabilità colloidale e alla mobilità nei mezzi porosi. È stato utilizzato il prodotto commerciale NANOFER STAR, le cui sospensioni sono state stabilizzate con l'aggiunta di carbossimetilcellulosa, un polimero utilizzato principalmente come addensante e legante in molti settori industriali; è stato analizzato anche il ruolo di questo polimero nel determinare le proprietà delle sospensioni.

Dopo questa fase di caratterizzazione di particelle e sospensioni, in cui rientravano anche alcune proprietà del mezzo poroso come il potenziale zeta, una sospensione di ferro selezionata è stata impiegata per la conduzione di test in colonna; la scelta si è basata sulla stabilità e sulle dimensioni delle particelle determinate durante i test precedenti. L'obiettivo di questi esperimenti era valutare la mobilità della sospensione e comprendere i meccanismi di deposizione che si verificano in due mezzi porosi con differente granulometria. A tale scopo, i test sono stati valutati con il software MNMs, attraverso cui è stata possibile una quantificazione dei processi di deposizione.

In effetti, la valutazione dei test precedenti attraverso la modellazione analitica e numerica ha permesso una comprensione più profonda e una quantificazione dei fenomeni osservati. In particolare, la determinazione dei parametri che regolano i processi di deposizione nelle colonne ha permesso di eseguire simulazioni di iniezione radiale a pozzo singolo per un'ipotetica applicazione sul campo. Queste simulazioni possono prevedere la distribuzione del ferro ottenuta durante una iniezione e valutare altri parametri importanti, come il conseguente aumento delle pressioni nel mezzo poroso. In conclusione, poiché la simulazione radiale con la sospensione selezionata non ha fornito risultati soddisfacenti in termini di distribuzione spaziale del ferro, tramite modellazione è stato ricercato un modo per migliorare il trasporto di particelle aumentando la concentrazione di CMC nella sospensione.

Table of Contents

1. Introduction	1
1.1. Motivation: soil and groundwater pollution.....	1
1.2. The NanoRem project.....	2
1.3. The present master's thesis and its objectives	3
2. Overview of the main remediation techniques	7
2.1. Source-control measures.....	7
2.2. Pump and treat.....	8
2.3. Permeable Reactive Barriers	9
2.4. Nanoremediation with nanoscale zerovalent iron	10
3. Theoretical background.....	13
3.1. Chlorinated hydrocarbons	13
3.2. Remediation with zerovalent iron	15
3.3. Transport of nZVI.....	20
4. Materials and methods	37
4.1. Main materials used in the experiments	37
4.2. Instruments and procedures used in the experiments.....	44
4.3. The software MNMs	59
5. Results and discussion.....	67
5.1. Particle and suspension characterization	67
5.2. Porous medium properties.....	82
5.3. Properties of CMC solutions	86
5.4. NANOFER STAR column tests	95
5.5. Modeling with MNMs.....	105
6. Conclusions	127
Appendix A.....	131
References	139

List of Figures

Figure 1 Example of contamination pattern.....	1
Figure 2 NanoRem project structure (NanoRem)	2
Figure 3 Example of hydraulic containment using P&T technology in a plan view and in a cross section (EPA, 1996)	8
Figure 4 Example of plume being treated by a permeable reactive barrier wall (Powell, et al., 1998)	9
Figure 5 Schematic drawing of direct push injection (Geoprobe Systems)	11
Figure 6 Molecular structure of PCE.....	13
Figure 7 Molecular structure of TCE	13
Figure 8 ZVI particle, with a shell of oxides and/or hydroxides. Adapted from (Jang, Lim, & Hwang, 2014)	15
Figure 9 Reaction scheme for reductive transformations of perchloroethylene (PCE). Solid arrows represent hydrogenolysis, finely dashed arrows show α - and β -elimination and coarse dashed arrows are for other steps, e.g. hydrogenation. Retrieved from (Kueper, Stroo, Vogel, & Ward, 2014), adapted from (Arnold & Roberts, 2000)	18
Figure 10 Contaminants which may be treated by nZVI (Zhang, 2003)	19
Figure 11 Schematic of the processes of particle aggregation and deposition (Elimelech, Gregory, & Jia, 2013)	20
Figure 12 Main mechanisms of particle transport and deposition (Messina, Marchisio, & Sethi, 2015)	21
Figure 13 Two ways by which the sites of an iron oxide surface may acquire a positive or a negative charge. The process (1b) shows better than (1a) that an overall zero charge can be obtained even when some sites have a local charge (Herbillon, 1988)	22
Figure 14 Electrical double layer and zeta potential (Malvern Instruments, 2015)	23
Figure 15 Terms of the total potential energy function (Malvern Instruments, 2015)	25
Figure 16 Energy profile presenting a primary and a secondary minimum (PM, SM) and an energy barrier (EB)	25
Figure 17 Example of relationship between zeta potential and pH for ZVI. Adapted from (Sun, Li, Cao, Zhang, & Wang, 2006)	26
Figure 18 Example of the influence of ionic strength on energy profiles	27
Figure 19 Representation of steric stabilization phenomenon (Elimelech, Gregory, & Jia, 2013)	28
Figure 20 A representation of clean-bed filtration theory (Tosco, Gastone, & Sethi, 2014)	29
Figure 21 Linear reversible attachment (Tosco, Gastone, & Sethi, 2014)	31
Figure 22 Blocking phenomenon (Tosco, Gastone, & Sethi, 2014)	31
Figure 23 Ripening phenomenon (Tosco, Gastone, & Sethi, 2014)	32
Figure 24 Straining phenomenon (C-vac)	32
Figure 25 Hyperbolic decrease of Darcy's flow velocity in a radial domain (Tosco, Gastone, & Sethi, 2014)	35

Figure 26 Viscosity versus shear rate for CMC solutions at different concentrations (Benchabane & Bekkour, 2008)	38
Figure 27 Structure of WALOCEL (The DOW Chemical Company)	39
Figure 28 SEM image of NANOFER STAR in powder form (NANO IRON s.r.o. - NANOFER STAR manual)	40
Figure 29 TEM image of activated NANOFER STAR (NANO IRON s.r.o. - NANOFER STAR manual)	41
Figure 30 Granulometric curve for Dorsilit 8. Adapted from (QUARZSANDE, 2012)	42
Figure 31 Grain size distribution of actual and reproduced VEGAS sands. Adapted from (Accolla, 2017).....	43
Figure 32 Reproduced (left) and actual (right) VEGAS sands.....	43
Figure 33 Preparation of a CMC solution	44
Figure 34 Picture of a NANOFER STAR suspension	45
Figure 35 HQ40d Portable multimeter: pH, conductivity and dissolved oxygen for water	45
Figure 36 Measuring with HQ40d Portable multimeter	45
Figure 37 Hydrogen evolution method: analysis	46
Figure 38 Hydrogen evolution method: end of test	46
Figure 39 Magnetic susceptibility meter during a sedimentation test	46
Figure 40 Freeze-dryer from Christ	47
Figure 41 BET instrument from Beckman Coulter, Inc. (Giotti, 2017)	47
Figure 42 Dried sample for BET measurement.....	47
Figure 43 Acoustic-electroacoustic spectrometer (left) and dispersing system (right)	48
Figure 44 Acoustic sensor. Pseudo-frontal (A) and top (B) views (Dukhin & Goetz, 2010).....	48
Figure 45 Disc centrifuge from CPS Instruments, Inc.	49
Figure 46 Frontal (left) and cross-sectional (right) views of the centrifuge disc (CPS Instruments Europe).....	49
Figure 47 Zetasizer Nano (left) and measuring cell (right) (Malvern Instruments).....	50
Figure 48 Disassembled stopper	50
Figure 49 Top (left) and bottom (center) views of the funnel. On the right picture, funnel and metal cylinder are displayed together.....	51
Figure 50 Argon flushing procedure	51
Figure 51 Peristaltic pump used for saturation	51
Figure 52 Pictures of a filled and saturated column (C2.3).....	52
Figure 53 Experimental setup for tracer tests. From right to left: degassed water tank, peristaltic pump, sand-packed column and flow cell with bromide sensor.....	53
Figure 54 Setup for hydraulic conductivity tests	54
Figure 55 Viscometer, top view (Physica - a Company by Antoon Paar)	55
Figure 56 Concentric cylinder configuration of the viscometer (Mezger, 2015)	55
Figure 57 Scheme of experimental setup for CMC column tests.....	55
Figure 58 Inflow pressure sensor	55
Figure 59 Scheme of experimental setup for NANOFER STAR column tests	57

Figure 60 Pictures of the magnetic susceptibility scanner: the signal registered within the copper coil can be correlated to a concentration of zerovalent iron present in the column	58
Figure 61 Tool for the calculation of energy profiles using DLVO or extended-DLVO interactions (MNM's©, 2018)	59
Figure 62 Tool for the calculation of single-collector contact efficiency (Yao's formulation) (MNM's©, 2018)	60
Figure 63 Representation of Cross model for shear-thinning fluids. Adapted from (ANSYS Fluent)	64
Figure 64 Shear stress vs. shear rate for different kinds of fluid (RheoSense - Simply Precise) .	87
Figure 65 Viscosity vs. shear rate for different kinds of fluids (RheoSense - Simply Precise)	88
Figure 66 Qualitative tracer test	95
Figure 67 Initial stages of NANOFE STAR test, column C1.2	100
Figure 68 Final stages of NANOFE STAR test, column C1.2	100
Figure 69 Transport test showing the presence of preferential flow paths	100
Figure 70 Final distribution of iron in column C2.2	104
Figure 71 Soil samples collected from column C2.2	104
Figure 72 Qualitative comparison between the suspensions prepared in water (the first three from the left) and those prepared in a certain concentration of CMC (the remaining five on the right)	107
Figure 73 Evaluation of the single-collector contact efficiency, for both columns C1.2 and C2.2 (MNM's©, 2018)	108
Figure 74 Tracer test evaluation, column C2.2 (MNM's©, 2018)	109
Figure 75 Output of the tracer test, column C2.2 (MNM's©, 2018)	109
Figure 76 Fitting of breakthrough curve, column C1.2 (MNM's©, 2018)	110
Figure 77 Fitting of concentration profiles, column C1.2 (MNM's©, 2018)	111
Figure 78 Estimated parameters via fitting, column C1.2 (MNM's©, 2018)	111
Figure 79 Fitting of breakthrough curve, column C2.2 (MNM's©, 2018)	112
Figure 80 Fitting of concentration profiles, column C2.2 (MNM's©, 2018)	112
Figure 81 Estimated parameters via fitting, column C2.2 (MNM's©, 2018)	113
Figure 82 Simulated pressure drop at 0.5, 1 and 3 meters from the center of the well during the injection of 6.5 g/L of NANOFE STAR and 10 g/L CMC in Dorsilit 8 sand with flow rate equals to 30 L/min (refer to Graph 47) (MNM's©, 2018)	118
Figure 83 Simulated pressure drop at 0.5, 1 and 3 meters from the center of the well during the injection of 6.5 g/L of NANOFE STAR and 10 g/L CMC in Dorsilit 8 sand with flow rate equals to 120 L/min (refer to Graph 49) (MNM's©, 2018)	118
Figure 84 Simulated pressure drop at 0.5, 1 and 3 meters from the center of the well during the injection of 6.5 g/L of NANOFE STAR and 40 g/L CMC in Dorsilit 8 sand with flow rate equals to 120 L/min (refer to Graph 57) (MNM's©, 2018)	124
Figure 85 Viscosity profile around the well, after 180 minutes of injection; NANOFE STAR concentration 6.5 g/L, CMC concentration 40 g/L, flow rate 120 L/min, Dorsilit 8 sand (MNM's©, 2018)	125

List of Tables

Table 1 Degradation rates and half-lives of PCE, TCE, DCE and VC (Hetterschijt, Stroet, & Bosma, 2000).....	14
Table 2 Properties of VEGAS degassed water. Adapted from (Giannelli, 2014)	37
Table 3 Basic characteristics of NANOFER STAR in powder form	40
Table 4 Grain distribution of Dorfner Dorsilit 8 (Frieser-München, 2011)	41
Table 5 Dorsilit sands reproducing VEGAS soil. Adapted from (Miyajima, 2015)	42
Table 6 Allowed combinations of different interaction sites in MNMs. Adapted from (Bianco, Tosco, & Sethi, 2018).....	62
Table 7 Having of NANOFER STAR concentrations due to settling	69
Table 8 Samples for BET analysis.....	69
Table 9 Samples measured with the acoustic-electroacoustic spectrometer	70
Table 10 Dimensions corresponding to the peaks of concentration	75
Table 11 Zeta potential of milled Dorsilit sand.....	82
Table 12 Calculation of hydraulic conductivity for column C1.2	84
Table 13 Properties of the columns	85
Table 14 Mass balance, column C1.2	98
Table 15 Hydraulic conductivity before and after the column test, column C1.2	99
Table 16 Mass balance, column C2.2	102
Table 17 Hydraulic conductivity before and after the column test, column C2.2	104
Table 18 Data for DLVO profile in degassed VEGAS water	105
Table 19 Data for DLVO profile in a 10 g/L CMC solution	106
Table 20 Effective porosity and dispersivity evaluated with MNMs.....	109
Table 21 Estimated parameters, used for the radial injection simulation.....	113
Table 22 Empirical coefficients C_a for both the kinds of sand	114
Table 23 Initial intrinsic permeabilities of the two kinds of sand	114
Table 24 Parameters of the Cross model for the 40 g/L CMC solution.....	120

List of Graphs

Graph 1 Content of zerovalent iron in different NANOFER STAR suspensions; values over time	67
Graph 2 Sedimentation tests for different NANOFER STAR suspensions in 10 g/L CMC	68
Graph 3 Comparison between the sedimentation of two suspensions at different temperatures	69
Graph 4 PSD of the reliable samples with 10 g/L of NANOFER STAR.....	71
Graph 5 PSD of the reliable samples with 15 g/L of NANOFER STAR.....	71
Graph 6 PSD of the reliable samples with 20 g/L of NANOFER STAR.....	72
Graph 7 PSD of the reliable samples with 30 g/L of NANOFER STAR.....	72
Graph 8 PSD of the reliable samples prepared in water.....	73
Graph 9 PSD of the reliable samples prepared in CMC 5 g/L.....	73
Graph 10 PSD of the reliable samples prepared in CMC 8 g/L.....	74
Graph 11 PSD of the reliable samples prepared in CMC 10 g/L.....	74
Graph 12 PSD obtained from the tests with the disc centrifuge: results by weight	76
Graph 13 PSD obtained from the tests with the disc centrifuge: results by weight, normalized on the maximum	76
Graph 14 PSD obtained from the tests with the disc centrifuge: results by number	77
Graph 15 PSD obtained from the tests with the disc centrifuge: results by number, normalized on the maximum	77
Graph 16 Comparison between spectrometer and disc centrifuge results; NANOFER STAR 10 g/L	78
Graph 17 Comparison between spectrometer and disc centrifuge results; NANOFER STAR 20 g/L	79
Graph 18 Mean value of peak size; comparison between spectrometer and disc centrifuge results.....	79
Graph 19 Representation of the zeta potential measurements. The grey, dashed line represents the value of potential given uniquely by the CMC dissolved in VEGAS water (background value); the blue, dotted line represents the values of the spectrometer measured close to the instrumental threshold and therefore not completely reliable	81
Graph 20 Calibration of bromide sensor prior to the tracer test of column C1.2.....	83
Graph 21 Breakthrough curve of the tracer test performed with column C1.2	83
Graph 22 Shear stress versus shear rate for water and different CMC concentrations	86
Graph 23 Rheogram of water and different CMC concentrations.....	87
Graph 24 Trend of hydraulic conductivities. K0 and K0' represent the hydraulic conductivities before the first and the second set of experiments respectively; all the other points represent the results of the hydraulic conductivity tests performed after each CMC injection (e.g. CMC5 v20 represents the conductivity measured after the injection of 5 g/L of CMC at 20 m/d seepage velocity, and so on)	89
Graph 25 Differential pressure caused by water and by different CMC concentrations injected in column; seepage velocity 10 m/d, column C1.1	90

Graph 26 Differential pressure caused by water and by different CMC concentrations injected in column; seepage velocity 20 m/d, column C1.1	90
Graph 27 Differential pressure caused by water and by different CMC concentrations injected in column; seepage velocity 50 m/d, column C1.1	90
Graph 28 Differential pressure caused by water and by different CMC concentrations injected in column; seepage velocity 100 m/d, column C1.1	91
Graph 29 Differential pressure caused by water and by different CMC concentrations injected in column; seepage velocity 300 m/d, column C1.1	91
Graph 30 Differential pressure caused by water and by different CMC concentrations injected in column; seepage velocity 10 m/d, column C2.1	92
Graph 31 Differential pressure caused by water and by different CMC concentrations injected in column; seepage velocity 20 m/d, column C2.1	92
Graph 32 Differential pressure caused by water and by different CMC concentrations injected in column; seepage velocity 50 m/d, column C2.1	92
Graph 33 Differential pressure caused by water and by different CMC concentrations injected in column; seepage velocity 100 m/d, column C2.1	93
Graph 34 Differential pressure caused by water and by different CMC concentrations injected in column; seepage velocity 300 m/d, column C2.1	93
Graph 35 Pressure corresponding to the plateau of each injection versus injection velocity, column C1.1	94
Graph 36 Pressure corresponding to the plateau of each injection versus injection velocity, column C2.1	94
Graph 37 Breakthrough curves of particles and of CMC, column C1.2.....	96
Graph 38 Iron distribution; comparison between scanner data and laboratory data, column C1.2	97
Graph 39 Cumulative mass; comparison between scanner data and mass balance, column C1.2	98
Graph 40 Parameters monitored during the NANOFER STAR test, column C1.2	99
Graph 41 Breakthrough curves of particles and of CMC, column C2.2.....	101
Graph 42 Iron distribution; comparison between scanner data and laboratory data, column C2.2	102
Graph 43 Cumulative mass; comparison between scanner data and mass balance, column C2.2	103
Graph 44 Parameters monitored during the NANOFER STAR test, column C2.2	103
Graph 45 Particle–collector and particle–particle DLVO profiles in VEGAS water	105
Graph 46 Particle–collector and particle–particle DLVO profiles in CMC 10 g/L	106
Graph 47 Profile of total particle concentration after 10, 30, 60, 120 and 180 minutes of injection; NANOFER STAR concentration 6.5 g/L, CMC concentration 10 g/L, flow rate 30 L/min, Dorsilit 8 sand	115
Graph 48 Profile of total particle concentration after 10, 30, 60, 120 and 180 minutes of injection; NANOFER STAR concentration 6.5 g/L, CMC concentration 10 g/L, flow rate 60 L/min, Dorsilit 8 sand	115

Graph 49 Profile of total particle concentration after 10, 30, 60, 120 and 180 minutes of injection; NANOFER STAR concentration 6.5 g/L, CMC concentration 10 g/L, flow rate 120 L/min, Dorsilit 8 sand	116
Graph 50 Profile of total particle concentration after 10, 30, 60, 120 and 180 minutes of injection; NANOFER STAR concentration 6.5 g/L, CMC concentration 10 g/L, flow rate 30 L/min, VEGAS sand	116
Graph 51 Profile of total particle concentration after 10, 30, 60, 120 and 180 minutes of injection; NANOFER STAR concentration 6.5 g/L, CMC concentration 10 g/L, flow rate 60 L/min, VEGAS sand	116
Graph 52 Profile of total particle concentration after 10, 30, 60, 120 and 180 minutes of injection; NANOFER STAR concentration 6.5 g/L, CMC concentration 10 g/L, flow rate 120 L/min, VEGAS sand	117
Graph 53 Comparison of the three final iron distributions obtained with the injection of 6.5 g/L of NANOFER STAR particles suspended in 10 g/L of CMC for 180 minutes, at different flow rates (30, 60, 120 L/min); Dorsilit 8 sand	117
Graph 54 Simulation of iron distributions in the two porous media. NANOFER STAR 6.5 g/L in CMC 10 g/L, flow rate 120 L/min, Dorsilit 8 and VEGAS sands	119
Graph 55 Distance reached by a hypothetical ZVI target concentration of 10 g/L after 180 minutes of injection; NANOFER STAR 6.5 g/L, CMC concentration 10 g/L, flow rate 120 L/min, Dorsilit 8 sand. Detail of Graph 49	119
Graph 56 Distance reached by a hypothetical ZVI target concentration of 10 g/L after 180 minutes of injection; NANOFER STAR 6.5 g/L, CMC concentration 10 g/L, flow rate 120 L/min, VEGAS sand. Detail of Graph 52	120
Graph 57 Profile of total particle concentration after 10, 30, 60, 120 and 180 minutes of injection; NANOFER STAR concentration 6.5 g/L, CMC concentration 40 g/L, flow rate 120 L/min, Dorsilit 8 sand	121
Graph 58 Distance reached by a hypothetical ZVI target concentration of 10 g/L after 180 minutes of injection; NANOFER STAR 6.5 g/L, CMC concentration 10 g/L, flow rate 120 L/min, Dorsilit 8 sand. Detail of Graph 57	121
Graph 59 Profile of total particle concentration after 10, 30, 60, 120 and 180 minutes of injection; NANOFER STAR concentration 6.5 g/L, CMC concentration 40 g/L, flow rate 120 L/min, VEGAS sand	122
Graph 60 Distance reached by a hypothetical ZVI target concentration of 10 g/L after 180 minutes of injection; NANOFER STAR 6.5 g/L, CMC concentration 40 g/L, flow rate 120 L/min, VEGAS sand. Detail of Graph 59	122
Graph 61 Comparison between the iron distributions in the two porous media with different CMC concentrations (10 g/L and 40 g/L) after 180 minutes of injection; NANOFER STAR 6.5 g/L, flow rate 120 L/min	123
Graph 62 Comparison between the iron distributions in the two porous media with different CMC concentrations (10 g/L and 40 g/L) after 180 minutes of injection; NANOFER STAR 6.5 g/L, flow rate 120 L/min. Detail of Graph 61	123

List of Abbreviations

BET	<i>Brunauer-Emmett-Teller theory</i>
CFT	<i>Clean-bed Filtration Theory</i>
CHC	<i>Chlorinated Hydrocarbon</i>
CMC	<i>Carboxymethyl Cellulose</i>
CVI	<i>Colloid Vibration Current</i>
DCE	<i>Dichloroethylene</i>
DCS	<i>Differential Centrifugal Sedimentation</i>
DLVO	<i>Derjaguin-Landau-Verwey-Overbeek theory</i>
DLS	<i>Dynamic Light Scattering</i>
DO	<i>Dissolved Oxygen</i>
DP	<i>Degree of Polymerization</i>
DNAPL	<i>Dense Non-Aqueous Phase Liquids</i>
DS	<i>Degree of Substitution</i>
EDL	<i>Electrical Double Layer</i>
IARC	<i>International Agency for Research on Cancer</i>
IEP	<i>Isoelectric Point</i>
IS	<i>Ionic Strength</i>
LDE	<i>Laser Doppler Electrophoresis</i>
MNMs	<i>Micro- and Nanoparticles transport, filtration and clogging Model - Suite</i>
mZVI	<i>microscale Zerovalent Iron</i>
NAPL	<i>Non-Aqueous Phase Liquids</i>
nZVI	<i>nanoscale Zerovalent Iron</i>
ORP	<i>Oxidation Reduction Potential</i>
PCE	<i>Perchloroethylene (tetrachloroethylene)</i>
P&T	<i>Pump and Treat</i>
PRB	<i>Permeable Reactive Barrier</i>
PSD	<i>Particle Size Distribution</i>
PV	<i>Pore Volume</i>
SEM	<i>Scanning Electron Microscope</i>
TCE	<i>Trichloroethylene</i>
TEM	<i>Transmission Electron Microscope</i>
TOC	<i>Total Organic Carbon</i>
VC	<i>Vinyl Chloride</i>
WP	<i>Work Package</i>
ZVI	<i>Zerovalent Iron</i>

1. Introduction

1.1. Motivation: soil and groundwater pollution

In the last decades, the widespread use of chemical products in human activities and the disposal of large quantities of waste materials, together with the accidental spill of harmful substances, have represented three of the main causes of soil and groundwater contamination across Europe. As hazardous substances, e.g. pesticides, heavy metals, oil products and solvents, are very common in everyday life and as they are often extremely persistent, it is possible to infer the reasons why they can pose a serious threat to public health. After being released in the environment, they can in fact gradually migrate from the source of contamination and reach the groundwater, polluting it. Then, thanks to the groundwater flow, they might move again and reach for instance a spring, a river or a drinking well, thus endangering the exposed receptors, as shown in Figure 1 ([National Research Council, 1984](#)).

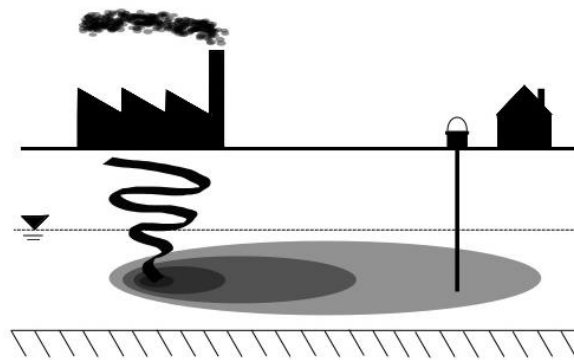


Figure 1 Example of contamination pattern

It is also worth mentioning that most of these pollutants may generally have both acute and chronic effects on human health. In the usual situation of a groundwater contamination however, the conditions are more likely to affect the exposed receptors with a chronic illness that might appear after several years of exposure. Therefore, a polluting source may not be identified for long time and the application of any technique of remediation could be considerably delayed. For this reason, when a contaminant source with potential negative impacts is ascertained, it must be treated in the most rapid and effective way possible.

Nowadays, since the awareness of people towards environmental and public health aspects is becoming more and more relevant and the legislation of the European countries is getting everyday stricter, it is fundamental to develop new and ameliorated strategies of remediation of polluted sites, that may be adopted effectively in various circumstances and conditions.

1.2. The NanoRem project

Nanoremediation is an emerging technology. By 2009, 44 full-scale applications had been documented around the world, mostly in the United States ([Mueller, et al., 2012](#)) ([PEN - The Project on Emerging Nanotechnologies](#)). In Europe, the main research project on this subject was the *NanoRem project* (2013 – 2017), funded through the European Commission FP7 and carried out by 28 partners, among which *DIATI* (Department of Environment, Land and Infrastructure Engineering - Politecnico di Torino) and *VEGAS* (Research Facility for Subsurface Remediation - University of Stuttgart). Its main goal was to facilitate a practical, safe, economic and exploitable nanotechnology that allowed to take the remediation processes from lab scale to end user applications ([NanoRem](#)). The overall strategy of the research project is shown in Figure 2; eleven Work Packages (WPs) with different focuses were arranged in functional groups.

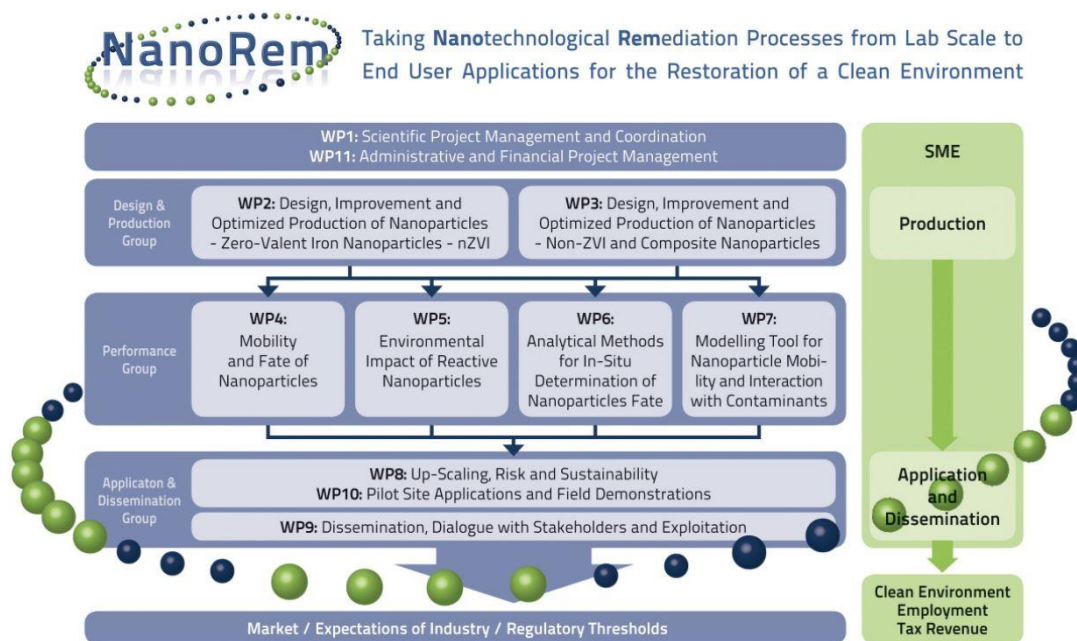


Figure 2 NanoRem project structure (NanoRem)

As a result of this intense research campaign, twelve final bulletins have been created to transfer to end-users the information developed within the project. These documents, together with the numerous publications and scientific papers, represent the main findings of the project and work as guidelines for future applications of the nanoremediation technique.

Nowadays, after the Final Conference of the 21st November 2016 and some last updates in the early 2017, *NanoRem* is officially concluded; however, many researchers who took part in the project are still working on this technology, which presents many application advantages, but still has aspects to be investigated and comprehended.

1.3. The present master's thesis and its objectives

The present master's thesis represents a follow-up of the NanoRem project, mainly of the WP4 and the WP7, concerning the mobility of nanoparticles and the modeling tools respectively. In effect, the goal of this research project is to combine the results of previous MSc theses conducted in VEGAS and Politecnico di Torino and determine additional parameters to characterize the properties for different nZVI suspensions, understand their influence on particle transport, and verify the applicability of the filtration theory by the conduction of single column tests; finally, the obtained data are used to evaluate nanoparticle transport through the software MNMs from Politecnico di Torino and to simulate a field injection in a radial geometry domain.

In particular, this work studied the commercial nZVI called NANO FER STAR, an iron powder produced by NANO IRON s.r.o. (see section 4.1.3). To successfully employ this product for the purposes of nanoremediation, it has to be dispersed in aqueous solutions which can be directly injected into the soil to create extended reactive zones where the contaminants are degraded. However, it is known that the dispersion of iron particles in water creates unstable colloidal systems, subject to a rapid sedimentation (Cwiertny, Handler, Schaefer, Grassian, & Scherer, 2008) (Tiraferri & Sethi, 2009) (Saleh, et al., 2008) (Dalla Vecchia, Luna, & Sethi, 2009). In these conditions, an injection in the soil would result in a poor radius of influence from the injection point, in a heterogeneous distribution of the iron and maybe in the clogging of the porous medium. Thus, it is required to improve the suspension properties to enhance their stability and their transport behavior.

Several studies have investigated the effects of the addition of polymers in the iron suspensions, achieving better stability and transport conditions (He, Zhang, Qian, & Zhao, 2009) (Lin, Tseng, Wey, & Lin, 2010) (Raychoudhury, Tufenkji, & Ghoshal, 2012). In this thesis the role of the carboxymethyl cellulose (CMC) in determining the properties of the iron suspensions and its contribution to the transport was evaluated.

The addition of CMC increases the viscosity of the carrier fluid; this condition may have positive impacts on the stability and mobility of the iron particles, but during field injections a high viscosity of the fluid means a great increase in the pressures in the porous medium, which can result in its fracturing.

In short, the present thesis tries to study more in detail how the suspension properties affect particle stability and transport, how the addition of carboxymethyl cellulose influences the iron suspensions, which is the transport behavior of NANO FER STAR particles in the porous medium and which would be the outcome of a field injection in terms of iron distribution and pressure buildup.

Working to achieve the abovementioned objectives, it is important to establish some research questions, that served as guidelines during the experimental work:

- **Which is the actual content of zerovalent iron in the NANOFE STAR particles? Does it change when preparing the suspensions starting from the product in powder form? Is it decreasing over time?**

At first, a test on the content of zerovalent iron in the NANOFE STAR suspensions was necessary. Not all the commercial product NANOFE STAR is indeed Fe^0 , useful in the nanoremediation process; in addition, the iron first appears as a powder and needs to be dispersed in a water-based carrier fluid and activated: this procedure may cause a reduction of the Fe^0 available. The amount of zerovalent iron was monitored for a certain time, to check if some ageing process was happening.

- **How do the particle and the suspension properties influence the stability of a colloidal system and therefore its transport in the porous medium?**

Particle size distribution and zeta potential seem to have an important role in determining the stability of colloidal particles and consequently their mobility in a porous medium. These determinations were performed always considering if the concentration of particles or of the stabilizing polymer had some influence on the results; in addition, sedimentation tests definitively proved the role of the iron concentration on colloidal stability.

At last, also the zeta potential of the porous medium was analyzed because it expresses the tendency of particles to the deposition.

- **How does the carboxymethyl cellulose vary the suspension properties and how is this reflected on the colloidal stability and on transport?**

Experiments on CMC solutions have been performed to understand the reasons why the polymer enhances the properties of the carrier fluid, which result in an improved transport during the injections. In particular, the viscosity variation due to high concentrations of polymer was investigated, as well as the rheological behavior of the solutions: some polymers exhibit a non-Newtonian behavior that may determine better transport conditions.

- **How do the porous medium properties influence the mobility and the distribution of the iron during an injection? Which deposition mechanisms take place?**

A selected combination of NANOFE STAR and CMC was used to conduct particle injection tests in two different porous media, to compare the results obtained in a homogeneous sand and in a heterogeneous one, which better replicates generic field conditions. The assessment of the results was performed using breakthrough curves, mass balances, magnetic susceptibility scanner data and laboratory analysis on the sand samples of the column. The injections have been modeled using the software MNMs to understand the deposition mechanisms occurring in the porous media and to estimate the parameters controlling these phenomena.

- **How can the modeling of the tests help the comprehension of the aggregation and deposition phenomena? What would be the outcome of a field application if a selected suspension was injected?**

MNMs allows the calculation of energy interaction profiles between two colloids or between a dispersed particle and a sand grain. Also, through MNMs it is possible to evaluate the collision probability of the colloids on a collector, which is the first step of the deposition phenomenon.

For these reasons, the energy profile and the collision efficiency have been evaluated via software.

However, the most important tool in the software is the transport simulator; the modeling of the column injections can provide information about the deposition mechanisms happening during the tests and give a quantification of the parameters which regulate them. The assessment of these processes consented the simulation of injections in radial geometry, which can predict the spatial iron distribution and the pressure buildup occurring during a field application.

The present work consists of 6 chapters; besides the Introduction, containing a short preface on the motivation, contextualization and explanation of the purposes of this work, Chapter 2 gives a quick overview of the main techniques for the remediation of the groundwater and Chapter 3 focuses on the theoretical background of the subject. Chapter 4 contains the description of the materials and of the experimental procedures followed during the analyses, as well as a global presentation of the software MNMs; the results of the tests are gathered and commented in Chapter 5, while the main findings are summarized in Chapter 6. Finally, some additional results are placed in Appendix A.

2. Overview of the main remediation techniques

A great variety of containment and remediation techniques for both the vadose zone and the groundwater has been developed during the last years; this is a field of intense research and new strategies are continuously discovered, while old methods are continuously improved and refined.

It is possible to classify these numerous methods according to various criteria, e.g. the polluted matrix (soil or groundwater) treated, the kind of treatment involved (physical, chemical or biological) and the site where the treatment is performed (*in situ* or *ex situ*). Based on the last criterion, it is worth remembering that the *ex situ* methods (which include *on-site* or *off-site* treatments) require the extraction of the contaminated matrix and its management, respectively in a dedicated mobile installation or in a different existing plant. Most European legislations encourage the choice of *in situ* remediation strategies, because usually the costs of removal of the polluted matrix are very elevated. Furthermore, the extraction process implies the management of the polluted medium and may expose the environment and the workers to some contaminants. However, sometimes *ex situ* methods allow to reach more effective results in terms of abatement of contaminant concentrations and on-site methods are a good alternative to *in situ* ones (Di Molfetta & Sethi, 2012).

In general, any treatment must consider two main issues: the control of the polluting source to prevent further releases, and the cleanup of the polluted soil and/or groundwater, with the objective of heavily reduce its concentrations of contaminants. As a matter of fact, in many cases, the disposal or the containment of the source, even though necessary, is often not sufficient to ensure the remediation of a polluted site and more measures have to be implemented to considerably decrease the residual contaminant concentrations in the soil and/or in the groundwater. Furthermore, pools of accumulated pollutant may behave as secondary sources of contamination, continuing to spread the contamination (Fetter, Boving, & Kreamer, 2017).

In the next sections the main remediation techniques are briefly presented, focusing on the ones allowing the remediation of the groundwater.

2.1. Source-control measures

As stated before, the control of the source of contamination is practically always a prerequisite to achieve an effective remediation of a polluted site: an on-going polluting source is in fact likely to make the remediation of the soil or water pointless. If a waste is placed in an unsecure landfill, for instance, it could be washed out by precipitations and therefore a remediation of the groundwater might be vain until the source is not correctly managed.

The control of the source can be obtained through physical removal of the waste and consequent transportation to a secure landfill or incinerator, through the construction of physical barriers surrounding the waste (*containment*) or through solutions that minimize the infiltration of precipitation (Fetter, Boving, & Kreamer, 2017).

2.2. Pump and treat

The classical remediation technique of the groundwater consists in extracting the water and treating it on the surface, which is referred to as *Pump and Treat (P&T)* technology. These systems can be designed both for the cleanup of contaminated groundwater, both for the containment of the source and of the pollutant plumes (Mercer, Skipp, & Giffin, 1990).

In a P&T treatment scheme used for the cleanup, contaminated groundwater and/or a mobile *NAPL phase*¹ are pumped to the surface to be more easily treated, usually by air stripping or by granular activated carbon absorption (Hamby, 1996). The realization of such a system requires the localization of the contamination in a three-dimensional space, the knowledge of the aquifer properties and the design and the installation of extraction (and in some cases injection) wells. Also, it is highly recommended to integrate the system with monitoring wells to check the effectiveness of the solution.

The P&T technology can also be applied as a hydraulic barrier to prevent off-site migration of pollutant plumes: the basic principle consists in modifying the hydraulic gradient, diverting the surrounding groundwater flow towards the extraction wells. An example of a P&T system used for the hydraulic containment is shown in Figure 3.

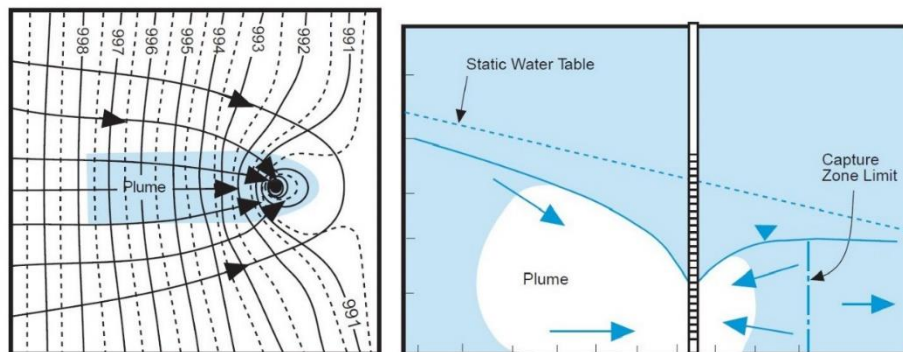


Figure 3 Example of hydraulic containment using P&T technology in a plan view and in a cross section (EPA, 1996)

Although the P&T technology is appropriate for many groundwater contamination problems (Ziegler, 1989), to be successfully applied it requires certain conditions. First, it is necessary that the subsurface has a sufficient hydraulic conductivity (K) to allow the water to flow. Secondly, the contaminants must be readily transportable by the fluid towards the extraction wells. In some cases, in fact, the heterogeneity of the aquifer or the state of the contaminant (sorbed or precipitated chemicals, or immobile NAPLs present as a separated phase slightly miscible) prevent the P&T technique to have a good performance.

The main limitation of this method however is definitely the long time required to obtain an acceptable level of cleanup, caused by the fact that many contaminants desorb and/or dissolve at a very slow rate, extending enormously the duration of the treatment. Consequently, operating costs are generally very high. According to an EPA study of 2001, the average annual cost of a P&T system for the treatment of *Dense NAPLs (DNAPLs)* is approximately \$570 000. The

¹ A *NAPL phase* is a liquid phase consisting of one or more Non-Aqueous Phase Liquids, immiscible with water.

period of operation may vary considerably, but the average P&T system of this study operated for 18 years, reaching an average cost of \$10 million (US EPA, 2004).

Moreover, when the contaminants occur as NAPLs (gasoline, diesel fuel, etc.) another issue must be considered: some of the oily phase can be hold back by capillary forces into the pore spaces and therefore it cannot be readily pumped out. This situation is often the reason why, once the P&T system is stopped, the contaminant concentrations tend to increase again, potentially exceeding the acceptable limits; this phenomenon is known as *rebound* (Di Molfetta & Sethi, 2012). For this and other reasons, it is common to integrate P&T wells with other interventions with the purpose of improving the effectiveness of the whole system.

2.3. Permeable Reactive Barriers

Permeable reactive barriers (PRBs) represent nowadays a valid *in-situ* alternative to the conventional technology of pump and treat. They consist in the emplacement of a reactive medium perpendicular to the trajectory of the contaminated groundwater, so that the plume flows through the barrier reacting with it. The objective is to transform contaminants into less harmful compounds or fixate them to the reactive material (see Figure 4) (Powell, et al., 1998).

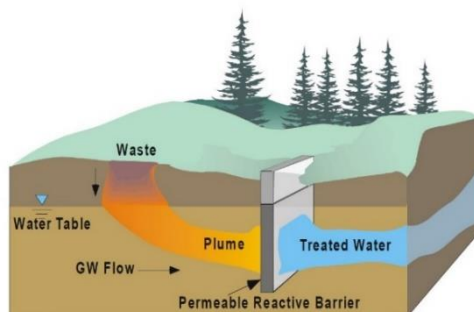


Figure 4 Example of plume being treated by a permeable reactive barrier wall (Powell, et al., 1998)

PRB technology has generated much interest in the last years because of its favorable cost/benefit ratio and its potential to confine the spread of contaminants (Powell, et al., 1998). An operating reactive barrier is in fact able to block the contaminants passively, with maintenance costs that only refer to the monitoring of performance. However, when designing a remediation through a PRB, it is fundamental to consider the excavation phase and the costs of purchase of the reactive materials, elements that contribute to raise considerably the expense of the whole operation, above all if the reagents in the barrier need to be substituted after a certain amount of time.

The most promising PRB application uses zerovalent iron (ZVI) as reactive material to degrade the contaminants into non-toxic compounds (Di Molfetta & Sethi, 2012). As described in section 3.2, this reagent has many advantageous properties in terms of remediation of various pollutants. Besides, an efficient functioning of a PRB also requires that its filling materials remain reactive for a long time, while ensuring an adequate hydraulic conductivity throughout the entire system. This condition is indeed necessary to make sure that the contaminated plume is intercepted by the barrier at all times, without being diverted elsewhere (Moraci & Calabrò, 2010) (Mumford, Rayner, Snape, & Stevens, 2014).

However, the main limitation of this technique is that only the contaminants flowing towards the barrier can be treated. The source of contamination as well as immobile compounds are not affected by the presence of the PRB, therefore their degradation is not at all enhanced. Moreover, if other aspects are considered, e.g. the advanced site characterization required, the inadequacy of realizing barriers deeper than 20 m from the surface, the possible need of replacing the reacting materials, etc., it is easy to realize that this technology requires specific conditions to be successfully applied (Obiri-Nyarko, Grajales-Mesa, & Malina, 2014).

2.4. Nanoremediation with nanoscale zerovalent iron

As described in section 2.3, the main application for ZVI has been its installation in permeable reactive barriers. Although successful in many cases, its use is limited for the treatment of plumes in shallow contaminated groundwater. Recently, the introduction of nZVI and mZVI (nanoscale and microscale ZVI respectively) allowed a larger range of applications, among which the direct injection of the reagent into the contaminant source, leading to the degradation of a wider range of contaminants with faster degradation rates (Grieger, et al., 2010). Microscale and especially nanoscale iron particles, because of their high specific surface area, are considerably more reactive than conventional ZVI. Moreover, due to their small size, can migrate in the subsurface, creating sufficiently large reactive zones for the degradation of the contamination (Mueller, et al., 2012). The main goal of this technique is in fact to deposit the iron in the pore space of the aquifer and hence form an injected reactive zone, able to remediate both the source and the plume.

There are different methods of application of this technology; the choice depends mainly on the geology and geochemistry of the polluted site in which the remediation must be performed (Crane & Scott, 2012). A well-known *in situ* application of nZVI is the injection in the aquifer through the Direct Push Technology (Geoprobe Systems) (see Figure 5). The main benefit of this system is that it allows to reach areas at contaminated sites not easily accessed by most of other remediation techniques; furthermore, its ability and simplicity to deliver the nZVI directly to the contaminant source areas and hot spots could easily prove the effectiveness of this technology in many applications (Grieger, et al., 2010) (Mueller, et al., 2012) (Velimirovic, et al., 2014) (Yang, Meng, & Guo, 2017).

Different ways of placing the nZVI into the soil require one or more injection wells. In some cases, a suspension of the reagent is injected in the subsoil thanks to the application of a high differential pressure (Quinn, et al., 2005) (CityChlor, 2013); in other cases, the injection is performed through permeation of the suspension into the ground. This last technique, unlike the previous ones, has the advantage of not raising excessively the pressures into the ground; excessive pressures in fact, may result in porous medium fracturing and consequent creation of preferential flow paths and heterogeneous distribution of the reagent. The permeation injection generates on the contrary a quite homogeneous flow through the soil pores and therefore, when particles are significantly smaller than pore size, it is recommended (Christiansen, et al., 2010) (Tosco, Papini, Viggi, & Sethi, 2014) (Gastone, Tosco, & Sethi, 2014a).

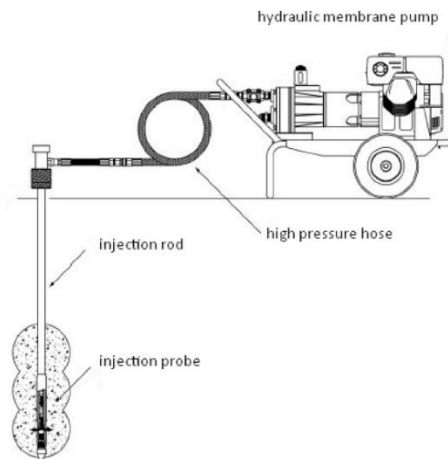


Figure 5 Schematic drawing of direct push injection (Geoprobe Systems)

Unfortunately, however, a key issue to successfully apply the strategies listed above is the assessment of the transport mechanisms of the injected nanoparticles, with the purpose of estimating their migration distance and their distribution into the porous medium; these pieces of information are fundamental for the design of any remediation (Grieger, et al., 2010).

Besides, the transport behavior of nZVI is also strictly related to the colloidal stability of the particles themselves, which have the tendency to aggregate and sediment out of the suspension. As a matter of fact, strong magnetic attractive interactions often lead to the formation of bigger dendritic aggregates that are more easily retained into pores of the medium, phenomenon also known as *straining* (Tosco & Sethi, 2010). In effect, the transport of unmodified nZVI suspensions has been proved scarce by many previous studies (Cwiertny, Handler, Schaefer, Grassian, & Scherer, 2008) (Tiraferri & Sethi, 2009) (Saleh, et al., 2008) (Dalla Vecchia, Luna, & Sethi, 2009) and therefore more research is necessary to develop materials and methods that would improve the stability of the nZVI suspensions. This last issue, together with the full understanding of the abovementioned transport mechanisms, are probably the two main challenges the nZVI technology must overcome in order to become a reliable alternative to the conventional remediation techniques.

3. Theoretical background

3.1. Chlorinated hydrocarbons

One of the most common categories of contaminants of the groundwater is represented by the halogenated aliphatic hydrocarbons, formed by substitution of 1, 2, 3 or 4 atoms of hydrogen with the same number of atoms of a halogen (chlorine, bromine, fluorine). In particular, because of their vast use in the industrial sector as solvents and their persistence in the soil, the chlorinated hydrocarbons (CHCs) are nowadays among the most relevant contaminants of the environment (Di Molfetta & Sethi, 2012). The tetrachloroethylene (or perchloroethylene, PCE) and the trichloroethylene (TCE) are the most frequently occurring types of CHCs, extensively used by industry as solvents for organic materials, as degreasers of metal parts and in dry cleaning (ATSDR - Agency for Toxic Substances and Disease Registry, 2018).

Tetrachloroethylene is a colorless, volatile liquid at room temperature, classified by International Agency for Research on Cancer (IARC) as a Group 2A carcinogen, that is to say *probably carcinogenic to humans* (IARC - International Agency for Research on Cancer, 2018). Moreover, it is known to have both acute and chronic effects on human health, that can affect the central nervous system, the eyes, the kidney, the liver, the lungs, the mucous membranes and the skin (ATSDR - Agency for Toxic Substances and Disease Registry, 2018). The molecular structure of PCE is shown in Figure 6.

Trichloroethylene, as well as tetrachloroethylene, is a colorless liquid at room temperature. TCE is classified by IARC as *carcinogenic to humans* (Group 1) (IARC - International Agency for Research on Cancer, 2018), with kidneys and liver as main target organs. Its toxicity may also affect the nervous and the reproductive system and generate kidney and liver damage (ATSDR - Agency for Toxic Substances and Disease Registry, 2018). Figure 7 shows the structure of TCE.

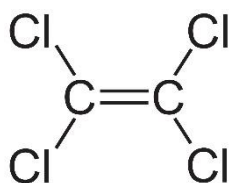


Figure 6 Molecular structure of PCE

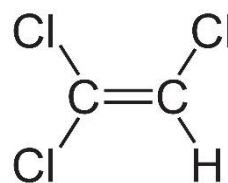


Figure 7 Molecular structure of TCE

Once these substances enter the environment, they can persist for many years because of their chemical stability and low solubility in water. In the Netherlands, Hetterschijt et al. developed a three-dimensional model based on *history matching*² to estimate the natural attenuation of these compounds and their by-products. Supposing a first-order degradation kinetic, they estimated the degradation rates for PCE, TCE, dichloroethylene (DCE) and vinyl chloride (VC), from which it is possible to calculate the half-lives shown in Table 1 (Hetterschijt, Stroet, & Bosma, 2000); the calculation between degradation rate and half-life was performed using Eq. 1.

² "History matching is the process of building one or more sets of numerical models which account for observed, measured data." (StreamSim Technologies, Inc.)

Table 1 Degradation rates and half-lives of PCE, TCE, DCE and VC (Hetterschijt, Stroet, & Bosma, 2000)

Substance	Degradation rate (3D model) [day ⁻¹]	Half-life [day]
PCE	0.0036	193
TCE	0.0080	87
DCE	0.0012	578
VC	0.0060	116

$$t_{1/2} = \frac{\ln 2}{D_R} \quad \text{Eq. 1}$$

Where:

- $t_{1/2}$ [T] is the half-life of the contaminant;
- D_R [T⁻¹] is the degradation rate of the contaminant.

The cited study demonstrates that these substances have extremely long half-lives; hence, often, if no reclamation operation is undertaken, 5 to 20 years are necessary for the concentrations of these compounds to comply to the regulatory limits.

Moreover, PCE and TCE are classified as DNAPLs: when spilled, if their volume is sufficient to cross the vadose zone and reach the water table, thanks to their greater density than water, they migrate vertically in the saturated zone until the volume is exhausted or until it is intercepted by an impermeable formation. At that point they start to migrate laterally following the slope of the substrate, that may differ from the direction of the water flow (Huling & Weaver, 1991). A precise localization of the contamination is therefore very complicated, while the recovery of the DNAPL phase is almost always inconceivable.

The difficult localization and the often-unfeasible extraction of PCE and TCE, combined with their natural persistence in the environment, show at the same time the complexity and the importance of intervening with any remediation technique. In the last decades, the *redox reactions*³ that these substances undergo when they are in presence of zerovalent iron have proved their effectiveness as a mean of remediation of CHCs.

³ "An oxidation-reduction reaction (or *redox reaction*) is a type of chemical reaction that involves a transfer of electrons between two species. A redox reaction is any chemical reaction in which the oxidation number of a molecule, atom, or ion, changes by gaining or losing an electron." (National Science Foundation, 2018)

3.2. Remediation with zerovalent iron

3.2.1. Iron particles and nanoparticles

Many metals like iron (Fe^0), zinc (Zn^0), magnesium (Mg^0) and aluminum (Al^0) have been tested at laboratory scale for the remediation of chlorinated hydrocarbons (Suresh, 2009); Fe^0 however, also known as zerovalent iron (ZVI), is the most promising and commonly used material for large-scale applications, both in PRBs (see Section 2.3) or for nanoremediation (see Section 2.4). A typical ZVI particle used in environmental application is shown in Figure 8, surrounded by a shell of iron oxides and/or hydroxides.

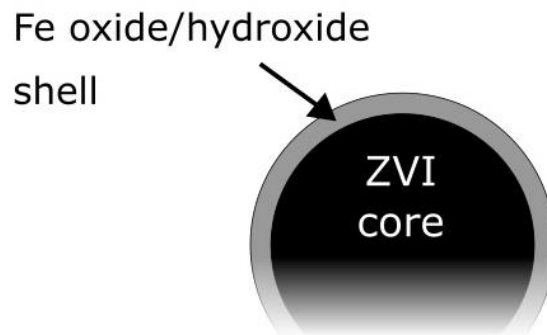


Figure 8 ZVI particle, with a shell of oxides and/or hydroxides. Adapted from (Jang, Lim, & Hwang, 2014)

Furthermore, as already mentioned in the Introduction, often the choice of nanoscale iron particles (nZVI, with size 10 – 100 nm ca.) is preferred for many reasons, such as:

- a) Nanoparticles can more easily access smaller pores and hard-to-reach sites of aquifers, shortening the clean-up times and potentially allowing for further injections (Grieger, et al., 2010);
- b) Because of their larger specific surface area, nanoscale particles are much more reactive; Mueller et al. demonstrated that nZVI reaction rates are 25 to 30 times faster than micro- to millimetric particles (Mueller & Nowack, 2010);
- c) Reactions induced by nZVI produce less toxic intermediate products than using larger iron particles (Grieger, et al., 2010);
- d) A short in-situ lifetime ensures that there is no risk of unwanted exposure for humans and for the environment (Mueller & Nowack, 2010).

However, the use of nZVI may also presents some disadvantages, including:

- a) The nZVI reacts with the target compounds as well as with non-target oxidants, which consume the reagent, following reactions commonly referred to as *corrosion* (see Section 3.2.2). In some aquifers, non-target reactions with oxygen [O_2], nitrate [NO_3^-] and sulfate [SO_4^{2-}] are expected to be the main cause of nZVI consumption (Suthersan, Horst, Schnobrich, Welty, & McDonough, 2016);
- b) Although nZVI primary particles have nanometric dimension, much larger aggregates may be formed because of magnetic and van der Waals attractive forces: the newly formed aggregates can be retained in small and dead-end pores, undergoing a phenomenon *straining* (see 3.3.5) (Phenrat, Saleh, Sirk, Tilton, & Lowry, 2007) (Tosco & Sethi, 2010).

- c) The nZVI performance in field applications is conditioned by different parameters, e.g. pH, redox potential (ORP), ionic strength (IS), dissolved oxygen in the groundwater (DO), etc. In field applications, where it is not possible to control thoroughly the conditions of the aquifer, it is complex to predict the outcome of a nZVI injection (Yu, Chen, Cheng, Lin, & Huang, 2014);
- d) The potential threats coming from the application of unmodified and modified nZVI to various environmental matrices are not entirely understood and recognized (Chen, Ji, Wang, & Zang, 2017);

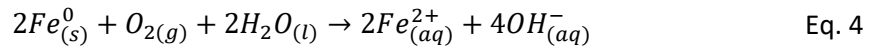
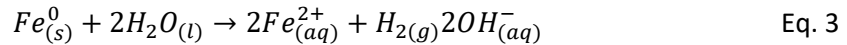
3.2.2. Corrosion of nZVI

Corrosion of metals is a natural phenomenon, which transforms a refined metal into a more chemically-stable form, such as an oxide, hydroxide or sulfide. This process of transformation is mainly caused by an irreversible redox reaction, in which an agent induces an *electrochemical*⁴ oxidation of a metal (Ghali, 2010); a typical example of corrosion is the formation of iron oxides on an iron surface, generally known as rust.

The process of corrosion is summarized by Eq. 2, where a generic metal (M) behaves as a reducing agent, giving up electrons that can be accepted by other chemical species present in the environment. In the reaction the metal is oxidized into a more stable form.



In aqueous media, Fe^0 rapidly oxidizes to Fe^{2+} and then possibly to Fe^{3+} following numerous competing reactions, which can occur in aerobic and in anaerobic conditions; Furakawa et al. (Furakawa, Kim, Watkins, & Wilkin, 2002) provided two examples (Eq. 3 and Eq. 4):

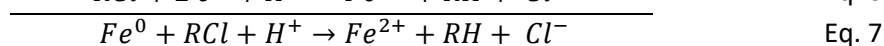
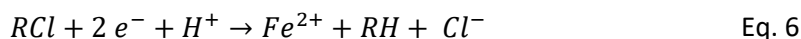
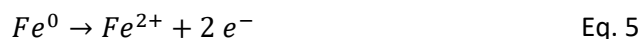


The previous examples show, also according to Schlimm and Heitz (Schlimm & Heitz, 1996), that two of the main electron acceptors in the subsoil are water and dissolved oxygen. In presence of certain contaminants however, these substances may accept part of the free electrons and therefore be reduced. The reduction of some contaminants is known to be an effective way to degrade them into non-harmful compounds. In particular, the remediation of chlorinated hydrocarbons through reduction by ZVI iron is emerging as a new alternative for the treatment of contaminated soil and groundwater (Mueller & Nowack, 2010).

⁴ “An electrochemical reaction is a chemical transformation that implies charge transport at the interface from a metallic conductor (electrode) to an ionic conductor (electrolyte).” (Ghali, 2010)

3.2.3. Degradation of chlorinated hydrocarbons

When the electrons freed during the oxidation of the zerovalent iron are accepted by a chlorinated solvent, this halogenated compound is slowly reduced to a simple hydrocarbon, losing chloride ions. This process can be summarized by the following equations:



In theory, the process of dichlorination should follow a sequence of chain reactions, where at each step an atom of chlorine is replaced by an atom of hydrogen (hydrogenolysis). Actually, nowadays, two main reaction mechanisms are known to cause the dehalogenation of the CHCs: *sequential hydrogenolysis* and *reductive elimination* (Di Molfetta & Sethi, 2012).

Figure 9 shows the possible paths of degradation of tetrachloroethylene. On the right it is possible to observe the sequence of degradation due to hydrogenolysis: PCE is reduced to TCE, DCE, VC and finally ethylene, losing one chlorine ion at every step and acquiring hydrogen instead. Before reaching the final, non-toxic compound, however, the starting substance is transformed in products which are often more harmful than the previous ones (such as VC, Vinyl Chloride). Moreover, it is known that the degradation rates become slower and slower at every step; hence there are some concerns about the risks of using this solution for the remediation of chlorinated compounds (Kueper, Stroo, Vogel, & Ward, 2014).

Fortunately, it has been demonstrated that in presence of nZVI the degradation path through reductive elimination predominates (Orth & Gillham, 1995); on the left side of Figure 9 the products of this mechanism are displayed. Dichloroacetylene, chloroacetylene or acetylene are formed when two chlorine ions are replaced by hydrogens in PCE, TCE or DCE respectively. When this process involves adjacent carbons, it is called *β-elimination*, while if the two Cl⁻ ions are eliminated from the same carbon, it is referred to as *α-elimination* (less common). Following this pathway, the production of toxic byproducts is minimized (Kueper, Stroo, Vogel, & Ward, 2014).

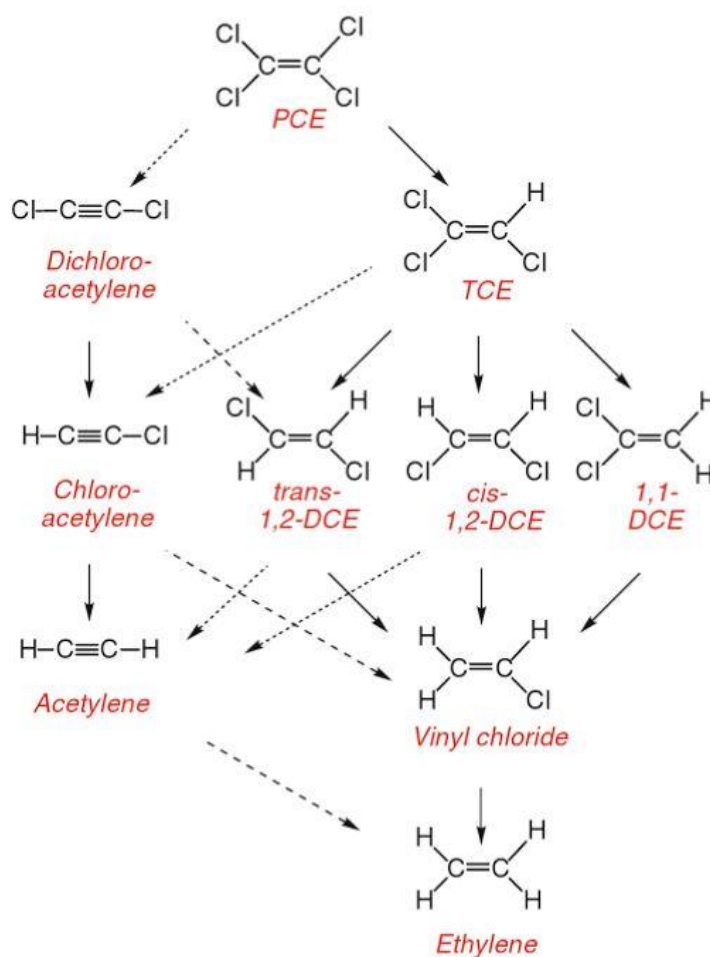


Figure 9 Reaction scheme for reductive transformations of perchloroethylene (PCE). Solid arrows represent hydrogenolysis, finely dashed arrows show α - and β -elimination and coarse dashed arrows are for other steps, e.g. hydrogenation. Retrieved from (Kueper, Stroo, Vogel, & Ward, 2014), adapted from (Arnold & Roberts, 2000)

Moreover, apart from chlorinated solvents, the nZVI particles are effective to remediate a wide range of other contaminants. As shown in Figure 10, Zhang (2003) provided a list of pollutants which may be treated with zerovalent iron, showing all the potentiality of this technology.

Chlorinated methanes	Trihalomethanes
Carbon tetrachloride (CCl_4)	Bromoform (CHBr_3)
Chloroform (CHCl_3)	Dibromochloromethane (CHBr_2Cl)
Dichloromethane (CH_2Cl_2)	Dichlorobromomethane (CHBrCl_2)
Chloromethane (CH_3Cl)	Chlorinated ethenes
Chlorinated benzenes	Tetrachloroethene (C_2Cl_4)
Hexachlorobenzene (C_6Cl_6)	Trichloroethene (C_2HCl_3)
Pentachlorobenzene (C_6HCl_5)	<i>cis</i> -Dichloroethene ($\text{C}_2\text{H}_2\text{Cl}_2$)
Tetrachlorobenzenes ($\text{C}_6\text{H}_2\text{Cl}_4$)	<i>trans</i> -Dichloroethene ($\text{C}_2\text{H}_2\text{Cl}_2$)
Trichlorobenzenes ($\text{C}_6\text{H}_3\text{Cl}_3$)	1,1-Dichloroethene ($\text{C}_2\text{H}_2\text{Cl}_2$)
Dichlorobenzenes ($\text{C}_6\text{H}_4\text{Cl}_2$)	Vinyl chloride ($\text{C}_2\text{H}_3\text{Cl}$)
Chlorobenzene ($\text{C}_6\text{H}_5\text{Cl}$)	Other polychlorinated hydrocarbons
Pesticides	PCBs
DDT ($\text{C}_{14}\text{H}_9\text{Cl}_5$)	Dioxins
Lindane ($\text{C}_6\text{H}_6\text{Cl}_6$)	Pentachlorophenol ($\text{C}_6\text{HCl}_5\text{O}$)
Organic dyes	Other organic contaminants
Orange II ($\text{C}_{16}\text{H}_{11}\text{N}_2\text{NaO}_4\text{S}$)	N-nitrosodimethylamine (NDMA) ($\text{C}_4\text{H}_{10}\text{N}_2\text{O}$)
Chrysoidine ($\text{C}_{12}\text{H}_{13}\text{ClN}_4$)	TNT ($\text{C}_7\text{H}_5\text{N}_3\text{O}_6$)
Tropaeolin O ($\text{C}_{12}\text{H}_9\text{N}_2\text{NaO}_5\text{S}$)	Inorganic anions
Acid Orange	Dichromate ($\text{Cr}_2\text{O}_7^{2-}$)
Acid Red	Arsenic (AsO_4^{3-})
Heavy metal ions	Perchlorate (ClO_4^-)
Mercury (Hg^{2+})	Nitrate (NO_3^-)
Nickel (Ni^{2+})	
Silver (Ag^+)	
Cadmium (Cd^{2+})	

Figure 10 Contaminants which may be treated by nZVI (Zhang, 2003)

Despite the vast prospects of application of nZVI particles, to achieve an effective remediation through this technique, a suitable dispersion of iron in the soil is required. For this reason, it is fundamental to investigate and understand the transport properties of these nanoparticles and to improve the methods by which they are delivered to the target zone.

3.3. Transport of nZVI

3.3.1. Aggregation and deposition of nZVI particles

The transport of nZVI is closely related to two aspects of the behavior of suspended nanoparticles: *aggregation* and *deposition*. Aggregation is the phenomenon by which particles associate to form clusters; deposition refers to the movement of the particles towards a surface, to which they remain attached (ref. Figure 11) (Elimelech, Gregory, & Jia, 2013).

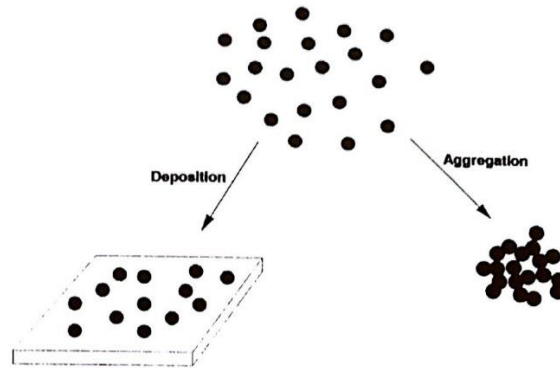


Figure 11 Schematic of the processes of particle aggregation and deposition (Elimelech, Gregory, & Jia, 2013)

The tendency of the nanoparticles to remain in a dispersed state is defined *colloidal stability*; a system may be called *stable* if the particles do not tend to form agglomerates, *unstable* otherwise. The stability of a colloidal system depends basically on two factors that may be treated, in most cases, independently:

- a) The occurrence of collisions between particles, due to their motion;
- b) The kind of interaction between colliding particles: attractive forces are likely to cause aggregation and lead the system towards instability, while repulsive forces prevent the formation of clusters making the system more stable.

Similarly, the process of deposition also involves transport and attachment steps and can be regarded as a particular aggregation which involves particles of different types. It is important to notice that colloidally stable particles could readily attach to a surface of a different kind, with which they have no repulsion (Elimelech, Gregory, & Jia, 2013).

Because of the relevance of the factors a) and b) on particle aggregation and deposition, and consequently on their mobility, the next sections will analyze these two aspects more in detail.

3.3.2. Collision mechanisms

The transport of a particle from the bulk of a suspension to the proximity of a *collector*⁵ is the first step that might lead to its deposition (or to its aggregation with another suspended particle). Three major mechanisms are known to be responsible for the occurrence of this transport stage (Yao, Habibian, & O'Melia, 1971).

⁵ "A *collector* refers to one of the grains on which the transported particles are gathered or deposited (Messina, Marchisio, & Sethi, 2015)

Figure 12 shows the main transport and deposition mechanisms. On the left side of the picture, the basic phenomena described by Yao et al. (1971) for a dimensionless particle are displayed: *Brownian diffusion* (D) in blue, *gravity* (G) in magenta and *advection and interception* (A) in black. On the right side of the figure, the same mechanisms also account for the *steric effects*⁶ of the particle and the collector (Messina, Marchisio, & Sethi, 2015).

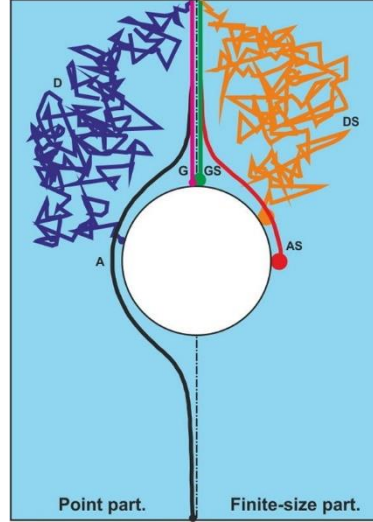


Figure 12 Main mechanisms of particle transport and deposition (Messina, Marchisio, & Sethi, 2015)

In the previous image the three phenomena are treated independently, neglecting any mutual interactions between the different transport mechanisms. In effect, the first quantification of the *single-collector contact efficiency* η_0 proposed by Yao et al. was simply the summation of three contributions: η_D due to Brownian motion, η_G related to gravity and η_I accounting for interception, as indicated in Eq. 8.

$$\eta_0 = \eta_D + \eta_G + \eta_I \quad \text{Eq. 8}$$

It is relevant to remind that, even if in many cases the previous equation is sufficient, the additivity of the three mechanisms is clearly a simplification hypothesis. When the different phenomena operate together, the supposed linearity of the interactions may lead to significant errors (Messina, Marchisio, & Sethi, 2015).

The single-collector contact efficiency η_0 quantifies how many particles reach the collector compared to all the particles incoming from the projection of the collector. To have a complete description of the deposition mechanism, it is now fundamental to quantify also the number of particles which become attached to the collector, once they reach it; to do so, the *attachment efficiency* α will be introduced in the following.

⁶ "A *steric effect* is an influence on a reaction or process determined by the fact that all of the atoms within a molecule occupy space, thus certain collision paths are either disfavored or favored." (Barnes)

3.3.3. Interaction mechanisms

Especially in aqueous systems, the interactions between colloidal particles are extremely important for the determination of particle stability because they define the fate of two particles (or a particle and a collector) that come into contact. The following subsections describe the main interaction mechanisms in a colloidal system.

3.3.3.1. Electrical interactions

Figure 8 showed the typical ZVI particle surrounded by a shell of oxides or hydroxides. In water, this shell may acquire a positive or a negative surface charge through a process that can be regarded either as a phenomenon of *adsorption*⁷ of H^+ or OH^- ions, or as a dissociation of sites at the interface (Herbillon, 1988). This mechanism is summarized in Figure 13, in which the attention is focused on a tiny portion of the shell.

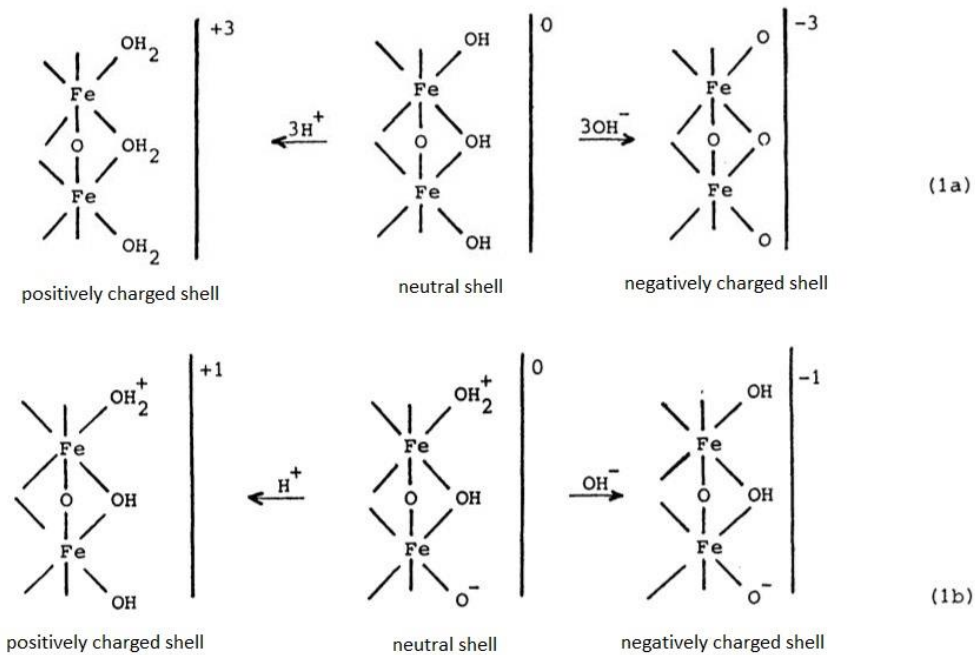


Figure 13 Two ways by which the sites of an iron oxide surface may acquire a positive or a negative charge. The process (1b) shows better than (1a) that an overall zero charge can be obtained even when some sites have a local charge (Herbillon, 1988)

As the previous illustration suggests, it is important to notice that this process is strongly influenced by the availability of H^+ and OH^- ions dissolved in water, hence the pH has a strong influence in determining the surface charge that the shell could acquire. In section 3.3.3.3 the contribution of pH on the stability of a colloidal suspension will be described more in detail.

⁷ "Adsorption is defined as the adhesion of a chemical species onto the surface of particles. [...] It is a different process from absorption, in which a substance diffuses into a liquid or solid to form a solution." (Helmenstine, 2017)

In any case, because of the presence of its surface charge, the shell must be balanced by an equivalent and opposite charge in solution. This balancing charge is constituted by an excess of oppositely charged ions close to the shell surface and by a deficit of similarly charged ions.

The earliest models that describe the distribution of ions surrounding a charged surface date back to 1853, when Helmholtz first suggested the idea of the *electrical double layer* (EDL) (Helmholtz, 1853). In the following century, many other scientists e.g. Gouy-Chapman, Stern and Grahame developed and improved Helmholtz's theory, achieving the description of a model that still today is considered as a reference point in many fields.

Figure 14 shows the conventional EDL: a negatively charged surface is readily surrounded by a thin layer of positive ions, firmly attached to the colloid (*Stern layer*); moving away from the charged surface, the positive ions still sense its attraction, but their concentration decreases more and more, while negative ions begin to be present (*Gouy or diffuse layer*). The Stern and the Gouy layers represent the aforementioned double layer, that ends when the ions do not perceive the influence of the charged surface anymore: the *bulk* of the dispersing medium has been reached (Prakash & Yeom, 2014).

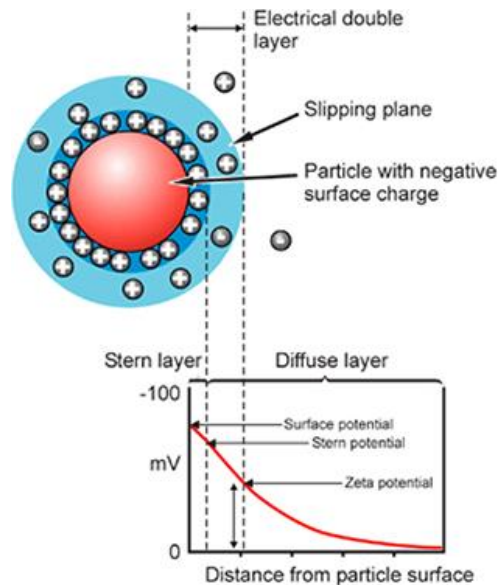


Figure 14 Electrical double layer and zeta potential (Malvern Instruments, 2015)

As presented in Figure 14, the surface charge and the double layer determine the formation of an electrical potential around the colloid. When two suspended particles come into contact, they sense the reciprocal interference and, having usually a charge of the same sign, they repel each other. A similar situation occurs between particle and collector.

To quantify the repulsive forces, it is possible to measure the electrical potential surrounding the colloid. From the standpoint of colloid stability however, instead of measuring the potential at the particle surface, it is more relevant to measure it at the slip plane that divides the immobile from the mobile portion of the double layer (Elimelech, Gregory, & Jia, 2013). The potential corresponding to this plane is referred to as ζ -potential or *zeta potential*, and it is more representative of the interactions sensed by colloids in suspension.

3.3.3.2. Van der Waals interactions

The presence of some attractive forces between colloidal particles of the same kind has long been recognized, but its comprehension took a long time to develop (Israelachvili, 2011). These forces, named after the scientist Johannes Diderik van der Waals, are based on the fact that spontaneous, transient electrical and magnetic polarizations can arise within a colloid, due to a motion of electrons in its molecules, or to a molecular distortion and/or orientation. This electromagnetic polarization can in this way perturb the surrounding region and induce further fluctuations elsewhere, resulting in an attractive *dispersion force*⁸ that Fritz London first calculated in his famous 1930 paper (London, 1930) (Ninham & Parsegian, 1970).

The classical (or *microscopic*) approach to the evaluation of van der Waals interactions is largely due to Hamaker (1937): the attractive forces between two macroscopic bodies can be estimated through the pairwise summation of all the singular intermolecular interactions. This assumption of additivity represents a simplification, but allows to divide the expressions into a purely geometrical part and a constant, A . This constant, known as *Hamaker constant*, is dependent only on the characteristics of the interacting bodies and on the medium; the constant A has generally a value between 10^{-21} and 10^{-19} Joule (Elimelech, Gregory, & Jia, 2013).

3.3.3.3. DLVO theory

The DLVO theory (named after the scientists Derjaguin, Landau, Verwey and Overbeek who developed it in the 1940s,) assumes van der Waals attraction and EDL repulsion as two additive phenomena that, combined, determine the total potential energy of interaction between particles as a function of separation distance. All other forms of interaction are neglected. The total energy function V_T can then be written as follows (Elimelech, Gregory, & Jia, 2013):

$$V_T = V_R + V_A \quad \text{Eq. 9}$$

Where:

- $V_R [M L^2 T^{-2}]$ is the sum of repulsive forces (due to the electrical double layer);
- $V_A [M L^2 T^{-2}]$ is the sum of attractive forces (due to van der Waals interactions).

It is possible to express V_R and V_A in their simplest form as shown in Eq. 10 and Eq. 11.

$$V_R = 2\pi\epsilon a\zeta^2 e^{-kD} \quad \text{Eq. 10}$$

Where:

- ϵ is the solvent permeability;
- a is the colloid radius;
- ζ is the zeta potential;
- k is a function of the ionic composition;
- D is the colloidal separation distance.

NB: The previous expression is rigorously valid for sphere–sphere interactions.

⁸ The London *dispersion force* is a temporary attractive force that results when the electrons in two adjacent atoms occupy positions that make the atoms form temporary dipoles. This force is sometimes called an induced dipole-induced dipole attraction." (Purdue University)

$$V_A = -\frac{A}{12\pi D^2} \quad \text{Eq. 11}$$

Where:

- A is the Hamaker constant;
- D is the colloidal separation distance.

NB: The previous expression is rigorously valid for plate–plate interactions.

The total potential energy function can be represented schematically as shown in Figure 15, where a negative sign of the energy means attraction between colloids, and a positive sign means repulsion.

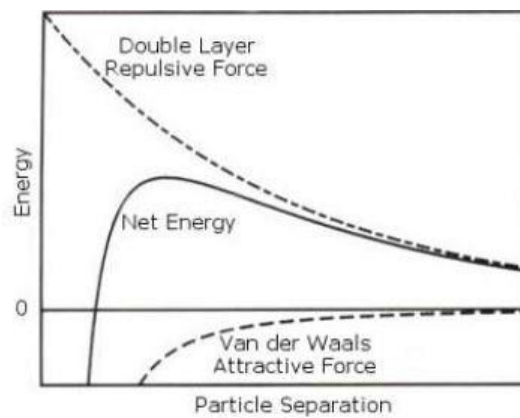


Figure 15 Terms of the total potential energy function (Malvern Instruments, 2015)

It is relevant to notice that the net energy of interaction displayed in the previous image may assume different configurations depending on the functions V_R and V_A ; the shape of this curve reflects the behavior of colloidal particles in Brownian motion (ref. Figure 16). In particular:

- a) The presence of a primary maximum creates like an energy barrier (EB) that prevents the particle from aggregating; it is the typical situation of a stable colloidal system.
- b) The presence of one or two minima promotes the aggregation of the particles. The secondary minimum (SM) allows reversible attachment, while the primary minimum (PM) often determines irreversible attachment.

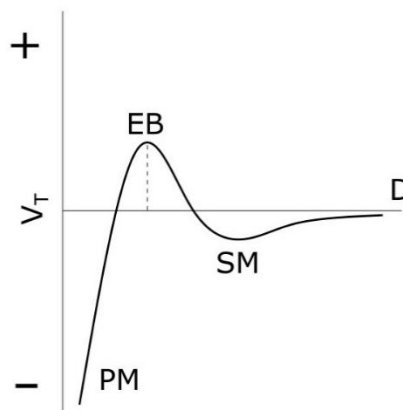


Figure 16 Energy profile presenting a primary and a secondary minimum (PM, SM) and an energy barrier (EB)

In an aqueous colloidal system there are two main parameters of the medium that influence the net energy curve of dispersed particles: pH and ionic strength.

In Section 3.3.3.1 the importance of pH on electrostatic forces has already been mentioned: it influences the surface charge that a colloid tends to acquire and, consequently, its EDL energy profile. Referring to Eq. 9 and Eq. 10, it is now possible to affirm that the change in the energy profile is reflected by a variation in the zeta potential, and finally in the repulsive forces V_R . A typical relationship between zeta potential and pH for a ZVI particle is represented in Figure 17.

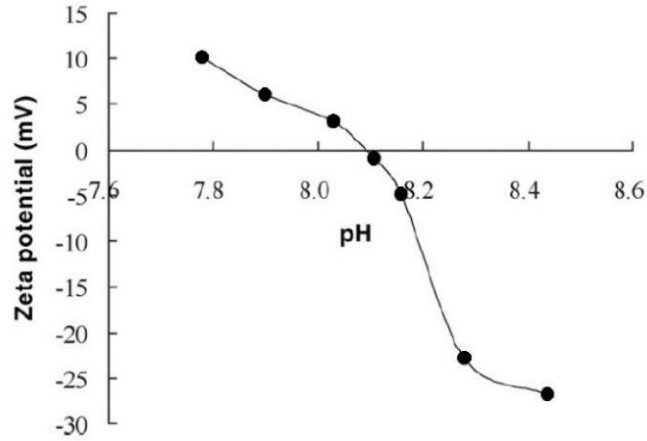


Figure 17 Example of relationship between zeta potential and pH for ZVI. Adapted from (Sun, Li, Cao, Zhang, & Wang, 2006)

Referring to the previous image, it is worth noticing that there are values of pH for which zeta potential approaches zero (*isoelectric point*, IEP). In this situation the repulsive forces between colloidal particles are very weak and they are likely to aggregate. Zhang (2003) defines stable the dispersed particles with zeta potential values above +30 mV or below -30 mV; on the contrary, when their zeta potential is equal to 0 mV, they are in conditions of maximum instability.

Another important element influencing the energy profiles is ionic strength IS, which represents a measure of the concentration of ions in a solution (Solomon, 2001). Indeed, the presence of many ions in solution may alter the EDL profile of a colloidal particle because they can work as a screen around the charged colloid. The result is usually a decrease in the repulsive field surrounding the particles, which leads to an enhanced aggregation or deposition.

Ionic strength can be expressed in different forms, but the most common is the molar ionic strength (M or $mol \cdot L^{-1}$), calculated as reported in Eq. 12 (McNaught & Wilkinson, 1997).

$$IS = \frac{1}{2} \sum_{i=1}^n c_i z_i^2 \quad \text{Eq. 12}$$

Where:

- $c_i [M]$ is the molar concentration of the i-th ion;
- $z_i [-]$ is valence of the i-th ion.

To have a better idea about how a change in ionic strength acts on the net energy curves, an example is provided in Figure 18. It is relevant to notice that an increase of IS reduces the repulsive energy barrier facilitating aggregation or deposition of colloids.

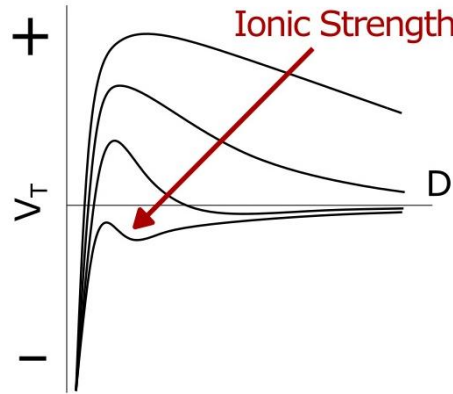


Figure 18 Example of the influence of ionic strength on energy profiles

Energy profiles are fundamental to understand the tendency of two colloidal particles to aggregate when they approach each other in their Brownian motion. Moreover, in the presence of a repulsive barrier, its height reveals that only the fraction of colloids having a higher energy could form aggregates, while the fraction with lower energy cannot. This phenomenon can be quantified introducing the *attachment efficiency* α , usually determined by experimental tests.

Having introduced both a *single-collector contact efficiency* (η_0 , see 3.3.2) and an *attachment efficiency* (α), a first complete description of aggregation and deposition phenomena, accounting for both the steps of transport and attachment, is now possible. In particular, it is usual to define the *single-collector removal efficiency* η as follows:

$$\eta = \alpha \eta_0 \quad \text{Eq. 13}$$

The quantity η will be central in the description of the transport behavior of particles and especially in the theory of the *clean-bed filtration* (CFT) (ref. 3.3.4).

Before proceeding with CFT however, it is important to present other interactions between dispersed particles which are not included in the DLVO theory; sometimes, in fact, they have relevant implications on the stability of colloidal systems.

3.3.3.4. Non-DLVO forces

In a colloidal system there are many other forces not accounted for in the classic DLVO model; in some cases, they have a significant influence on aggregation and deposition mechanisms and a description solely based on electric and van der Waals interactions may not be enough.

The main non-DLVO forces are:

- a) Born repulsions;
- b) Magnetic interactions;
- c) Steric stabilization.

Born repulsions

Born repulsions come from the short-ranged interactions that originate when the electron shells of two atoms begin to interpenetrate each other. A precise formulation of the interatomic potential must rely on quantum mechanical considerations, but some approximate analytical expressions have been proposed (Fitts, 1966).

However, the effect of Born interaction is usually not significant in aqueous systems, since the presence of hydrated ions prevents separation distances of colloids below 0.3 nm (Elimelech, Gregory, & Jia, 2013).

Magnetic interactions

Because of the magnetic properties of FeO and Fe₃O₄, magnetic attractive forces between particles may arise, affecting the colloidal stability of a dispersion (De Vicente, Delgado, Plaza, Durán, & González-Caballero, 2000). In particular, nZVI particles may undergo dipole–dipole interactions between magnetic moments, encouraging the formation of bigger aggregates (Phenrat, Saleh, Sirk, Tilton, & Lowry, 2007).

Steric stabilization

The presence of adsorbed polymers on the particle surface can play an important role in colloidal systems. In case of small amounts, adsorbed polymers can create chemical bonds between distinct polymeric chains, promoting the aggregation of different particles through a process called *bridging*. On the contrary, larger quantities of adsorbed polymers usually give an enhanced stability to colloids, through a mechanism known as *steric stabilization*. For this phenomenon to occur, the polymers must have a certain affinity with the particles surface, but at the same time a segment of the chain must extend from the colloids into the dispersion fluid. In this way, as two particles approach sufficiently close to each other, adsorbed polymeric layers come into contact, hindering a further interpenetration (ref. Figure 19) (Elimelech, Gregory, & Jia, 2013).

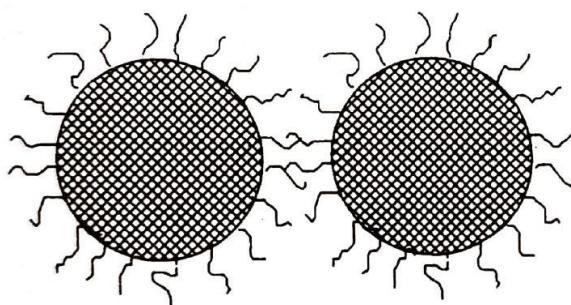


Figure 19 Representation of steric stabilization phenomenon (Elimelech, Gregory, & Jia, 2013)

Because of the presence of these three kinds of interaction, the DLVO model could be not sufficient to predict the aggregation tendencies of colloids. For this reason, sometimes it is better to resort to the *Extended DLVO*, which includes the classic DLVO forces plus the three listed above. This choice requires however the knowledge of specific experimental parameters, not always easy to determine.

3.3.4. Clean-bed filtration theory

Deposition of particles on the grains of a porous medium is generally described with the clean-bed filtration theory (CFT), developed by Yao et al. in 1971 (Yao, Habibian, & O'Melia, 1971). The filtration model, derived from a mass balance around a single collector, predicts particle removal in porous media as follows (Logan, 2012):

$$\frac{\partial c}{\partial x} = -\frac{3(1-\varepsilon)}{2d_{50}}\alpha\eta_0 c \Rightarrow c(x) = c_0 \exp\left(-\frac{3(1-\varepsilon)}{2d_{50}}\alpha\eta_0 x\right) \quad \text{Eq. 14}$$

where:

- $c [M L^{-3}]$ is the effluent particle concentration;
- $c_0 [M L^{-3}]$ is the influent particle concentration;
- $\varepsilon [-]$ is the effective porosity of the porous medium;
- $d_{50} [L]$ is the mean grain size;
- $\eta_0 [-]$ is the single-collector contact efficiency (see 3.3.2);
- $\alpha [-]$ is the attachment efficiency (see 3.3.3).

The main hypotheses of this model are (Logan, Jewett, Arnold, Bouwer, & O'Melia, 1995):

- a) Single collector: presence of an isolated collector in an infinite fluid domain;
- b) Early stages of deposition (or clean-bed filtration): the few deposited particles do not have any influence on the ones incoming;
- c) Irreversible process: there cannot be detachments of the deposited particles.

A simplified representation of clean-bed filtration is presented in Figure 20.

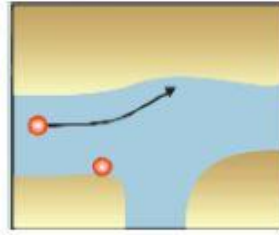


Figure 20 A representation of clean-bed filtration theory (Tosco, Gastone, & Sethi, 2014)

Starting from Eq. 14, the CFT removal rate $k_{CFT} [T^{-1}]$ can be evaluated using Eq. 15, in which $v [L T^{-1}]$ represents the pore velocity of the flowing fluid (Parker, et al., 2017).

$$k_{CFT} = \frac{3(1-\varepsilon)}{2d_{50}}\alpha\eta_0 v \quad \text{Eq. 15}$$

When studying the mobility of nZVI particles in porous media, however, it is difficult to describe their behavior simply referring to the CFT, because it is apparent that in many cases the hypotheses on which it is based are not valid. The CFT supposes that each particle does not sense the presence of the others; instead, the iron particles may have interactions among them and with the already deposited particles, and this deeply affects their behavior. In addition, the deposition of particles (which can be reversible) may vary the porosity of the collector causing clogging of the porous medium. Therefore, a more elaborate transport model is often required.

3.3.5. Model for the transport of nZVI particles

The transport of nanoscale zerovalent iron in saturated porous media can be described with a modified advection–dispersion equation, which accounts for the non-equilibrium interactions between particles both in the liquid and in the solid phase (Tosco & Sethi, 2010) (Tiraferri, Tosco, & Sethi, 2011). The unidimensional model is expressed with the following equations:

$$\begin{cases} \frac{\partial(\varepsilon c)}{\partial t} - \sum_i \frac{\partial(\rho_b S_i)}{\partial t} = -\frac{\partial(qc)}{\partial x} + \frac{\partial^2(\varepsilon Dc)}{\partial x^2} \\ \frac{\partial(\rho_b S_i)}{\partial t} = \varepsilon k_{a,i} \Phi_i c - \rho_b k_{d,i} S_i \end{cases} \quad \text{Eq. 16}$$

where:

- ε [–] is the effective porosity of the porous medium;
- c [$M L^{-3}$] is the particle concentration in the liquid phase;
- ρ_b [$M L^{-3}$] is the bulk density of the solid matrix;
- S [–] is the particle concentration in the solid phase;
- q [$L T^{-1}$] is the Darcy's velocity;
- D [$L^2 T^{-1}$] is the dispersion coefficient;
- k_a [T^{-1}] is the attachment rate coefficient;
- k_d [T^{-1}] is the detachment rate coefficient.

In addition, the variable Φ in the attachment term represents a generic function that varies according to the attachment mechanism used to describe the transport in every specific situation. In the hypothesis of validity of CFT, for instance, the attachment term would be described by a Φ function equals to 1, and k_a could be written as k_{CFT} (see 3.3.4); then, the detachment term, accordingly to the CFT assumptions, would be zero.

In a more generic situation, k_a becomes a parameter that contains all the variables of the problem, and it is adjusted by the specific function Φ chosen. A similar case happens for k_d , with the difference that this term is always considered linear in the present model. The terms k_a and k_d become therefore the most important parameters to evaluate through experimental tests: knowing them is the prerequisite for any further consideration on particle transport behavior.

Finally, another consideration on Eq. 16 is required. The presence of the summation term with subscript i , regulating the exchange of particles between liquid and solid phase, means that more than a single deposition mechanism can be accounted for by the model. Each phenomenon is evaluated independently, then their effects are combined: additivity of single mechanisms is therefore assumed. However often, to avoid introducing too many variables in the equations, a maximum of two coexisting phenomena is adopted ($i = 1, 2$).

In the following, the main deposition processes are listed, together with their specific Φ functions (Bianco, Tosco, & Sethi, 2018). For the sake of conciseness, the subscript i , indicating concurrent deposition mechanisms, will be dropped where not strictly needed.

Linear reversible attachment

The linear reversible attachment is the simplest case possible. It may occur when particle–collector and particle–particle interactions have similar intensity. Its description is alike clan-bed filtration, with the difference that k_a does not have a fixed expression, and therefore must be evaluated from experimental tests. The function Φ is equal to 1.

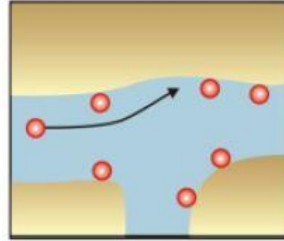


Figure 21 Linear reversible attachment (Tosco, Gastone, & Sethi, 2014)

Blocking phenomenon

Blocking phenomenon can happen when particle–particle repulsions are stronger than particle–collector ones. This mechanism expresses the fact that previously deposited particles hinder the deposition of the incoming ones: there is therefore a maximum level of particle attachment, expressed by:

$$\Phi = 1 - \frac{S}{S_{max}} \quad \text{Eq. 17}$$

in which S_{max} [–] represents the maximum concentration retainable on the grains at given chemical conditions.

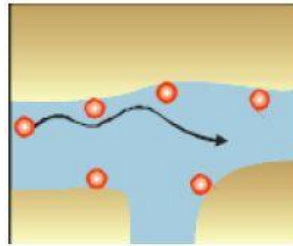


Figure 22 Blocking phenomenon (Tosco, Gastone, & Sethi, 2014)

Ripening phenomenon

Ripening phenomenon is typical of attractive particle–particle interactions: the affinity between particles is so high that the deposited attract the incoming ones, continuing to increase their concentration in the solid phase. This condition may be described as:

$$\Phi = 1 + A_{rip} S^{\beta_{rip}} \quad \text{Eq. 18}$$

in which A_{rip} [–] and β_{rip} [–] represent the ripening coefficients, both greater than zero.

This mechanism often determines *clogging* of the porous medium, because the deposited particles slowly start to obstruct the pores of the medium.

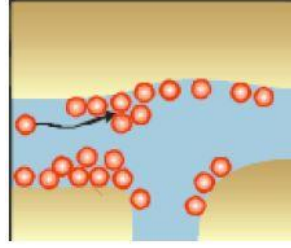


Figure 23 Ripening phenomenon (Tosco, Gastone, & Sethi, 2014)

Straining phenomenon

As indicated by Tosco and Sethi (Tosco & Sethi, 2010), the term *straining* includes a pair of phenomena that lead to an increased deposition of the suspended particles. In particular, it is defined straining the process of aggregation and subsequent filtration of the newly formed clusters of colloids, more easily retained into the pores of the medium.

The increased deposition can be modeled as follows:

$$\Phi = \left(1 + \frac{x}{d_{50}}\right)^{-\beta_{str}} \quad \text{Eq. 19}$$

in which $x [L]$ is the distance travelled by the particles in the porous medium and $\beta_{str} [-]$ represents the straining coefficient, controlling the particle spatial distribution. Experimental tests have shown that β_{str} can usually be assumed equal to 0.432 (Bradford, Simunek, Bettahar, van Genuchten, & Yates, 2003).

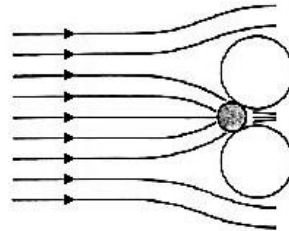


Figure 24 Straining phenomenon (C-vac)

The abovementioned mechanisms are strongly affected by several parameters. The main influences will be described briefly below, while a more detailed formulation of the phenomena will be given in section 4.3.3, where the transport model implemented in the software MNMs will be explained.

The major parameters that regulate the attachment/detachment mechanisms are:

- a) Ionic strength;
- b) Porous medium clogging;
- c) Mobile phase viscosity;
- d) Flow velocity.

Ionic strength

As already mentioned in Section 3.3.3.3, the ionic strength plays an important role in the determination of particle–particle and particle–collector interactions. In effect, a change in ionic strength determines a variation of the attachment and detachment coefficients, as well as of maximum blocking concentration.

Porous medium clogging

The process of clogging is a progressive occlusion of the medium pores due to deposition of particles, accompanied by a reduction of permeability and porosity of the formation. A model that accounts for the clogging of porous medium must solve a system of coupled equations, which evaluate the change in the flow due to the sedimentation particles; this change in the flow, in turn, affects the deposition mechanisms, and so on. Moreover, this phenomenon is also responsible of the pressure buildup caused by particle deposition and consequent permeability reduction.

Mobile phase viscosity

As explained in Section 3.3.3.4, the presence of polymers in a colloidal system can effectively improve its stability, thanks to the steric interactions which prevent aggregation of particles; in addition, the increased viscosity of the fluid usually caused by the presence of polymers hinder the sedimentation of the particles, according to Stokes's law.

Furthermore, the polymeric substances frequently used in field applications (e.g. CMC, guar gum, xanthan gum, etc.) tend to exhibit a non-Newtonian rheological behavior, with viscosities that slowly decrease at high shear rates. This peculiar behavior affects the transport of nanoparticles and has an important influence on the pressures that originates in aquifers during an injection ([Gastone, Tosco, & Sethi, 2014b](#)) ([Xue & Sethi, 2012](#)).

Flow velocity

The phenomena of attachment and detachment are strongly influenced by the velocity of the flow. In general, the higher the flow velocity, the higher the attachment and detachment rates. In a column test, the fluid flows with a constant velocity, therefore the test allows the determination of k_a and k_d for that specific velocity.

In a field application, it is necessary to abandon the one-dimensional description of the phenomena and the simplest way of doing so is supposing a radial symmetry domain around the injection well. In case of radial geometry, the equations describing the transport and the deposition mechanisms become:

$$\begin{cases} \frac{\partial(\varepsilon c)}{\partial t} - \sum_i \frac{\partial(\rho_b S_i)}{\partial t} = -\frac{1}{r} \frac{\partial(rqc)}{\partial r} + \frac{1}{r} \frac{\partial}{\partial r} \left[r \varepsilon D_r \frac{\partial c}{\partial r} \right] \\ \frac{\partial(\rho_b S_i)}{\partial t} = \varepsilon k_{a,i} \Phi_i c - \rho_b k_{d,i} S_i \end{cases} \quad \text{Eq. 20}$$

where:

- $\varepsilon [-]$ is the effective porosity of the porous medium;
- $c [M L^{-3}]$ is the particle concentration in the liquid phase;
- $\rho_b [M L^{-3}]$ is the bulk density of the solid matrix;
- $S [-]$ is the particle concentration in the solid phase;
- $q [L T^{-1}]$ is the Darcy's velocity;
- $D_r [L^2 T^{-1}]$ is the dispersion coefficient, in radial direction;
- $k_a [T^{-1}]$ is the attachment rate coefficient;
- $k_d [T^{-1}]$ is the detachment rate coefficient.

In accordance with this formulation, the flow velocity now decreases hyperbolically with the distance, as expressed below.

$$q = \frac{Q}{2\pi r b} \quad \text{Eq. 21}$$

Where $q [L T^{-1}]$ is the Darcy's velocity, $Q [L^3 T^{-1}]$ is the flow rate, $r [L]$ is the distance from the injection well and $b [L]$ is the length of the well screening.

A representation of the phenomenon is given by Tosco et al. (Tosco, Gastone, & Sethi, 2014), and it is reported in Figure 25.

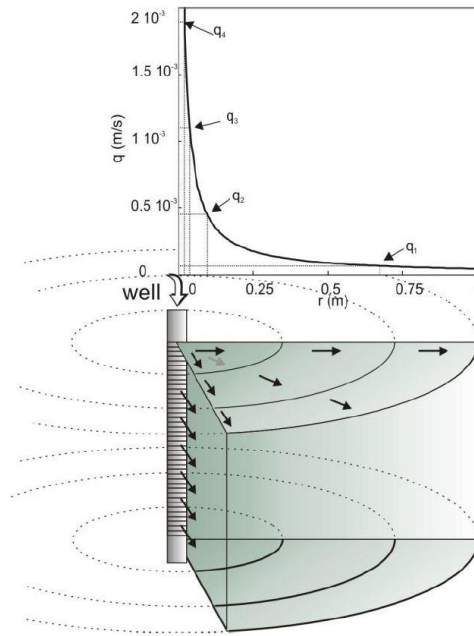


Figure 25 Hyperbolic decrease of Darcy's flow velocity in a radial domain (Tosco, Gastone, & Sethi, 2014)

In these conditions, the hyperbolic decrease of flow velocity with the distance affects the mechanisms of attachment and detachment in each point of the domain; to adapt the k_a and k_d coefficients to this situation, a modified formulation has been proposed by Tosco et al. (Tosco, Gastone, & Sethi, 2014):

$$k_a = C_a \frac{\eta_0}{d_{50}} v \quad \text{Eq. 22}$$

$$k_d = C_d \mu_m v \quad \text{Eq. 23}$$

where:

- C_a [–] and C_d [$T M^{-1}$] are empirical parameters including all other phenomena not accounted for in this formulation e.g. ionic strength, pH, etc.
- η_0 [–] is the single-collector contact efficiency (see 3.3.2);
- d_{50} [L] is the average diameter of the porous medium;
- v [$L T^{-1}$] is the pore velocity (or *effective*) of the flowing fluid;
- μ_m [$M L^{-1} T^{-1}$] is the viscosity of the liquid fluid.

4. Materials and methods

4.1. Main materials used in the experiments

In this section a brief description of the materials used in the experiments is provided. In particular, the focus is placed on the water used to prepare the iron suspensions, on the polymer added to stabilize them, on the kind of nZVI particles utilized, and on the sand employed to recreate the porous medium.

4.1.1. VEGAS degassed water

To simulate aquifer conditions, in which the quantity of dissolved oxygen (DO) is very low, degassed tap water has been chosen to prepare the suspensions of iron particles. To ensure that this condition was respected at all times, a constant checking of the degassing device has been carried out. The data collected showed a value of DO always below 1.2 mg/L in the moment when the water was collected to prepare the suspensions. A low concentration of dissolved oxygen in the water was also essential to prevent a promptly oxidation of the iron once the nanoparticles were added (ref. 3.2.2).

Furthermore, to work in conditions similar to those present in field, it was decided not to perform a deionization of the tap water, which therefore contained some dissolved species. Laboratory analysis performed at VEGAS in 2014, reported the parameters for the tap water shown in Table 2 (Giannelli, 2014).

Table 2 Properties of VEGAS degassed water. Adapted from (Giannelli, 2014)

Parameter	U.M.	Value
pH (9°C)	[-]	7.97
Dissolved oxygen	[mg/L]	1
TOC ⁹	[mg/L]	1
Nitrate	[mg/L]	4.2
Nitrite	[mg/L]	<0.005
Sulfate	[mg/L]	34
Calcium carbonate	[mmol/L]	1.6
Electrical conductivity (25°C)	[μS/cm]	333
Sodium	[mg/L]	5.2
Calcium	[mg/L]	48
Magnesium	[mg/L]	8
Potassium	[mg/L]	1.4
Chloride	[mg/L]	7

⁹ "The *total organic carbon* (TOC) is a measurement method for the content of carbon of dissolved and undissolved organic substances in water." (LAR - Process Analysers AG)

4.1.2. Sodium carboxymethyl cellulose

Carboxymethyl cellulose (CMC) is a derivative of cellulose, synthesized from its reaction with chloroacetic acid (Hollabaugh, Burt, & Walsh, 1945). After CMC formation, a purification process is needed to obtain a pure product, removing the salts produced during the synthesis reactions. Unlike cellulose, the polar carboxyl groups in the CMC molecule make this substance soluble in water and chemically reactive.

CMC is often used in the form of its sodium salt, *sodium carboxymethyl cellulose*, which appears as a white powdered solid, almost odorless (FAO monograph, 1992). It is employed in several different fields such as pharmaceutical, food and in many industrial applications, mostly for its properties of thickener and binder. Because of its characteristics of being innocuous, inexpensive and commercially available, it might be successfully used in nanoremediation applications. In effect, as reported by Saberinasr et al. (Saberinasr, Rezaei, Nakhaei, & Hosseini, 2016), the technique of coating the nZVI particles with CMC to enhance their mobility and to hinder particle aggregation and deposition has been investigated in many studies (He, Zhang, Qian, & Zhao, 2009) (Lin, Tseng, Wey, & Lin, 2010) (Raychoudhury, Tufenkji, & Ghoshal, 2012).

It is known that dissolving CMC in water results in an increase of the solution viscosity. The rheological behavior of CMC solutions at different concentrations has been studied by Benchabane and Bekkour (2008). Working with a product with nominal molecular weight of $700000 \text{ g} \cdot \text{mol}^{-1}$ and a *degree of substitution*¹⁰ of 0.65 – 0.85 supplied from Sigma-Aldrich, they obtained the results reported in Figure 26.

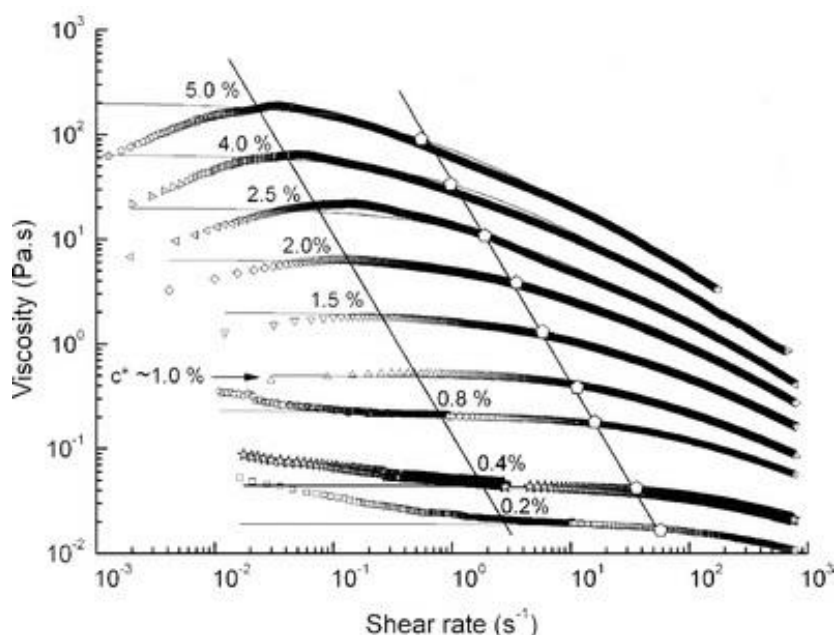


Figure 26 Viscosity versus shear rate for CMC solutions at different concentrations (Benchabane & Bekkour, 2008)

¹⁰ "The *degree of substitution (DS)* equals the number of hydroxyl groups replaced by the substituent per glucose unit in the chain of cellulose." (Bonet, Quijada, Muñoz, & Cases, 2005)

The previous graph demonstrates the expected increase in viscosity due to an increase in the CMC concentration. Moreover, it shows that the rheological behavior of the solutions changes with shear rates. In detail, it is possible to distinguish three regions. At high shear rates, the shear-thinning behavior of the solutions is showed, with viscosities decreasing with an increase of shear rate. In the central region of the graph instead, the viscosity stays essentially constant. Finally, at low shear rates, the properties of the solutions seem to change with the concentration of CMC, showing a shear-thinning behavior for concentration below 1%, a shear-thickening behavior for higher values.

Besides, the solutions prepared with CMCs from different producers may have different behaviors, and even a single producer can fabricate different products. In effect, an important factor that affects the rheological characteristics of this substance is the length of its polymeric chains i.e. its *degree of polymerization* (DS) ([The DOW Chemical Company](#)).

During the experimental work of the present thesis the commercial CMC Walocel CRT 30 GA, supplied from the American company DOW Chemical, has been used. A schematic representation of its polymeric chain is given in Figure 27 ([The DOW Chemical Company](#)). Throughout the experiments, an extensive characterization of the rheological behavior of this particular CMC has been conducted as the basis for further investigations on stabilized iron suspensions.

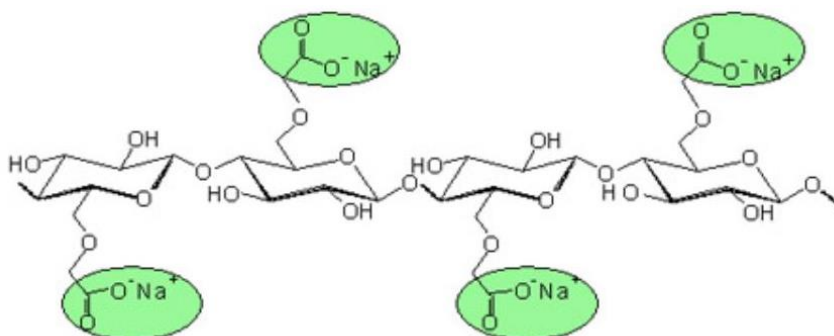


Figure 27 Structure of WALOCCEL ([The DOW Chemical Company](#))

4.1.3. NANO FER STAR nZVI particles

There are different nZVI particles available on the market, e.g. Carbo-Iron, NANO FER 25P, NANO FER 25S, etc. However, in this work exclusively NANO FER STAR, produced by NANO IRON s.r.o. (Czech Republic), has been studied. The choice of the product descended from the numerous favorable properties claimed by the producer ([NANO IRON s.r.o.](#)):

- NANO FER STAR is stabilized by a thin inorganic surface layer (4 nm ca.) that protects nZVI against quick oxidation in contact with air;
- Despite the stabilization in air, the product keeps the maximum reactivity in water;
- It is in powder form: it is therefore easy to ship, to handle and to use;
- It has practically unlimited storage time in sealed packaging;
- It is known that its migration properties improve with addition of CMC.

NANO IRON declares the following composition for its NANOFE[®] STAR, in powder form:

Table 3 Basic characteristics of NANOFE[®] STAR in powder form

Fe⁰ content [% weight]	Iron oxide content [% weight]
≥ 65-80%	35-20%

Throughout the experimental work, two different batches of this product have been used. In any case the nominal concentration of ZVI was virtually the same (about 77.0%), therefore the observed characteristics are unlikely affected by this situation.

As indicated by the producer itself, manufactured nanoparticles have a nominal dimension of about 50 *nm*. However, they come in form of clusters and agglomerates (ref. Figure 28), therefore, prior to their use, it is necessary to *activate* them by preparation of an aqueous suspension (slurry) (NANO IRON s.r.o. - NANOFE[®] STAR manual).

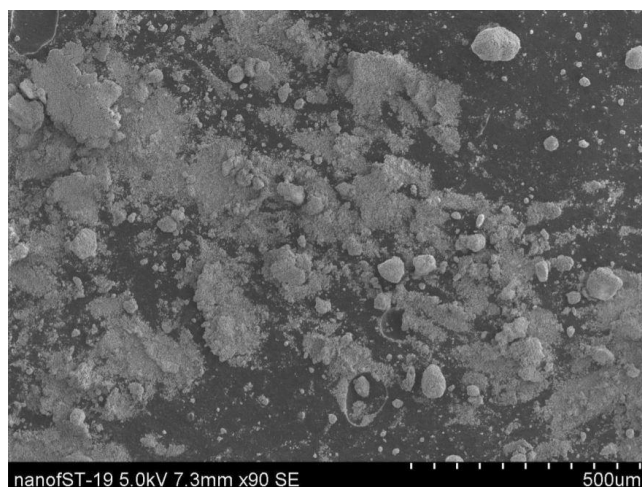


Figure 28 SEM image of NANOFE[®] STAR in powder form (NANO IRON s.r.o. - NANOFE[®] STAR manual)

The process of activation is described more in detail in section 4.2.2. The result of this procedure is the destruction of aggregates, leading to a significant increase of the surface area of the particles, together with an increase in reactivity (Giotti, 2017); moreover, smaller particles are expected to travel longer distances in porous media. A representation of activated NANOFE[®] STAR particles is provided in Figure 29.

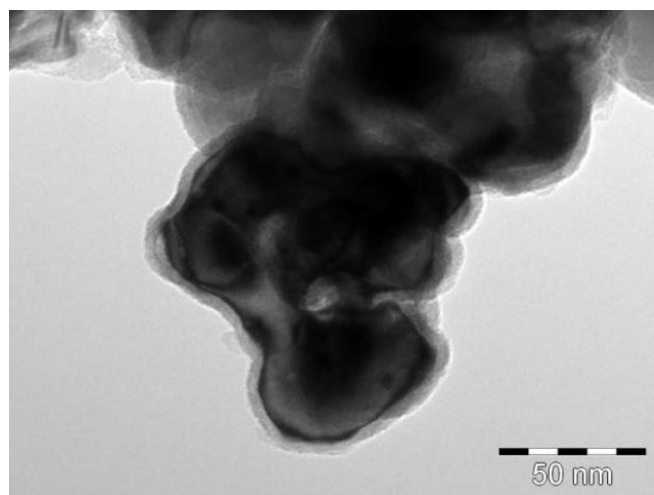


Figure 29 TEM image of activated NANO FER STAR (NANO IRON s.r.o. - NANO FER STAR manual)

4.1.4. Porous medium

For the column tests performed in this thesis, two kinds of porous medium have been used. The first medium was composed uniquely of Dorsilit 8 FG, a homogeneous crystal quartz sand produced by the German company Dorfner GmbH, with grains in between 0.3 and 0.8 mm, and $d_{50} = 0.57$ mm. An important property of this sand is the low content of iron oxides (0.01% ca. in weight), so that during the experiments the mobility of nZVI is not affected by the iron already present in the porous medium.

The German company Frieser-München reports the following characteristics for Dorfner Dorsilit 8 (Frieser-München, 2011):

Table 4 Grain distribution of Dorfner Dorsilit 8 (Frieser-München, 2011)

size [mm]	Pass. [%]
> 1	traces
> 0.8	1
0.63 - 0.8	37
0.315 - 0.63	60
< 0.315	2

However, another producer provided a complete granulometric curve for its Dorsilit 8 (0.3 – 0.8 mm); the graph is reported in Figure 30. The properties of this sand should reflect the ones of the sand supplied from Dorfner GmbH.

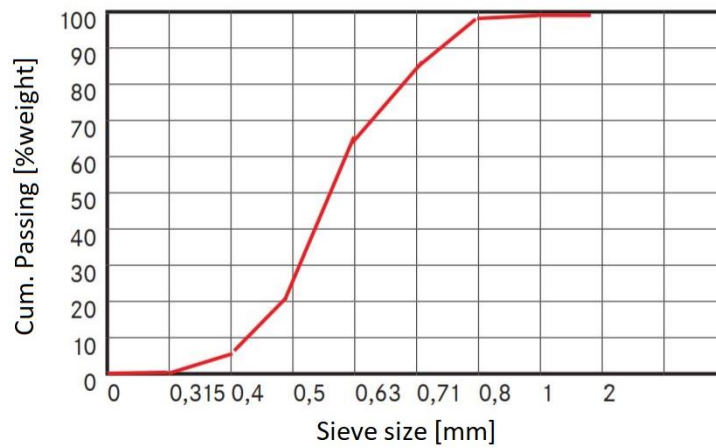


Figure 30 Granulometric curve for Dorsilit 8. Adapted from (QUARZSANDE, 2012)

As mentioned above, the Dorsilit 8 is a homogeneous sand. This condition, often very useful for laboratory experiments, is not very representative of a real situation where, usually, the solid grains composing the soil are in fact very heterogeneous, in size and shape. For this reason, at VEGAS several former experiments have been performed using the heterogeneous soil present in that area of Stuttgart (referred to as *VEGAS soil* or *VEGAS sand*). However, this medium has a non-negligible natural content of iron; hence it does not seem suitable for being used in tests with iron nanoparticles, because it may lead to misinterpretations of the results. Thus, the granulometry of the VEGAS soil was artificially reproduced by mixing in the right proportions three different kinds of Dorsilit sands. The result was a sand with a granulometric distribution matching the one of the actual VEGAS soil, but having a much lesser content of iron; this mixture has been used as the second porous medium for the experiments of the present thesis.

The Dorsilit sands used to recreate VEGAS soil are described below (ref. Table 5), while a complete granulometric curve of the mix is given in Figure 31, both from Miyajima and Accolla (Miyajima, 2015) (Accolla, 2017), in comparison with the actual VEGAS sand.

Finally, two pictures showing the reproduced and the actual VEGAS sand are shown in Figure 32.

NB: Since in this thesis only reproduced VEGAS sand has been used, in the following sections this specification may be omitted, where not required from the context.

Table 5 Dorsilit sands reproducing VEGAS soil. Adapted from (Miyajima, 2015)

Parameter	U.M.	Sand 1	Sand 2	Sand 3
Grain size distribution	[mm]	0 to 4	0 to 4	0.2 to 8
Porosity	[-]	0.34	0.34	0.4
Particle density	[Kg/m ³]	2.65E+03	2.65E+03	2.65E+03
Bulk density	[Kg/m ³]	1.7E+03 to 1.8E+03	1.72E+03	1.59E+03
Permeability	[m ²]	4.1E-11 to 14.3E-11	4.1E-11 to 14.3E-11	3.6E-10 to 6.1E-10
Hydraulic conductivity*	[m/s]	4.1E-04	4.1E-04	9.3E-03
Hydraulic conductivity**	[m/s]	-	4.3E-04	4.5E-03

* measured with constant head permeameter

** based on tracer experiment in large scale container experiment

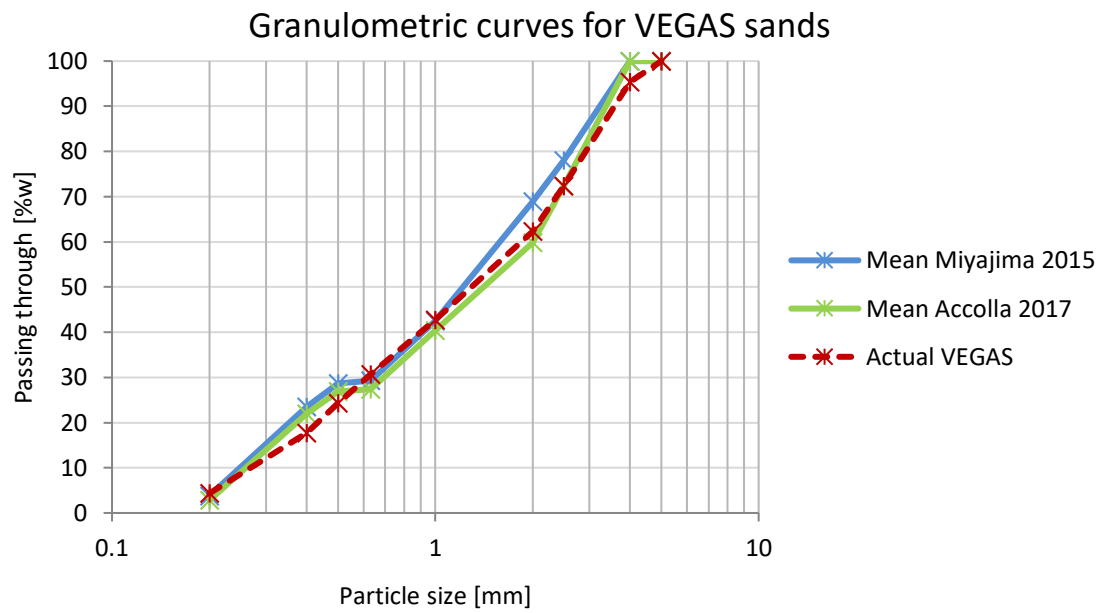


Figure 31 Grain size distribution of actual and reproduced VEGAS sands. Adapted from (Accolla, 2017)



Figure 32 Reproduced (left) and actual (right) VEGAS sands

4.2. Instruments and procedures used in the experiments

In the following sections the most relevant procedures applied during the experimental work will be presented, also focusing on the measurement systems and on their operating principles. Most of the measurements have been performed at VEGAS institute, in Stuttgart. Some further experiments have been carried out at Politecnico di Torino.

4.2.1. Preparation of CMC solutions

The preparation of the solution with the stabilizing polymer has been carried out in a very simple way. After having collected the required volume of VEGAS degassed water and having weighted the desired amount of CMC, the powder was dissolved in water mixing with a disperser IKA T25 digital ULTRA-TURRAX (see Figure 33) for 5 minutes, at ca. 22000 *rpm*. The procedure was performed in 1 L bottles. Finally, the prepared solutions were left to stand for 2 days before being used.



Figure 33 Preparation of a CMC solution

4.2.2. Activation of NANO FER STAR

As suggested from the producer, the NANO FER STAR particles must be activated before use. The activation process has always been performed in VEGAS degassed water, in 100 mL bottles. It consisted in mixing the iron powder in water for 6 minutes at about 10000 *rpm*. Argon, an inert gas, has been used to flush the headspace of the bottles during the entire procedure, in order to hinder the solubilization of the air oxygen into the sample and prevent its oxidation. In conclusion, the activated nanoparticles were left to stand for 1 to 2 days, as recommended by the manufacturer ([NANO IRON s.r.o. - NANO FER STAR manual](#)).

4.2.3. Preparation of NANOFER STAR suspensions

When the nanoparticles were ready, it was possible to prepare the desired suspensions. In the case of an aqueous suspension, the particles in the small bottles were simply agitated with the ULTRA-TURRAX for 1 minute at 10000 *rpm*, then added into a 1 L bottle containing the required amount of degassed water and finally mixed at 22000 *rpm* for further 5 minutes. In the case of a CMC-stabilized suspension a similar procedure has been followed. The only difference was that the particles, after being mixed for 1 minute, were added into a 1 L bottle containing CMC with such a concentration that the addition of the new volume created the desired final concentrations of both particles and of polymer. After that, the mixing for 5 minutes completed the procedure.

It is important to highlight that, in both cases, the mixing phases were associated with an argon flushing of the headspace, to impede a contact of the samples with air.

Eventually, the newly created suspensions have been immediately used for the experiments. An example of suspension is shown below.



Figure 34 Picture of a NANOFER STAR suspension

4.2.4. Measurements of pH, electrical conductivity and dissolved oxygen

On several occasions it was necessary to measure one or more parameters of water, CMC solutions or iron suspensions. The measurements of pH, electrical conductivity and dissolved oxygen have been performed with the portable multimeter (HQ40d, HACH, US) shown below.



Figure 35 HQ40d Portable multimeter: pH, conductivity and dissolved oxygen for water



Figure 36 Measuring with HQ40d Portable multimeter

4.2.5. Determination of nZVI in NANOFER STAR suspensions and in solid samples

To evaluate the concentration of Fe^0 into the suspensions of NANOFER STAR, the *hydrogen evolution method* has been used (Comba & Braun, 2012). The addition of a known amount of hydrochloric acid (HCl) into the liquid sample causes a certain amount of hydrogen to develop, thanks to the reactions between Fe^0 and the acid. By measuring the volume of the resultant hydrogen, it is possible to determine the quantity of the initial ZVI in the sample.

Furthermore, the same procedure may be followed for the determination of ZVI deposited in the sand grains of a porous medium.



Figure 37 Hydrogen evolution method: analysis

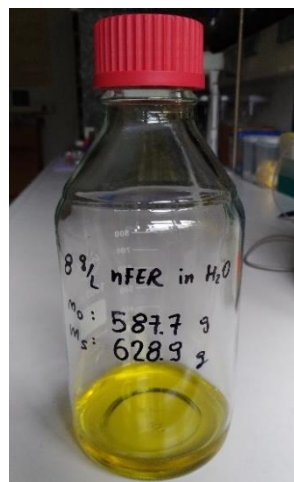


Figure 38 Hydrogen evolution method: end of test

4.2.6. Sedimentation tests

At Politecnico di Torino, some sedimentation tests on NANOFER STAR suspensions have been performed, with the objective of having a temporal indication of their stability. Each suspension was inserted into an elongated cuvette, where it slowly started to sediment. In the meanwhile, a magnetic susceptibility meter measured the signal in a fixed point of the cuvette at least until it halved; the well-known direct proportionality between magnetic susceptibility and iron concentration allowed to draw a parallelism between the halving of the signal and the halving of the initial particle concentration.

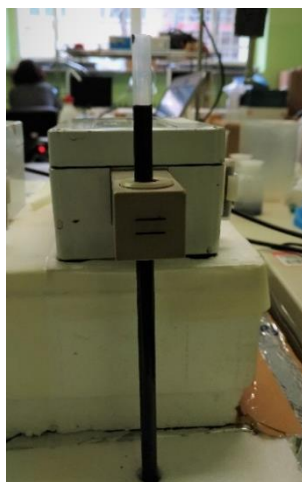


Figure 39 Magnetic susceptibility meter during a sedimentation test

4.2.7. Measurement of specific surface area of NANOER STAR

The determination of the specific surface area of NANOER STAR particles in a suspension has been carried out via BET measurements (named after Brunauer–Emmett–Teller theory). These scientists, in their theory, found out that the specific surface area of a powder could be evaluated by calculating the quantity of gas physically adsorbed around the solid grains ([Particle Analytical](#)). Before the analysis the samples were freeze-dried in an Alpha 1-2 freeze-dryer produced by Christ; the actual BET analysis has been conducted with a SA 3100 BET analyzer from Beckman Coulter, Inc. The two instruments are shown in Figure 40 and Figure 41 respectively, while a picture of a dried sample is presented in Figure 42.



Figure 40 Freeze-dryer from Christ



Figure 41 BET instrument from Beckman Coulter, Inc. (Giotti, 2017)

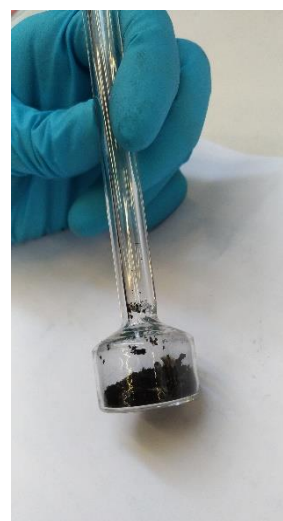


Figure 42 Dried sample for BET measurement

4.2.8. Measurements of particle size and zeta potential

Measurements of particle size and zeta potential of NANOER STAR have been carried out both at VEGAS and at Politecnico di Torino, with different equipment. In the following, the techniques applied will be briefly described.

4.2.8.1. Acoustic and electroacoustic spectrometry

At VEGAS, the evaluation of NANOER STAR particle size and zeta potential has been performed with the acoustic and electroacoustic spectrometer (DT-1200, Dispersion Technology Inc., US). The operating principle of an acoustic spectrometer is quite simple. The instrument generates sound pulses that are measured by a receiver after having passed through the colloidal system in question. This passage in the sample changes the intensity and the phase of the sound energy emitted. The spectrometer measures the sound energy loss (often called *attenuation*) and the sound speed, which depend on the interaction of the sound waves with the sample. Finally, the experimental attenuation data are fitted to relatively complex theoretical models in order to obtain the particle size distribution (PSD) of the sample by weight, i.e. the curve showing the contribution to the total mass of the sample given by each fraction of particles with similar dimension.

Instead, electroacoustics works on a more complex principle, discovered by Debye in 1933 (Debye, 1933). In short, the electroacoustic spectrometer applies a sound energy to a sample and then it detects and measures the resultant electric field (or current) created by the vibration of the electrical double layers of the colloids (phenomenon called Colloid Vibration Current, CVI). This measure provides a characterization of the sample zeta potential (Dukhin & Goetz, 2001). The DT-1200 contains both the acoustic and the electroacoustic sensors; therefore, it can give information both on particle size distribution and on zeta potential of the suspensions (Dispersion Technology Inc.). The measurement system is shown in Figure 43, together with the disperser ULTRA-TURRAX T25 (Janke & Kunkel, IKA - Labortechnik) used to keep the nZVI particles suspended during the measurement. The suspension was continuously circulated into the pipes and mixed until the test was complete. Lastly, a detail of the measuring chamber of acoustic phenomena is provided in Figure 44.

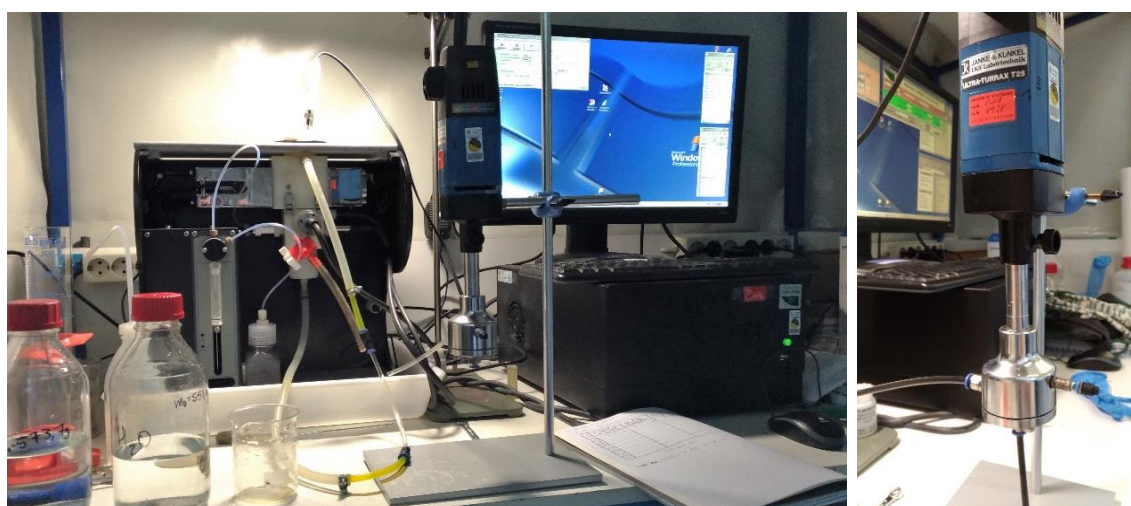


Figure 43 Acoustic-electroacoustic spectrometer (left) and dispersing system (right)

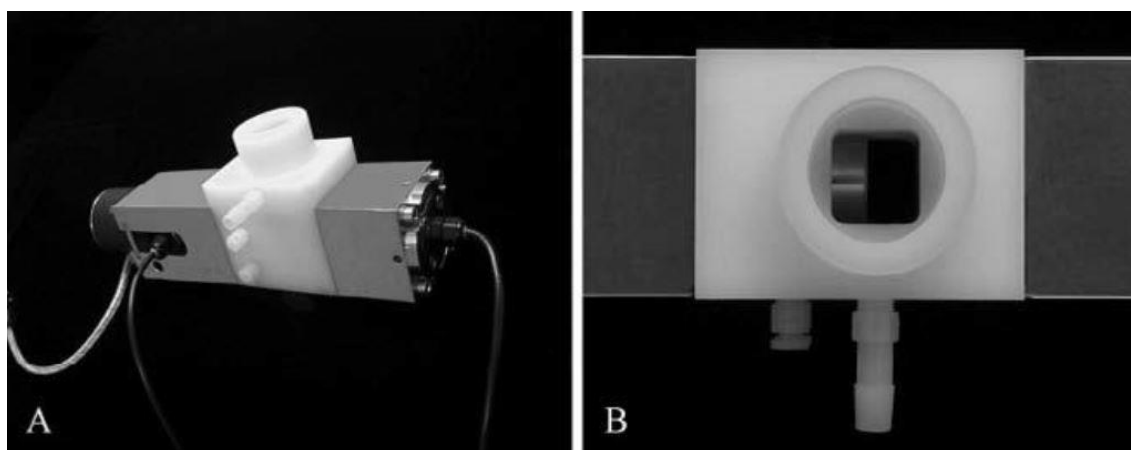


Figure 44 Acoustic sensor. Pseudo-frontal (A) and top (B) views (Dukhin & Goetz, 2010)

To achieve a validation of the results given by the spectrometer, further analyses have been performed at Politecnico di Torino, using different instruments: a CPS Disc Centrifuge for the investigation of particle size and a Malvern Zetasizer Nano for the determination of zeta potential of iron particles and sand grains.

4.2.8.2. Differential centrifugal sedimentation

At Politecnico di Torino, particle size has been evaluated with a Disc Centrifuge from CPS (see Figure 45). Its principle of operation is quite simple. The rotations of the central disc separate the injected particles because of a phenomenon called *differential centrifugal sedimentation* (DCS), according to which the bigger particles settle much earlier than the smaller ones; this process is stabilized by the presence of a liquid with a slight density gradient within the disc. The particles sediment inside this transparent disc and, when they approach its outside edge, they interact with a light beam that passes through it. The variation in light intensity is continuously recorded by the instrument and converted by the software into a particle size distribution ([CPS Instruments Europe](#)), which can be displayed, among the others, by weight or by number of particles. A frontal view and a cross-sectional representation of the disc are shown in Figure 46.



Figure 45 Disc centrifuge from CPS Instruments, Inc.

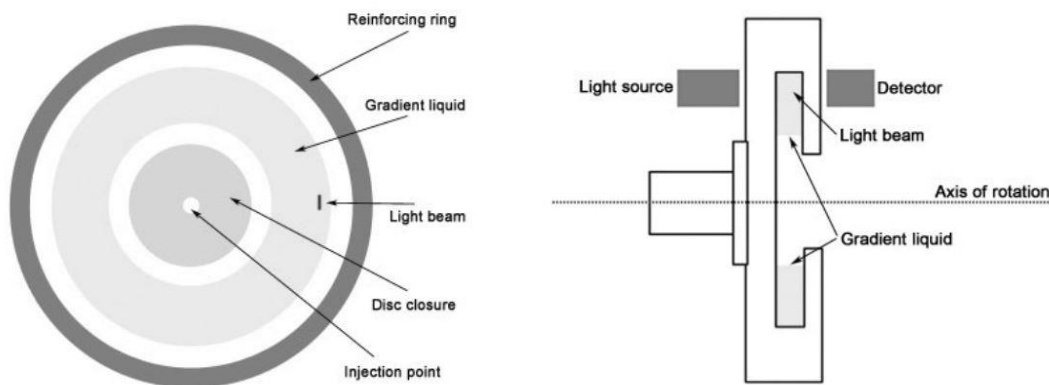


Figure 46 Frontal (left) and cross-sectional (right) views of the centrifuge disc ([CPS Instruments Europe](#))

4.2.8.3. Electrophoresis

The zeta potential of NANOFER STAR particles in different suspensions as well as the one of the sand grains of the medium have been determined at Politecnico di Torino with a Zetasizer Nano, from Malvern. These results completed the measurement campaign already performed at VEGAS.

The Zetasizer is based on the principle of *laser doppler electrophoresis* (LDE): when an electric field is applied to a dispersion of particles, they move in the measuring cell with a velocity related to the interaction between charged particles and applied field. This velocity, proportional to the energy potential of the particle at the slip plane (i.e. zeta potential), is measured by detecting the Doppler shift in the scattered light. Therefore, this optical measurement can be used to evaluate the zeta potential of a dispersion ([Malvern Instruments](#)) ([St. Petersburg State University](#)). A representation of the instrument and of the measuring cell is provided below.



Figure 47 Zetasizer Nano (left) and measuring cell (right) (Malvern Instruments)

4.2.9. Filling and saturation of the columns

Experimental work required the preparation of two sets of columns (C1.n and C2.n), respectively filled with Dorsilit 8 and with reproduced VEGAS sand. The inner diameter of each column was 4.4 cm, while the length of the packed porous medium was around 50 cm. Column properties, provided in detail in 5.2.2, have been evaluated by weighting the columns at different stages of preparation. First, the empty column with the two stoppers (see Figure 48) and with the inlet and outlet tubes (about 70 cm long and 4 mm of diameter) had to be weighed. Later, the sand-packed column was weighed before and after saturation.



Figure 48 Disassembled stopper

In order to pack a quite homogeneous column for all its length, several tools have been used. In particular, a funnel with two wire grids at the bottom helped the filling and the distribution of the sand (Rad & Tumay, 1987); then a heavy metal cylinder was employed to further compact the porous medium. The abovementioned instruments are shown in Figure 49.



Figure 49 Top (left) and bottom (center) views of the funnel. On the right picture, funnel and metal cylinder are displayed together

Before being saturated with water, each column was flushed with approximately 4 L of argon to replace the air that may have entered during the filling procedure; thus, oxidation processes were hindered. The argon flushing is pictured in Figure 50. After that, at least 2 L of degassed water were injected into the column using a peristaltic pump (Masterflex L/S Series from Cole-Parmer, ref. Figure 51). Both the flushing and the saturation had to be carried out with low flow rates, to avoid any disturbance of the porous medium.

At the end of this process, the column should be completely saturated, and it can be used for following investigations. A complete column is shown in Figure 52.



Figure 50 Argon flushing procedure



Figure 51 Peristaltic pump used for saturation



Figure 52 Pictures of a filled and saturated column (C2.3)

4.2.10. Column properties: tracer and hydraulic conductivity tests

The evaluation of effective porosity of a packed porous medium is fundamental. The mobile phase that flows throughout the column can indeed move only in a fraction of the total pores, the ones connected to each other. It is very difficult to know a priori which is the porosity that allows the movement of the mobile phase, therefore the best way to determine it is to perform a tracer test; in addition, through this test also the dispersivity is evaluated.

Then, to assess the hydraulic conductivity of the columns, the relative test has been carried out.

4.2.10.1. Tracer tests

Tracer tests have been carried out for all columns with bromide, using a pulse input. At first, the probe of a bromide sensor was calibrated to transform the signal detected in the flow cell (mV) into a bromide concentration (mg/L). Later, the probe was used to detect the concentration of bromide flowing out of the column under consideration, pushed by the peristaltic pump presented before (ref. Figure 51). Finally, the *breakthrough curve*¹¹ was evaluated to obtain the effective porosity and the dispersivity of the porous medium. Specifically, the arrival time of the concentration peak gave information about the effective porosity, while the shape and width of the curve provided information on dispersivity. The setup used for the tracer tests is shown in Figure 53.

¹¹ "A *breakthrough curve* is defined as the plot of relative concentration of a given substance versus time, where relative concentration is the ratio of the actual concentration to the source concentration." (American Meteorological Society, 2012)



Figure 53 Experimental setup for tracer tests. From right to left: degassed water tank, peristaltic pump, sand-packed column and flow cell with bromide sensor

4.2.10.2. Hydraulic conductivity tests

Hydraulic conductivity describes the ease with which the water can pass through a porous medium, when submitted to a hydraulic gradient ([Indian Institute of Technology](#)). This property has been evaluated for the columns both prior to and after the experiments, allowing a comparison between the two conditions.

The experimental approach for the determination of hydraulic conductivity is based on Darcy's law for the flow of a fluid through a porous medium. The *constant head method*, specifically, uses the following equation:

$$K = \frac{Q L}{A \Delta h} \quad \text{Eq. 24}$$

where:

- $K [L T^{-1}]$ is the hydraulic conductivity;
- $Q [L^3 T^{-1}]$ is the flow rate through the porous medium;
- $L [L]$ is the thickness of the porous medium (in this case the length of the column);
- $A [L^2]$ is the column cross-section;
- $\Delta h [L]$ is the difference in hydraulic head.

NB: The ratio between Δh and L represents the abovementioned hydraulic gradient.

Eq. 24 allows the calculation of hydraulic conductivity K when all the other parameters are known. In effect, the length of the packed column L is known, as well as its cross section A . The difference in the hydraulic head Δh between the conditions upstream and downstream the column is easily measured. Finally, the flow rate Q can be simply calculated by measuring the volume of water collected at the outflow in a defined time.

The setup for the hydraulic conductivity experiments is shown in Figure 54; the pump keeping a constant hydraulic head (another peristaltic Masterflex L/S Series from Cole-Parmer) is not present in the framing.



Figure 54 Setup for hydraulic conductivity tests

4.2.11. Viscosity and rheologic behavior of CMC

An important part of the experimental work was focused on the determination of the rheological properties of the CMC solutions in which the iron particles were dispersed. The characteristics of the carrier have relevant consequences on the transport behavior of the suspensions. To achieve a thorough description of these attributes, viscosity measurements have been carried out using a rotational viscometer. Moreover, to ensure that the results were representative of the conditions that occur during a column test, further tests were conducted inside the columns. The two approaches are described below.

4.2.11.1. CMC analyses with viscometer

The rotational viscometer Physica Rheolab MC 1 (from Anton Paar GmbH) has been used at VEGAS for the determination of viscosity of CMC solutions. Specifically, measurements have been performed on CMC solutions at different concentrations to investigate the rheological properties of the fluids. The *concentric cylinder configuration* of the measuring system was chosen, as the more reliable for the analysis of low-viscosity liquids (Mezger, 2015). A representation of the viscometer and its configuration are presented in Figure 55 and in Figure 56.



Figure 55 Viscometer, top view (Physica - a Company by Anton Paar)

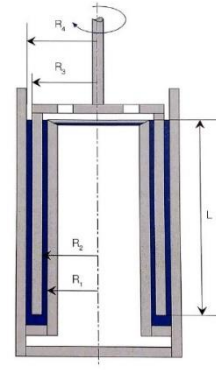


Figure 56 Concentric cylinder configuration of the viscometer (Mezger, 2015)

Finally, some viscosity data of CMC solutions were chosen, when performing radial injection simulations, from laboratory analyses conducted at Politecnico di Torino with a rheometer (Anton Paar Physica MCR 301).

4.2.11.2. CMC column tests

To investigate the rheological properties of CMC solutions inside the columns, as well as the rise in pressures caused by the injection, several column tests have been performed. In particular, the objective was to determine if different concentrations of polymer and different injection velocities (and therefore different shear rates) caused the fluid to exhibit a shear-thinning behavior. These tests have been conducted with the setup schematized in Figure 57.

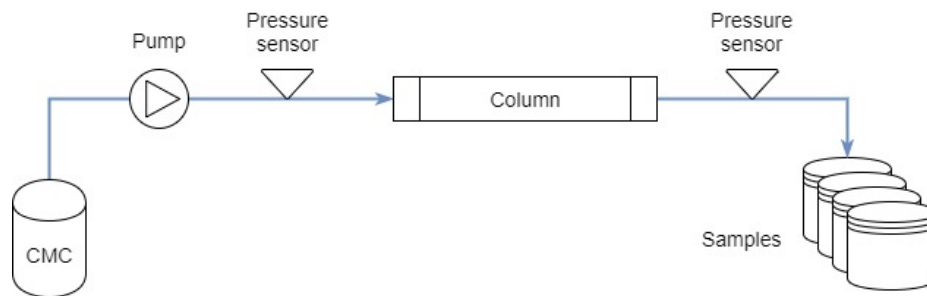


Figure 57 Scheme of experimental setup for CMC column tests

The pump represented in the diagram is again the Masterflex used for the saturation of the columns (ref. Figure 51); one of the pressure sensors (the one at the inflow) is shown below:



Figure 58 Inflow pressure sensor

This experiment is based on the following equation, representing the Darcy's law written in a general notation:

$$q = -\frac{k}{\mu} \Delta P \quad \text{Eq. 25}$$

where:

- $q [L T^{-1}]$ is the Darcy's velocity (or specific discharge);
- $k [L^2]$ is the intrinsic permeability of porous medium;
- $\mu [M L^{-1} T^{-1}]$ is the dynamic viscosity of the fluid;
- $\Delta P [M L^{-1} T^{-2}]$ is the pressure gradient between the two sensors.

By performing several injections with different velocities q and by measuring the consequent pressure gradients between upstream and downstream of a column, it was possible to build a graph showing the variation of ΔP as a function of q . Knowing that during the first stages of the injection the intrinsic permeability k is a constant parameter, depending only on the properties of the porous medium, a change in the slope of the curve would suggest a change in the dynamic viscosity of the fluid μ . In effect, a Newtonian fluid would appear in the graph as a straight line, while a shear-thinning fluid would have a curve with a slope becoming flatter and flatter; a shear-thickening fluid instead, would be represented by a curve with a slope getting gradually steeper with increasing velocities (and shear rates). The results of these tests will be reported in section 5.3.2, for different CMC concentrations.

Finally, it is important to underline that, to ensure that this method of analysis was applicable, it was necessary to check if the Darcy's equation could be used to describe the flow conditions inside the column. To do so, the calculation of the Reynolds number was made for the different injection velocities and for the different concentrations of CMC. The equation used is reported below:

$$Re = \frac{\rho q d_{30}}{\mu} \quad \text{Eq. 26}$$

where:

- $\rho [M L^{-3}]$ is the density of the fluid;
- $q [L T^{-1}]$ is the Darcy's velocity (or specific discharge);
- $d_{30} [L]$ is a representative grain diameter for the finer fraction in the porous medium;
- $\mu [M L^{-1} T^{-1}]$ is the dynamic viscosity of the fluid.

Historically, critical Reynolds values for non-Darcy flow in porous media range from 1 to 100 (Zeng & Grigg, 2006); in this work a Reynolds number in the order of 10^0 or less was considered to represent a laminar flow, well described by the Darcy's equation.

In addition, during these experiments it was also possible to evaluate the breakthrough curve of the CMC solutions, to later compare it with the breakthrough curve of the NANOfer STAR particles. This curve was calculated analyzing the electrical conductivity of the outflow samples and comparing the measurements with the reference value obtained from the bottle at the inflow.

4.2.12. NANOFE STAR column tests

After having completed the other experiments, also considering the previous transport results achieved at VEGAS, the suspension formed by 10 g/L NANOFE STAR in 10 g/L CMC was chosen for the column tests, for both sets of columns (C1.n and C2.n). Before the injection of particles, the tests started injecting degassed water at first, and CMC 10 g/L later. The purpose was to minimize the impact of an abrupt variation of experimental conditions in order to study the behavior of the particles without any disturbance. The setup for NANOFE STAR column tests, similar to the one used for CMC column tests, is schematized in Figure 59.

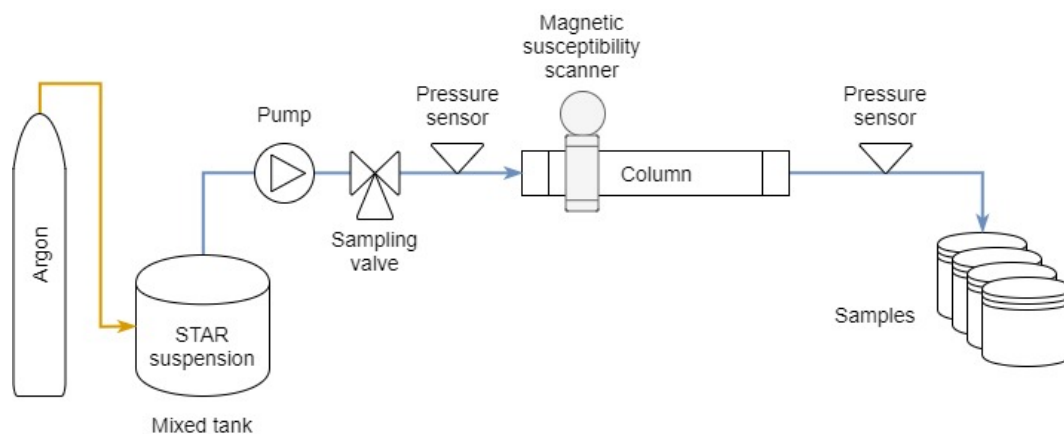


Figure 59 Scheme of experimental setup for NANOFE STAR column tests

As shown by the previous diagram, there are some differences between this setup and the one described by the flow chart in Figure 57. First, the tank containing the iron suspension is kept agitated at all times, to prevent an untimely sedimentation of the particles. The agitation is provided by the Turrax already showed in Figure 33. Also, the headspace of the tank is continuously flushed with argon, to hinder the contact between the suspension and the air oxygen. Then, a three-way valve has been inserted before the pressure sensor, to allow the sampling of the suspension entering the column. Lastly, a magnetic susceptibility sensor was placed around the column; during the injections the sensor scanned the whole column to determine the zerovalent iron present inside.

The pump and the pressure sensors are the same already described for the CMC column tests.

While the flushing with argon is a very simple process, the column scanning with the magnetic susceptibility sensor requires some considerations. As already mentioned, the sensor ran along the column during the experiments and it could track the iron concentration profile inside the column by induced voltage. It recorded a signal that required a complex decorrelation process, performed through a software designed at VEGAS by Dr.-Ing. Norbert Klaas.

Some pictures of the magnetic susceptibility scanner are reported in Figure 60.

Finally, the liquid samples collected at the outflow of columns during the tests were analyzed with the hydrogen evolution method (see 4.2.5) for the presence of ZVI; furthermore, at the end of each test, the columns were emptied and some soil samples were collected to be analyzed and a mass balance was calculated.

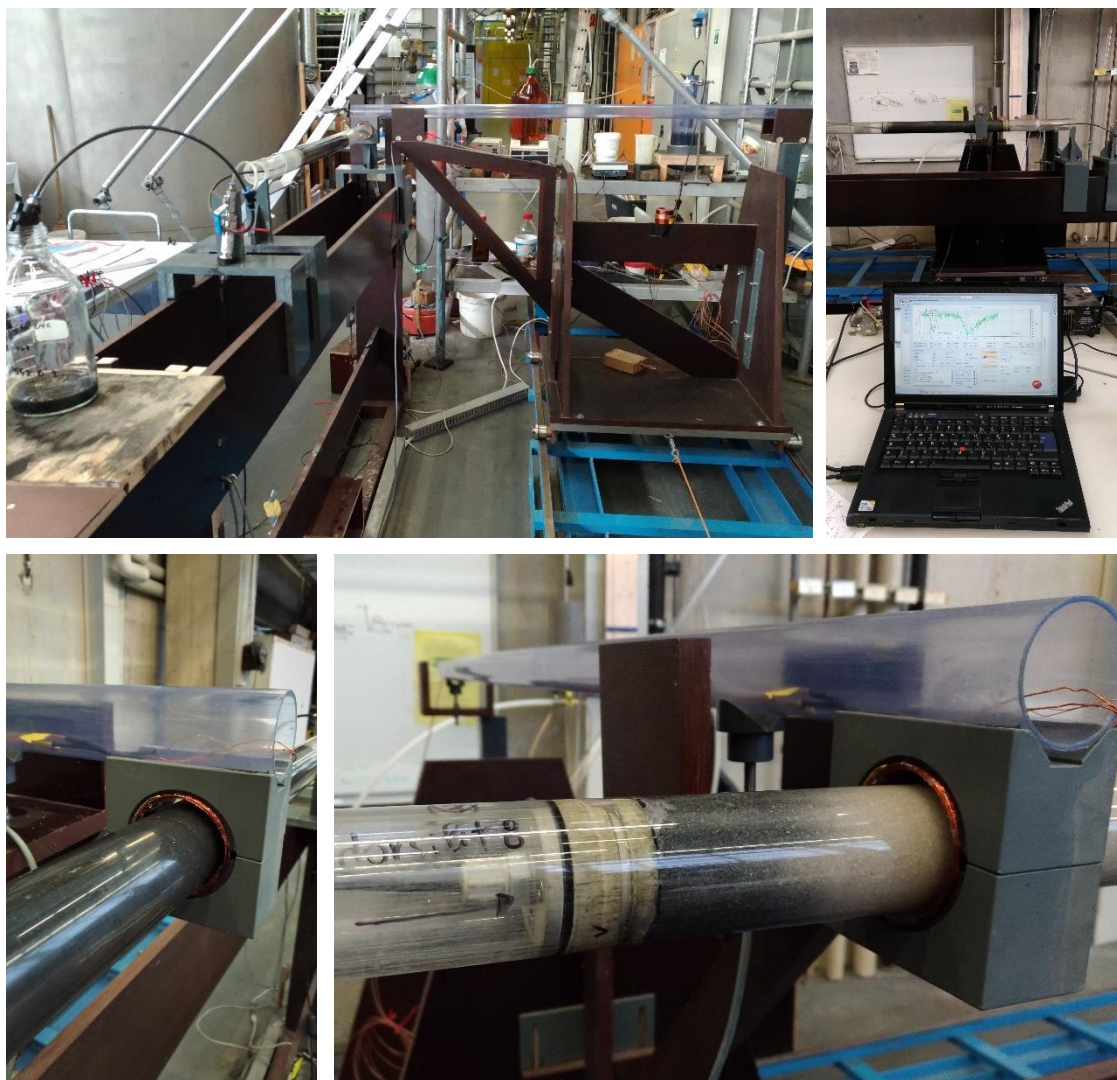


Figure 60 Pictures of the magnetic susceptibility scanner: the signal registered within the copper coil can be correlated to a concentration of zerovalent iron present in the column

In conclusion, the main results of the tests described in this section will be presented and discussed in section 5.4.

4.3. The software MNMs

One of the objectives of the present thesis was to model the NANOfer STAR injections with a software developed at Politecnico di Torino by C. Bianco, T. Tosco and R. Sethi. The software is called *Micro- and Nanoparticles transport, filtration and clogging Model – Suite*, abbreviated *MNMs*. Aside from the transport modeling, MNMs has many other features; in the following sections the main aspects will be presented.

4.3.1. DLVO interaction energy profiles

The software allows the calculation of the energy profiles described in section 3.3.3, both for particle–particle and particle–collector interactions. In particular, not only it calculates the classic DLVO interaction mechanisms, but also includes equations to evaluate the forces considered in the extended DLVO theory: steric, magnetic and born interactions; the complete formulations implemented in the software are available in the user manual (Bianco, Tosco, & Sethi, 2018). The tool for the evaluation of energy profiles, with default parameter, is shown below:

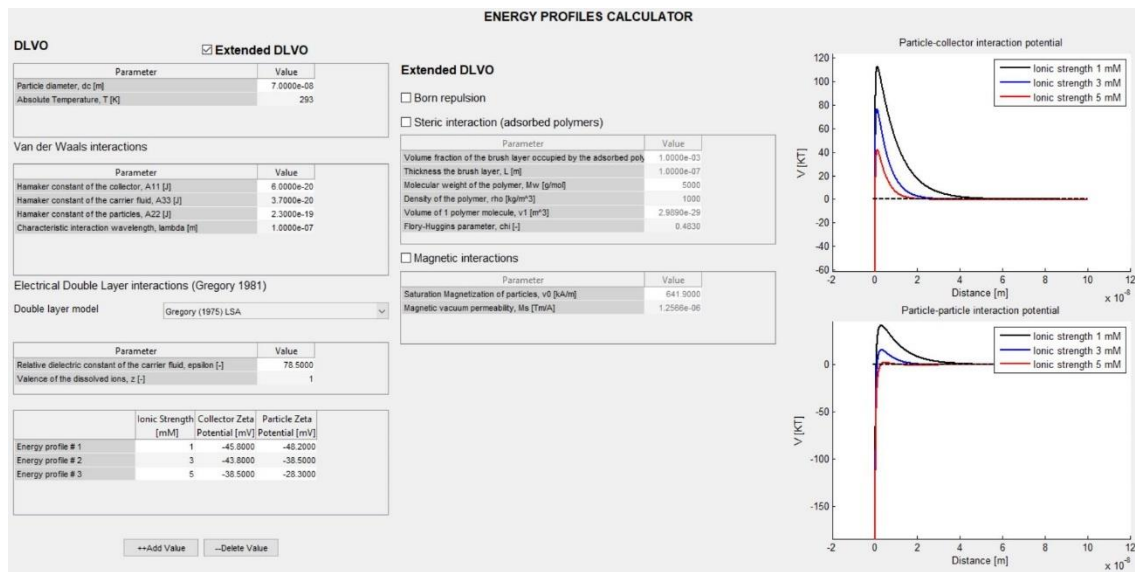


Figure 61 Tool for the calculation of energy profiles using DLVO or extended-DLVO interactions (MNMs©, 2018)

4.3.2. Single-collector contact efficiency

MNMs contains a tool for the evaluation of the single-collector contact efficiency (see 3.3.2), according to different formulations. The easiest is probably the one suggested by Yao et al. (Yao, Habibian, & O'Melia, 1971); it will be the one used in this thesis. The complete formulation of Yao's normalized single-collector contact efficiency implemented in the software is described by Eq. 27.

$$\eta_0 = 4.04A_S^{1/3}N_{Pe}^{-2/3} + \frac{3}{2}A_SN_R^2 + N_G \quad \text{Eq. 27}$$

Where:

- η_0 is the single-collector contact efficiency;
- A_S is a porosity dependent variable;
- N_{Pe} is the Peclet Number (*ratio between convective and diffusive transport*);
- N_R is the Steric number or Aspect ratio;
- N_G is the Gravity number (*ratio of Stokes particle settling velocity to approach velocity of the fluid*).

NB: A complete description of the previous dimensionless group is available in the user manual of MNMs (Bianco, Tosco, & Sethi, 2018).

The tool for evaluation of single-collector contact efficiency is shown below with default input parameters.

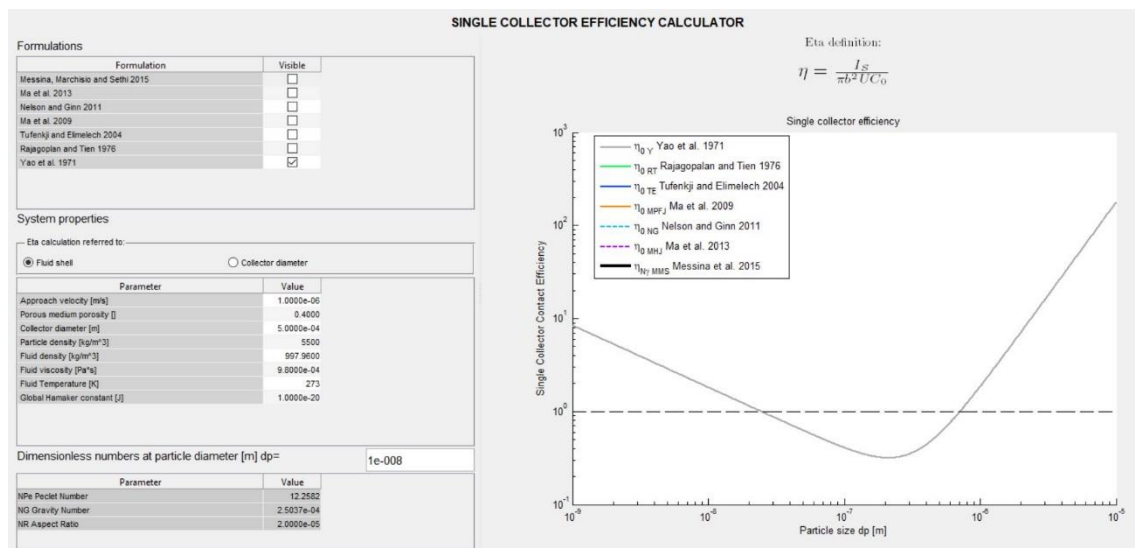


Figure 62 Tool for the calculation of single-collector contact efficiency (Yao's formulation) (MNM©, 2018)

4.3.3. Modeling the transport with MNMs

The main feature of MNMs is the tool for the simulation of solute and particle transport. Solute transport modeling may be used for the simulation, evaluation and/or validation of tracer tests, usually performed to obtain important parameters of porous media. Moreover, particle transport in a 1D situation can be simulated and/or evaluated; it means that the software can be used for the interpretation of column tests, with the aim of acquiring the parameters which regulate particle behavior in the porous medium. Lastly, MNMs allows the simulation of a field injection, supposing radial symmetry around the injection well.

These three options provided in the software are briefly described below.

4.3.3.1. Solute transport

The partial differential equation that describes the one-dimensional motion of a solute in a porous medium, accounting for a first-order degradation kinetics and *equilibrium adsorption*¹², can be expressed as indicated below:

$$\varepsilon R \frac{\partial C}{\partial t} = -q \frac{\partial C}{\partial x} + \varepsilon D \frac{\partial^2 C}{\partial x^2} - \varepsilon \lambda C \quad \text{Eq. 28}$$

where:

- ε [–] is the porous medium effective porosity;
- R [–] is the *retardation factor*:

$$R = 1 + \frac{\rho_b K_d}{\varepsilon} \quad \text{Eq. 29}$$

in which: ρ_b [$M L^{-3}$] bulk density of the solid matrix;
 K_d [$L^3 M^{-1}$] soil-water partition coefficient.

- q [$L T^{-1}$] is the Darcy's velocity (or specific discharge);
- C [$M L^{-3}$] is the concentration of the solute;
- D [$L^2 T^{-1}$] is the *dispersion coefficient*:

$$D = \alpha \cdot v \quad \text{Eq. 30}$$

in which: α [L] porous medium dispersivity;
 v [$L T^{-1}$] pore (or *effective*) velocity of the liquid phase.

- λ [T^{-1}] is the first-order degradation constant.

Both numerical and analytical solutions are provided by MNMs, in the hypotheses of homogeneous porous medium (constant porosity, bulk density, dispersivity) and of constant hydro-chemical parameters (flow velocity, soil-water partition coefficient, degradation rate) (Bianco, Tosco, & Sethi, 2018).

¹² The substances flowing in the groundwater may interact with the solid matrix, undergoing adsorption on the sand grains. *Equilibrium adsorption* is the condition for which the concentration of the solute in the liquid phase is at any time in equilibrium with the one adsorbed on the solid matrix (Di Molfetta & Sethi, 2012).

NB: In the equations on this page the adsorption kinetics is supposed linear.

4.3.3.2. Nanoparticle transport in 1D geometry

Transport and interaction mechanisms

MNMs implements most of the equations described in Section 3.3.5, above all Eq. 16, which describes the transport of nanoparticles in saturated porous media and is characterized by different interactions mechanisms. In particular, in the software, the interactions between particles and solid matrix can be simulated with up to two deposition mechanisms, choosing among CFT, linear, blocking, ripening and straining. The permitted combinations are represented in green in the following table.

Table 6 Allowed combinations of different interaction sites in MNMs. Adapted from (Bianco, Tosco, & Sethi, 2018)

		SITE 1			
		Linear	Blocking	Ripening	Straining
SITE 2	Linear	✓	✓	✓	✓
	Straining	✓	✓	✓	X

Ionic strength

The software can also consider the presence of a transient ionic strength, that modifies the attachment/detachment mechanisms. MNMs implements the semi-empirical approach proposed by Tosco et al. (Tosco, Tiraferri, & Sethi, 2009), which considers the coefficients k_a , k_d and S_{max} as functions of the salt concentration; the determination of several other empirical parameters is required in this formulation. Moreover, to link these relationships to the overall system of equations, a new equation describing the variations in time and in space of the water salinity needs to be added (Tosco & Sethi, 2009) (Tosco, Tiraferri, & Sethi, 2009). This equation can be written in the same way as Eq. 28, in which the solute is considered conservative ($\lambda = 0$) and not undergoing retardation ($R = 1$) (Bianco, Tosco, & Sethi, 2018).

Porous medium clogging

The clogging of the porous medium can also be accounted for by MNMs. The evaluation of clogging represents a crucial point of the model because it adds a degree of complexity.

First of all, in case of clogging, the porosity of the medium decreases proportionally to the number of attached particles (Bianco, Tosco, & Sethi, 2018):

$$\varepsilon_m = \varepsilon_0 - \frac{\rho_b}{\omega \rho_c} S \quad \text{Eq. 31}$$

where:

- ε_m [–] is the porosity available to the mobile phase;
- ε_0 [–] is the initial porosity (clean-bed condition);
- ρ_b [$M L^{-3}$] is the bulk density;
- ω [–] is an empirical coefficient that represents the fraction of deposited particles that contributes to the decrease of porosity;
- ρ_c [$M L^{-3}$] is the density of colloidal particles;
- S [–] is the particle concentration in the solid phase.

Besides, also the specific surface area of the solid matrix depends on the deposition process; a formulation is given below (Bianco, Tosco, & Sethi, 2018):

$$A = A_0 + \theta A_c \frac{\rho_b}{\rho_c} S \quad \text{Eq. 32}$$

where:

- $A [L^{-1}]$ is the specific surface area available;
- $A_0 [L^{-1}]$ is the initial specific surface area (clean-bed condition);
- $\theta [-]$ is an empirical coefficient that represents the fraction of the surface of deposited particles that contributes to the increase of specific area;
- $\rho_b [M L^{-3}]$ is the bulk density;
- $\rho_c [M L^{-3}]$ is the density of colloidal particles;
- $S [-]$ is the particle concentration in the solid phase.

Then, the two previous equations (Eq. 31 and Eq. 32) can be used in the *Kozeny-Carman equation*¹³ to describe the variation of permeability of the solid matrix (Bianco, Tosco, & Sethi, 2018):

$$k = \left(\frac{\varepsilon_m}{\varepsilon_0} \right)^3 \left(\frac{A_0}{A} \right)^2 k_0 \quad \text{Eq. 33}$$

where $k [L^2]$ is the current permeability, $k_0 [L^2]$ is the starting one.

Finally, it is possible to calculate the pressures buildup through a modified formulation of the Darcy's law (Bianco, Tosco, & Sethi, 2018):

$$-\nabla p = \frac{\mu_m}{k(S)} q \quad \text{Eq. 34}$$

where:

- $\nabla p [M L^{-1} T^{-2}]$ is the pressure gradient;
- $\mu_m [M L^{-1} T^{-1}]$ is the viscosity of the liquid fluid;
- $k(S) [L^2]$ is the porous medium permeability, dependent on the particle concentration deposited in the matrix;
- $q [L T^{-1}]$ is the Darcy's velocity (or specific discharge).

The complexity in the description of porous medium clogging lies in the interconnections among the abovementioned parameters: a variation in one of these parameters determine a change in the other. In addition, they are all linked to the advection-dispersion equation that regulates the transport. For this reason, MNMs offers two ways of evaluating the nanoparticle transport accounting for porous medium clogging (Bianco, Tosco, & Sethi, 2018):

¹³ "The Carman-Kozeny equation (or the *Kozeny-Carman equation*) is a relation to calculate the pressure drop for laminar flow through a packed bed of solids. It was originally developed by Kozeny in 1927 [...]" (Kruczek, 2014).

- Coupled flow and transport option, where porosity and permeability are supposed to have an important influence on transport equations: at every time step of the numerical solution their influences are accounted for in the transport model;
- Decoupled flow and transport option, where the transport equations are solved, at every time step, prior to porosity and permeability variations. This simulation is faster, but it can be performed only when the variations of the porous medium properties are expected to be small.

Mobile phase viscosity

When simulating the transport of a polymer-stabilized suspension, in order to consider the dependence of the dynamic viscosity from shear rate, MNMs implements a modified *Cross model* (Gastone, Tosco, & Sethi, 2014a), reported below:

$$\mu_m = \mu_\infty + \frac{\mu_0 - \mu_\infty}{1 + (\vartheta \dot{\gamma})^\chi} \quad \text{Eq. 35}$$

where:

- $\mu_m [M L^{-1} T^{-1}]$ is the viscosity of the liquid fluid;
- $\mu_0 [M L^{-1} T^{-1}]$ is the viscosity of the liquid fluid at zero shear rate;
- $\mu_\infty [M L^{-1} T^{-1}]$ is the viscosity of the liquid fluid at extremely high shear rates;
- $\dot{\gamma}_m [T^{-1}]$ is the shear rate experienced by the mobile phase;
- $\vartheta [T^{-1}]$ and $\chi [-]$ are parameters of the Cross model.

In this model the dynamic viscosity is a function of both the shear rate in porous medium and the concentration of polymer. A simple representation of the Cross model is given in Figure 63.

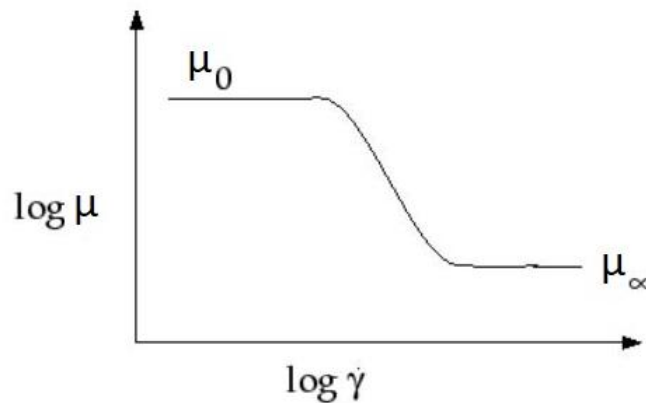


Figure 63 Representation of Cross model for shear-thinning fluids. Adapted from (ANSYS Fluent)

The complete description of the model is provided in MNMs user manual (Bianco, Tosco, & Sethi, 2018); however, it is worth mentioning that an estimation of the shear rates experienced by a fluid moving in a porous medium is given by Bird (2002) and Lopez et al. (Lopez, Valvatne, & Blunt, 2003); the formulation is presented below.

$$\dot{\gamma}_m = \alpha \frac{|q|}{\sqrt{|k|\varepsilon}} \quad \text{Eq. 36}$$

where:

- $\dot{\gamma}_m [T^{-1}]$ is the shear rate experienced by the mobile phase;
- α is a *shift factor*, used to match rheograms from rotational tests;
- $q [L T^{-1}]$ is the Darcy's velocity (or specific discharge);
- $k [L^2]$ is the intrinsic permeability of the porous medium;
- $\varepsilon [-]$ is the effective porosity of the porous medium.

4.3.3.3. Nanoparticle transport in radial geometry

MNMs allows the simulation of a nanoparticle injection in a radial domain through Eq. 20, which describes the particle transport in the porous medium. Also in this case, MNMs consents the choice of up to two interaction mechanisms, selecting between linear and generic ripening; the ripening mechanism, however, can be transformed into blocking with a specific choice of the input parameters.

Here again, MNMs can account for the influence of the mobile phase viscosity and for the clogging of the porous medium in similar fashions respect to what presented in the previous section. The main differences are the radial space domain, with the consequent change in flow velocity, and the possibility to evaluate the contribution of undissolved polymer residuals to clogging.

Moreover, as already mentioned in section 3.3.5, the attachment and detachment coefficients are strongly influenced by the flow velocity, which now is decreasing hyperbolically; their evaluation is carried out by the software through Eq. 22 and Eq. 23.

5. Results and discussion

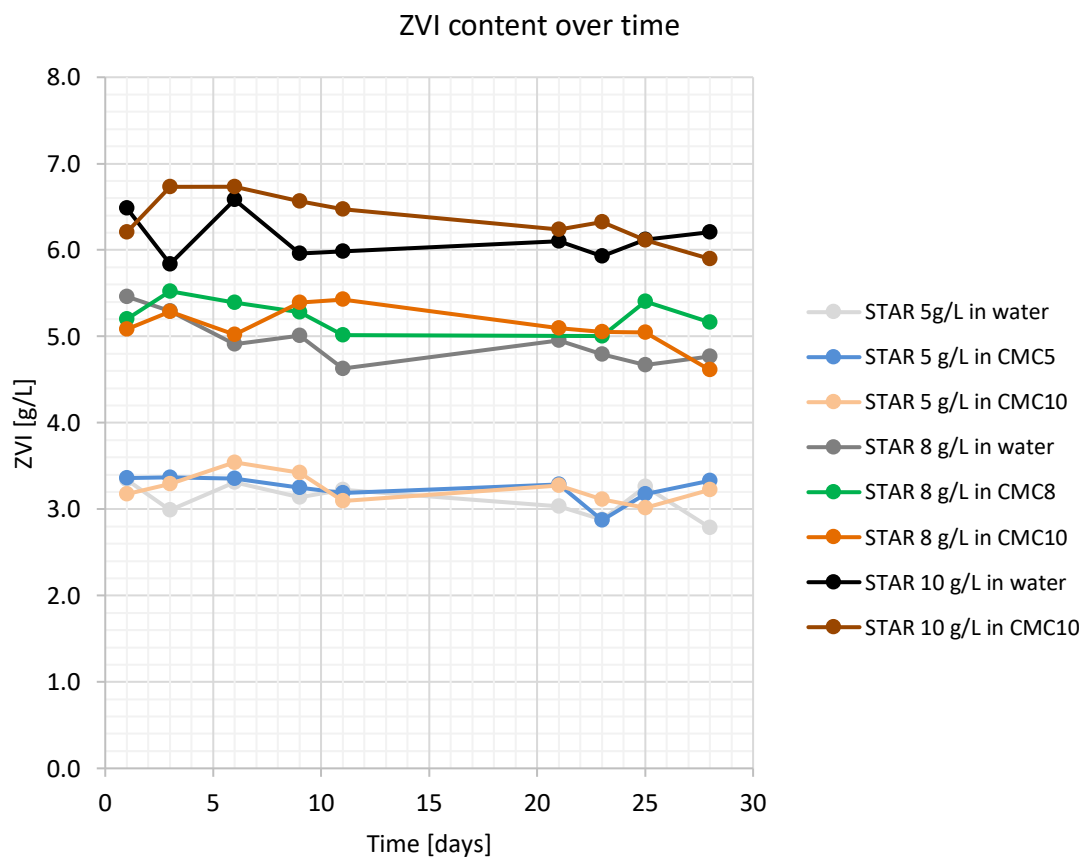
5.1. Particle and suspension characterization

In the present section the main results concerning the characterization of NANOFE STAR particles and suspensions will be provided. In between the results, some comments will be made.

5.1.1. ZVI content in NANOFE STAR suspensions

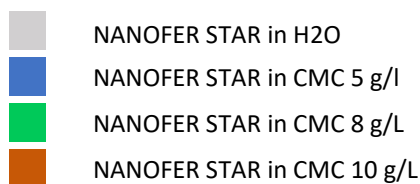
As explained in section 4.1.3, NANOFE STAR particles are composed of zerovalent iron for ca. the 77%; for this reason, it is always important to remember that a suspension 10 g/L of NANOFE STAR, for instance, does not correspond to a suspension 10 g/L of ZVI. The preparation of the suspensions was based on the mass of NANOFE STAR particles, while the content of iron in the samples has always been evaluated using the hydrogen evolution method (ref. 4.2.5), which reveals on the ZVI content.

That being said, some analyses on the ZVI content in the suspensions have been conducted at VEGAS. Specifically, the content of ZVI in the suspensions has been measured over a month to see if an ageing process took place, and the zerovalent iron was oxidized into another form. The results are presented below.



Graph 1 Content of zerovalent iron in different NANOFE STAR suspensions; values over time

To identify more easily the suspensions having the same CMC concentration, the previous graph was based on the following color sets:

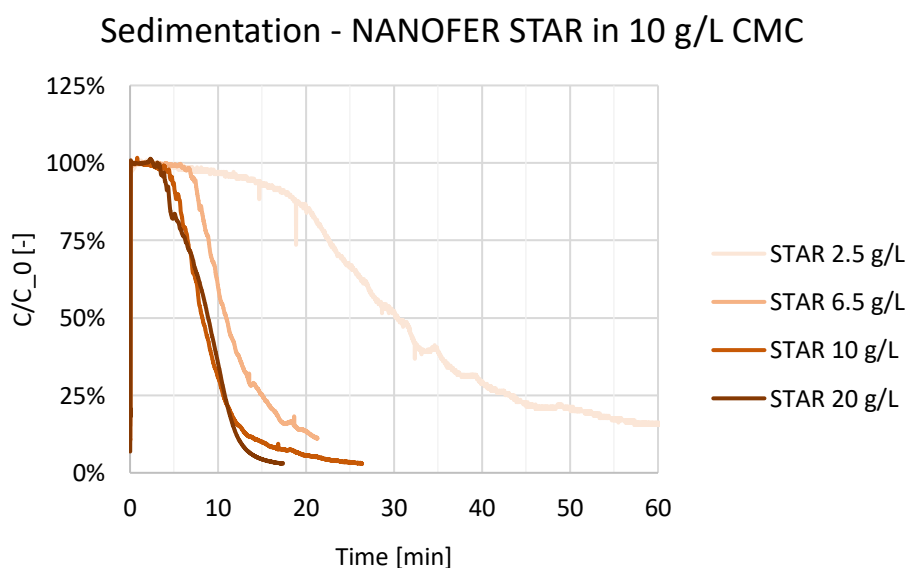


The first consideration on Graph 1 is that the ZVI content is actually lower than expected: the suspensions prepared with 10 g/L of NANOFER STAR particles only have about 6.2 g/L of ZVI, those prepared with 8 g/L, only have about 5 g/L of ZVI, and so on. It means that, once dispersed, the ZVI fraction is only the 62% of the total. Part of the zerovalent iron is probably oxidized during the preparation of the suspensions.

Another possible remark is that for a month the content of ZVI did not change considerably; there is a slight decreasing trend for most of the curves, but in all cases it is very slight. It is important to say that the samples were stored at room temperature (between 15 and 20 °C) in sealed, glass bottles, and only opened for the measurements.

5.1.2. Sedimentation tests

To evaluate the stability of the NANOFER STAR suspensions, some sedimentation tests have been performed at Politecnico di Torino, using a magnetic susceptibility meter (see 4.2.6). In this way it was possible to determine how long it took for the suspensions to sediment. This test was carried out with four different concentrations of particles dispersed in 10 g/L CMC; the suspensions, after their preparation, were left to cool down until room temperature prior to the measurements: during the mixing phase with the disperser extremely high temperatures were reached, causing a decisive reduction in the suspension viscosity. The relative concentration of particles, normalized on the maximum value, is represented below.



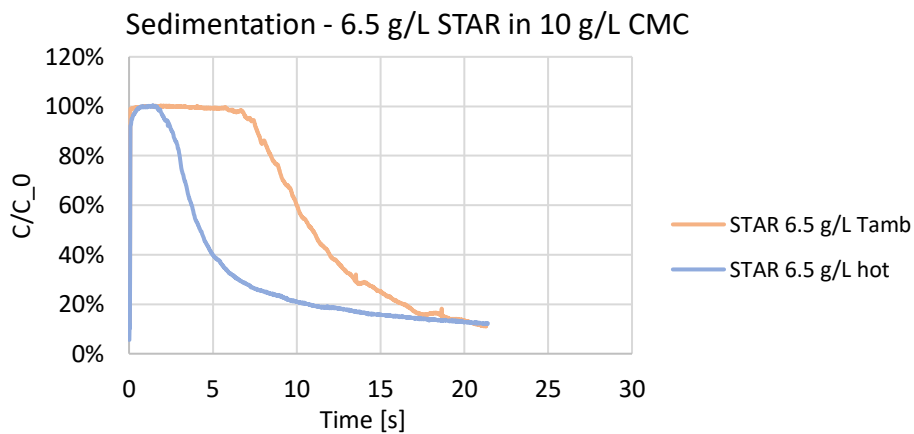
Graph 2 Sedimentation tests for different NANOFER STAR suspensions in 10 g/L CMC

Graph 2 shows the decrease in the concentrations due to the settling of particles. In particular, it is possible to observe that at higher concentrations, NANOFE STAR particles settle more rapidly; an explanation of this phenomenon can be found in the tendency to aggregation of the particles: higher concentrations cause the formation of bigger aggregates, which are more likely to sediment, according to Stokes' law. To quantify the previous fact, the sedimentation half time of the particle concentrations has been extracted from Graph 2 and listed in Table 7.

Table 7 Having of NANOFE STAR concentrations due to settling

NANOFE STAR conc. [g/L]	$T_{1/2}$ [min.]
2.5	30.4
6.5	10.9
10	8.2
20	8.9

To visualize the effect of temperature in the previous experiments, the sedimentation tests of the suspension 6.5 g/L are displayed in Graph 3, comparing the results obtained at room temperature with the ones in which the suspension was still hot after its preparation.



Graph 3 Comparison between the sedimentation of two suspensions at different temperatures

5.1.3. BET tests

Some brief experiments for the determination of specific surface area of NANOFE STAR particles have been performed at VEGAS. The procedure and the instruments used for this analysis are presented in section 4.2.7. The results of this test, performed on three samples with different NANOFE STAR and CMC concentrations, are provided in Table 8.

Table 8 Samples for BET analysis

Date	Sample (STAR conc. / polymer conc.)	m_{sample} [g]	total surface area [m ²]	BET specific surface area [m ² /g]
19/09/2017	10/10	0.523	13.68	26.15
21/09/2017	8/8	0.8752	26.69	30.49
25/09/2017	5/5	1.0254	23.50	22.96

The results are similar to those reported by the producer: specific surface area $> 25 \text{ m}^2/\text{g}$, (NANO IRON s.r.o. - NANO FER STAR manual). A higher concentration of CMC in the suspensions may result in a higher specific surface area because it prevents the particles from creating agglomerates. This hypothesis however must be validated with further investigations.

5.1.4. Particle size distribution

The evaluation of the particle size distribution (PSD) of NANO FER STAR suspensions has been performed at VEGAS with the acoustic-electroacoustic spectrometer; later, at Politecnico of Torino, the results were validated through a disc centrifuge (see 4.2.8).

At VEGAS, four series of samples have been prepared for the analyses with the spectrometer. In particular, each series of suspensions was prepared with a different CMC concentration; then, for each series, different concentrations of NANO FER STAR particles were used. The samples prepared are summarized in Table 9. The choice of particle and polymer concentrations was based on previous tests and had the objective of identifying the best combination in terms of small suspended particles and colloidal stability; moreover, during the choice, it was always kept in mind that these concentration ranges may actually refer to field applications.

Table 9 Samples measured with the acoustic-electroacoustic spectrometer

		NANO FER STAR concentration (g/L)							
		1	2.5	5	8	10	15	20	30
CMC concentration (g/L)	0 (water)								
	5								
	8								
	10								

Measurements below the accuracy threshold: very low reliability

Measurements close to the accuracy threshold: little reliability

Measurements above the accuracy threshold: good reliability

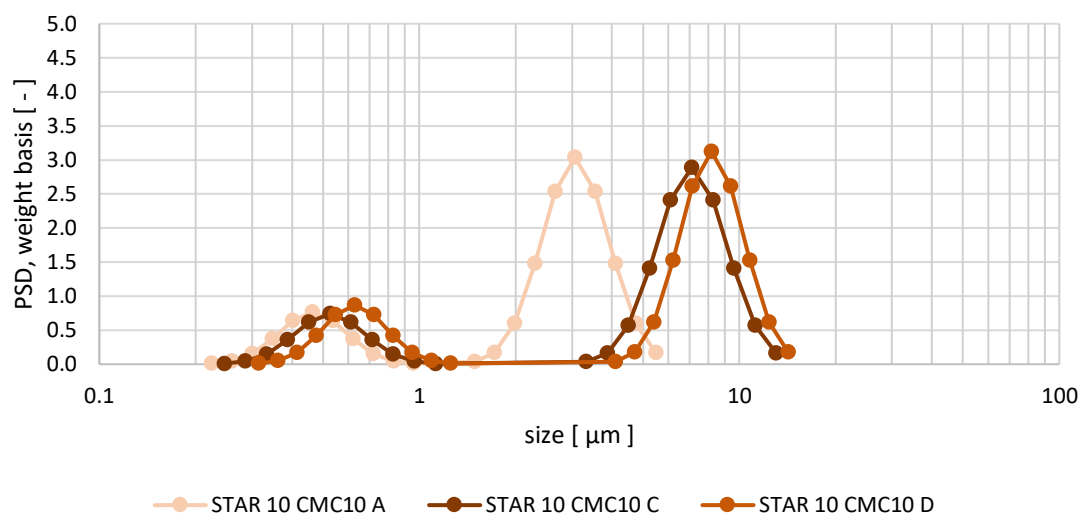
As expressed by the previous table, the concentrations chosen presented an inconvenient: the spectrometer, which work very well for concentrated suspensions, had some difficulties in detecting the iron particles in the more diluted suspensions. In effect, the producer suggested 10 g/L as the lower threshold of instrumental accuracy. For this reason, only certain results will be shown below, the ones for which the instrument provided a good fitting of the experimental data to the theoretical models (see 4.2.8.1 for the instrument working principle).

The most reliable results of PSD given by the spectrometer, divided by iron concentration, are reported in the next pages; to easily identify the different CMC concentration in each graph, the following color sets are given to each series:

	NANO FER STAR in H ₂ O
	NANO FER STAR in CMC 5 g/l
	NANO FER STAR in CMC 8 g/L
	NANO FER STAR in CMC 10 g/L

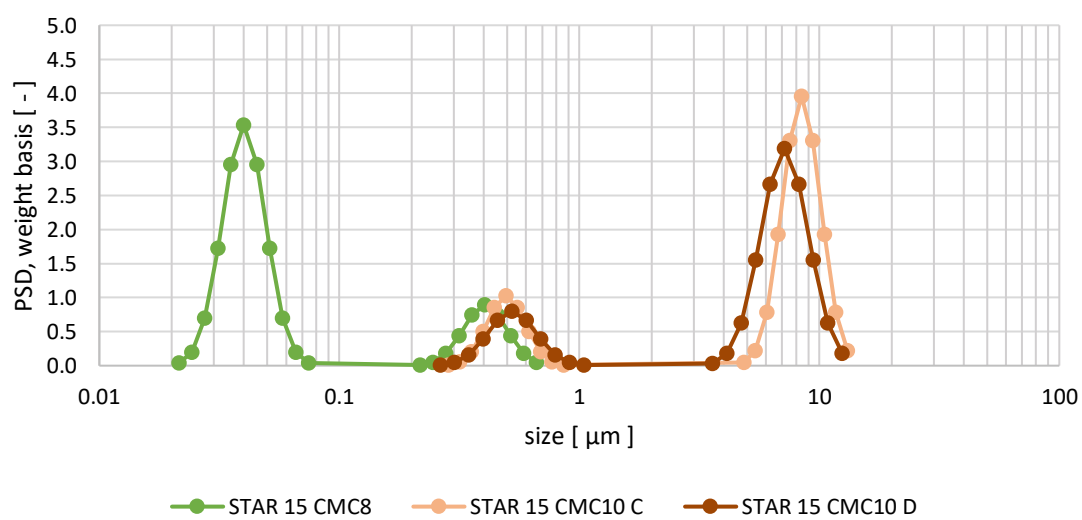
Moreover, the capital letters A, B, etc. design different replicates of the same sample.

Particle Size Distribution - STAR 10 g/L

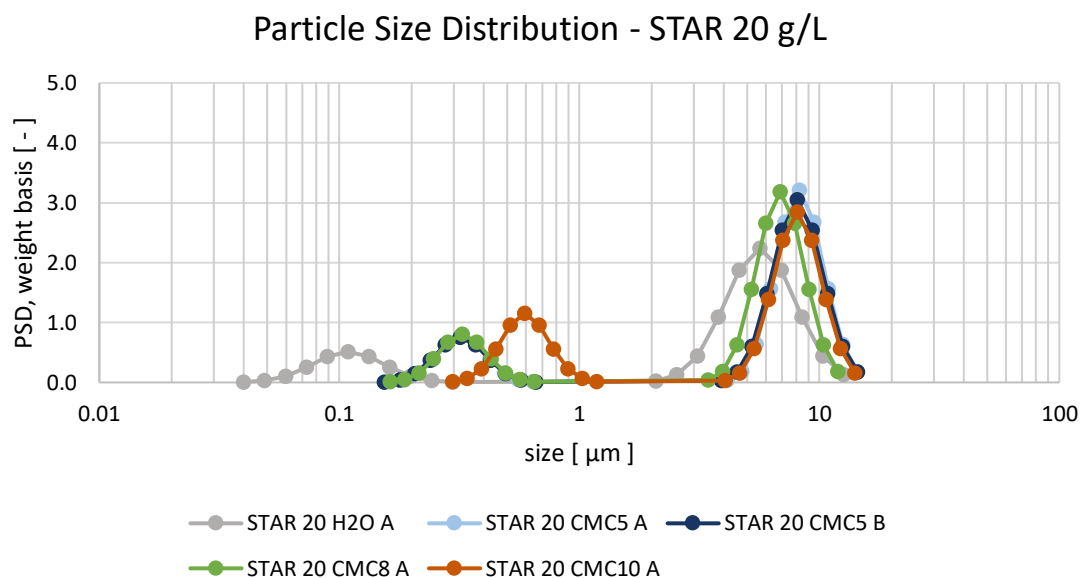


Graph 4 PSD of the reliable samples with 10 g/L of NANOFER STAR

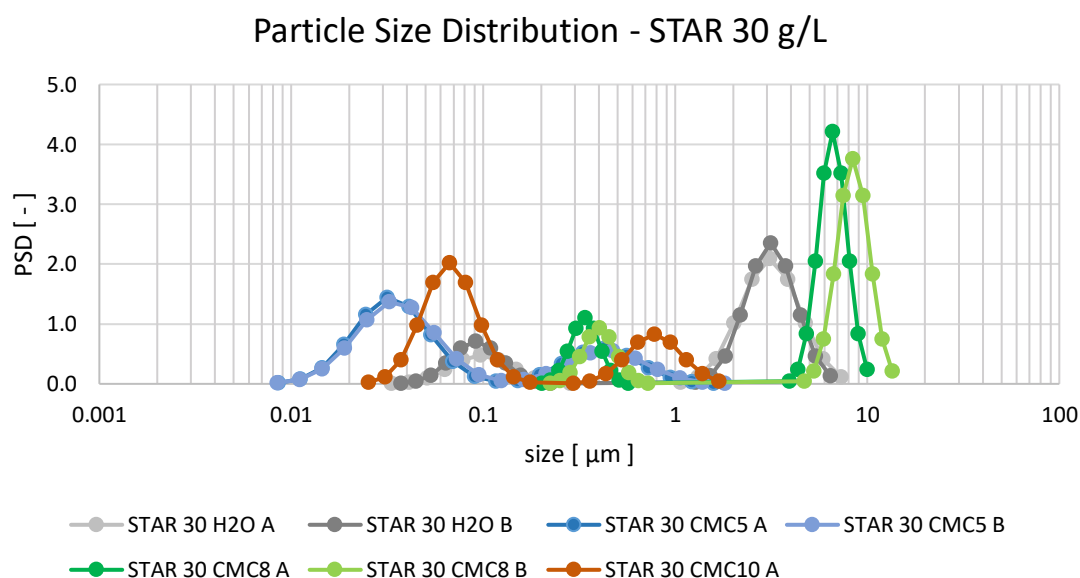
Particle Size Distribution - STAR 15 g/L



Graph 5 PSD of the reliable samples with 15 g/L of NANOFER STAR



Graph 6 PSD of the reliable samples with 20 g/L of NANO FER STAR

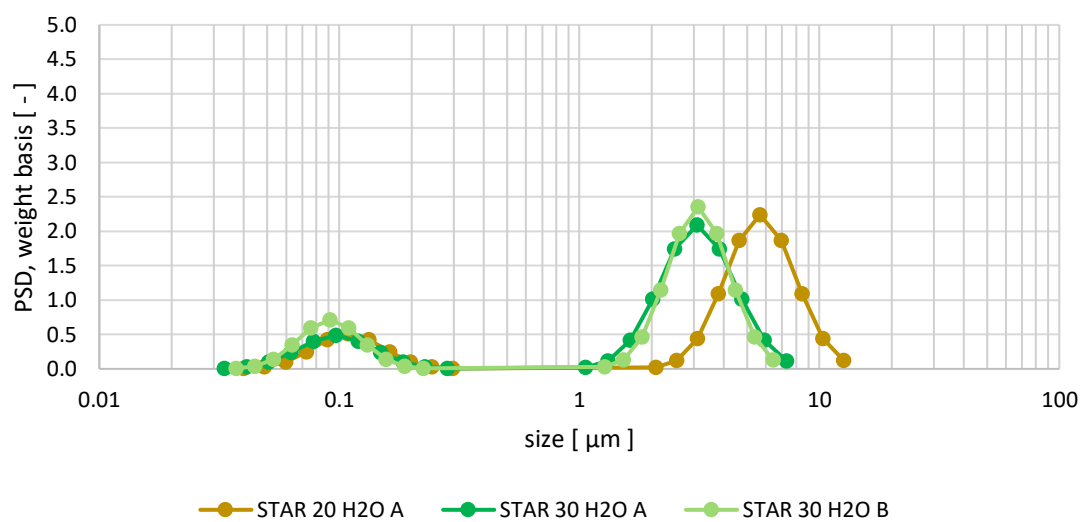


Graph 7 PSD of the reliable samples with 30 g/L of NANO FER STAR

Furthermore, to evaluate the presence of some trends, the same results can now be divided by CMC concentration. The data are presented in the following pages, trying to assign a color set to the different iron concentrations:

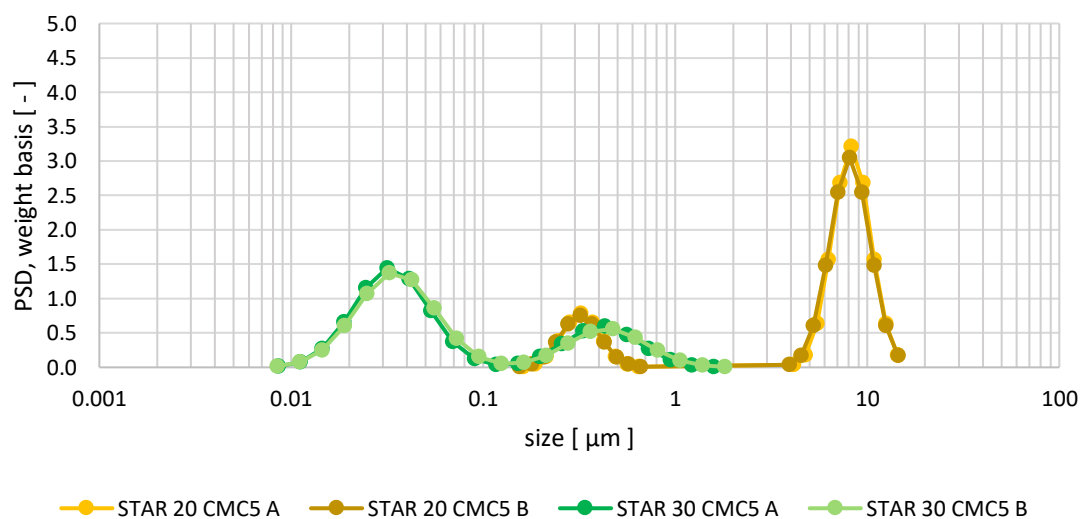


Particle Size Distribution - water

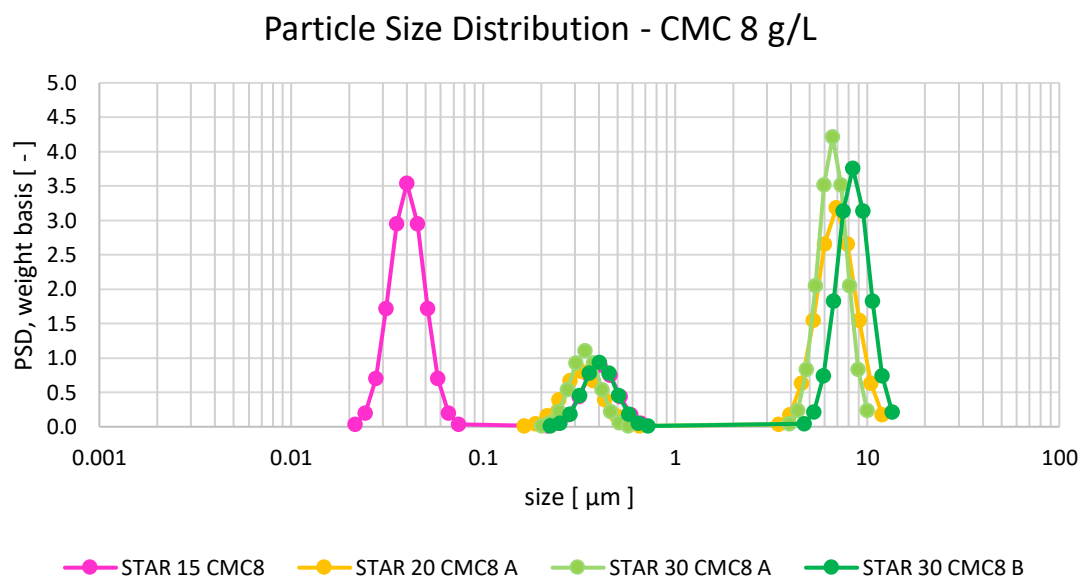


Graph 8 PSD of the reliable samples prepared in water

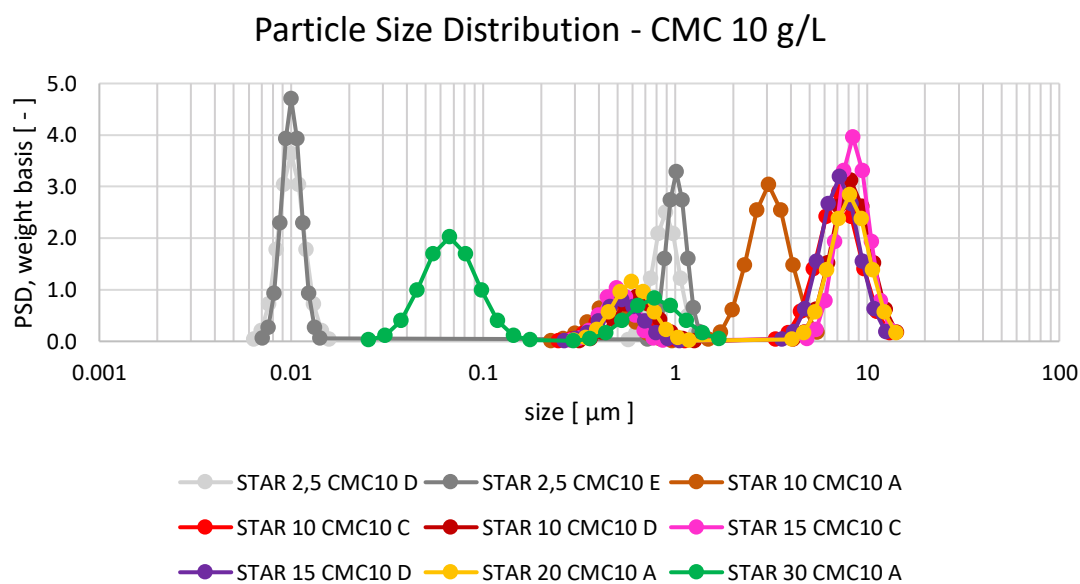
Particle Size Distribution - CMC 5 g/L



Graph 9 PSD of the reliable samples prepared in CMC 5 g/L



Graph 10 PSD of the reliable samples prepared in CMC 8 g/L



Graph 11 PSD of the reliable samples prepared in CMC 10 g/L

The analysis of the previous graphs is quite complex; in fact, it is hard to identify a clear trend in particle size depending on the concentration of iron or of CMC. Higher concentrations of CMC were expected to prevent the agglomeration of iron particles, hence ensuring a greater fraction of smaller particles; however, in the previous graphs, often the opposite situation is observed (e.g. in Graph 5 or Graph 6). An explanation can be the following: the spectrometer sees the particles surrounded by polymer, detecting a larger size.

Afterwards, higher iron concentrations were expected to create more easily aggregates, resulting in larger clusters. This situation may be revealed by Graph 10, but the exceptions are numerous (e.g. Graph 9).

To synthetize the previous data, the dimension corresponding to the peaks is reported in the following table:

Table 10 Dimensions corresponding to the peaks of concentration

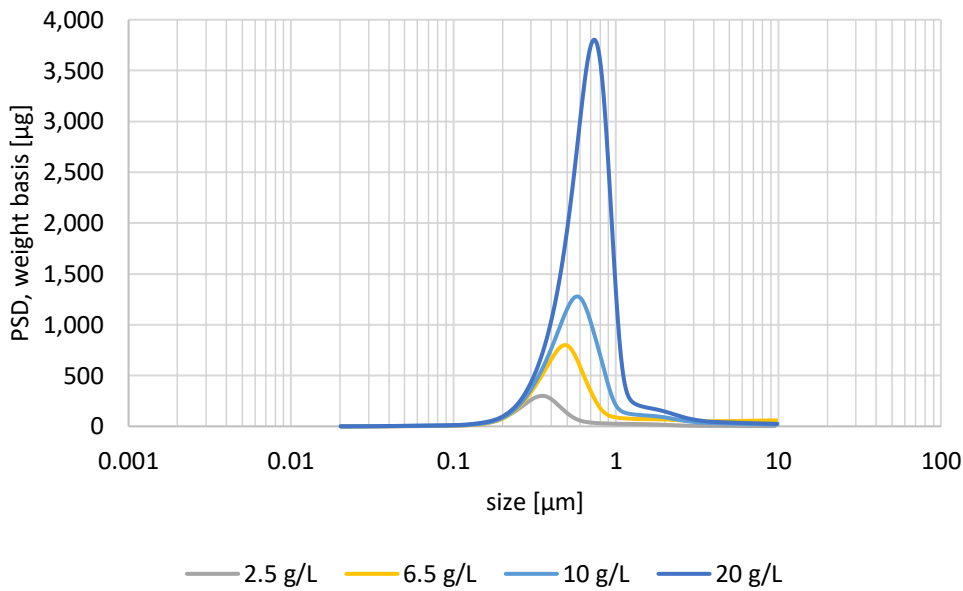
Sample	Replicate	Peak 1 [μm]	Peak 2 [μm]
STAR 2.5 g/L CMC 10 g/L	D	0.010	1.010
STAR 2.5 g/L CMC 10 g/L	E	0.010	0.944
STAR 10 g/L in CMC 10 g/L	A	0.464	3.069
STAR 10 g/L in CMC 10 g/L	C	0.525	7.100
STAR 10 g/L in CMC 10 g/L	D	0.628	8.181
STAR 15 g/L in CMC 8 g/L		0.040	0.443
STAR 15 g/L in CMC 10 g/L	C	0.495	8.420
STAR 15 g/L in CMC 10 g/L	D	0.525	7.170
STAR 20 g/L in H ₂ O	A	0.119	5.670
STAR 20 g/L in CMC 5 g/L	A	0.322	8.262
STAR 20 g/L in CMC 5 g/L	B	0.319	8.100
STAR 20 g/L in CMC 8 g/L	A	0.326	6.887
STAR 20 g/L in CMC 10 g/L	A	0.592	8.090
STAR 30 g/L in H ₂ O	A	0.097	3.100
STAR 30 g/L in H ₂ O	B	0.091	3.130
STAR 30 g/L in CMC 5 g/L	A	0.032	0.430
STAR 30 g/L in CMC 5 g/L	B	0.032	0.474
STAR 30 g/L in CMC 8 g/L	A	0.338	6.588
STAR 30 g/L in CMC 8 g/L	B	0.402	8.424
STAR 30 g/L in CMC 10 g/L	A	0.067	0.776

However, what can really be understood from the previous graphs and from Table 10, is the presence of three regions, characterized by different particle size. These regions are clearly observed in Graph 5, Graph 8, Graph 9 and Graph 10, but can also be recognized in other charts. The first two regions, ranging between $0.01 - 0.1 \mu\text{m}$ and $0.1 - 1 \mu\text{m}$ respectively, were expected: they represent the region of the single NANOFE STAR particles and that of larger aggregates. The region at higher dimensions ($1 - 10 \mu\text{m}$) instead, was unexpected; if it represented some large aggregates, it would mean that these particles are not suitable for traveling in the soil, because they would be way too large.

To verify the presence of particles with a particle size falling in the bigger region, further experiments have been carried out at Politecnico di Torino, using the disc centrifuge. In this occasion, only four samples were analyzed, focusing the attention on the most important combinations for the objectives of this thesis. For this reason, the measurements were performed on the particle concentrations 2.5, 6.5, 10 and 20 g/L in a 10 g/L solution of CMC.

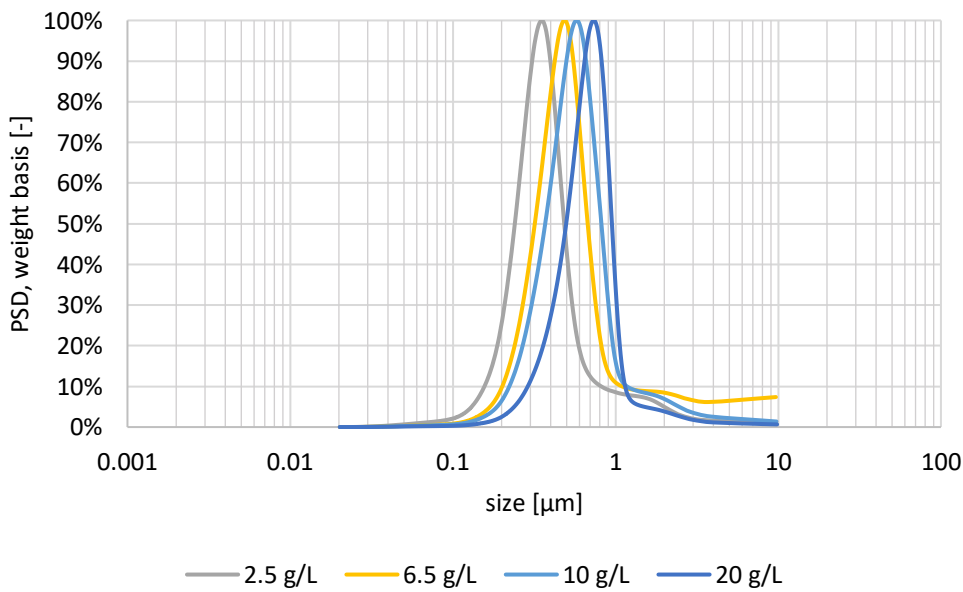
The centrifuge can provide PSD curves using both the weight and the number of particles of the sample as basis. The results are shown below, both raw and normalized on the maximum, to make them easier to compare among each other.

PSD NANOFER STAR in CMC 10 g/L - weight (raw)

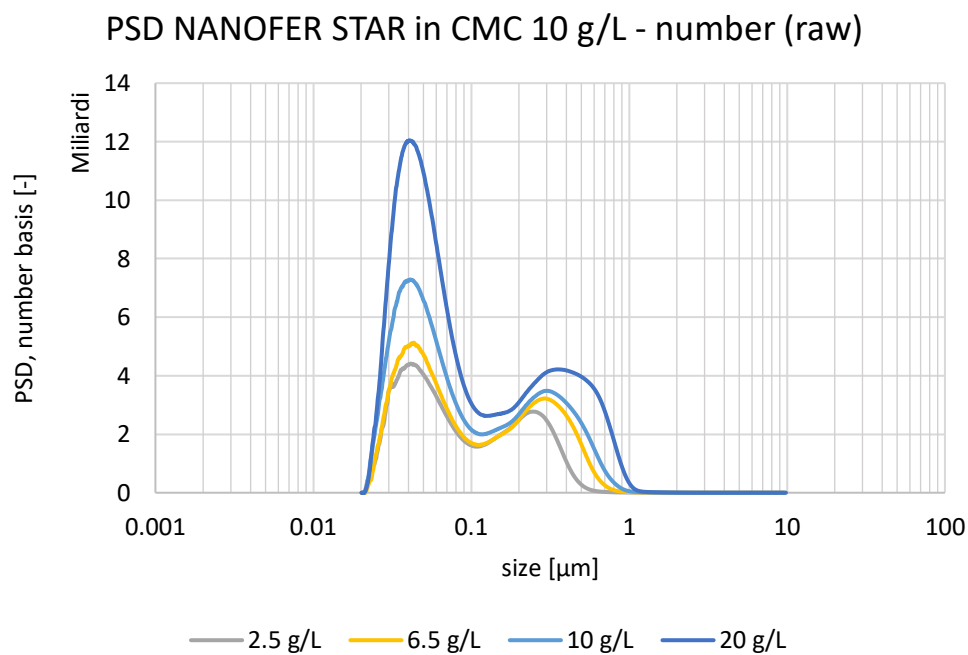


Graph 12 PSD obtained from the tests with the disc centrifuge: results by weight

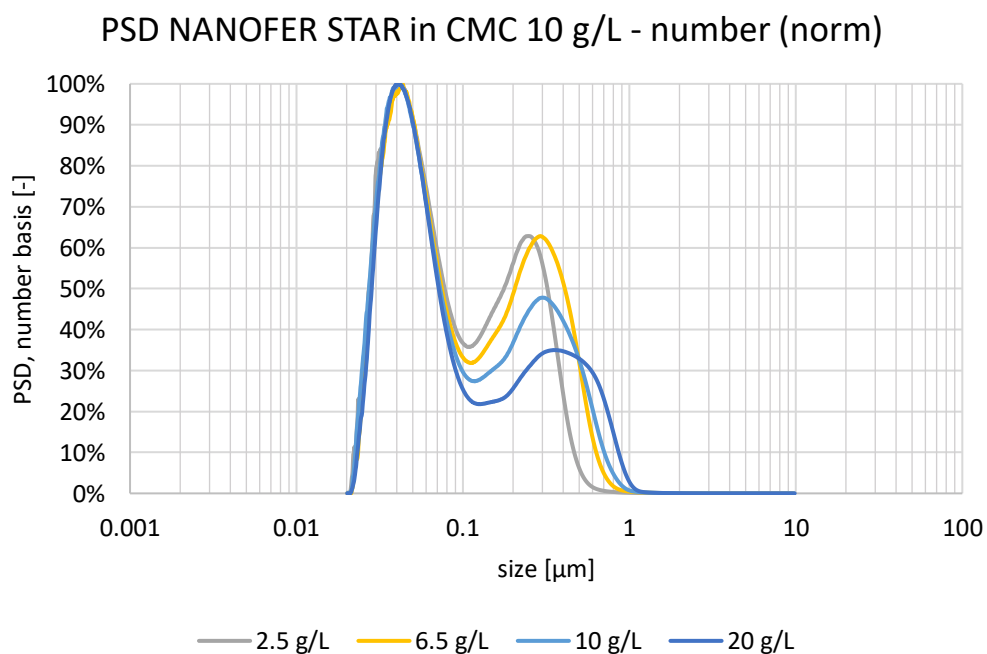
PSD NANOfer STAR in CMC 10 g/L - weight (norm)



Graph 13 PSD obtained from the tests with the disc centrifuge: results by weight, normalized on the maximum



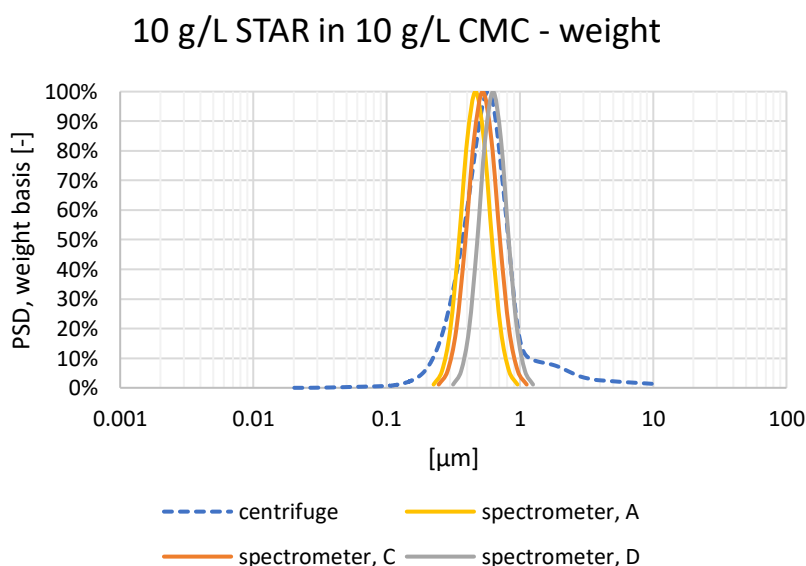
Graph 14 PSD obtained from the tests with the disc centrifuge: results by number



Graph 15 PSD obtained from the tests with the disc centrifuge: results by number, normalized on the maximum

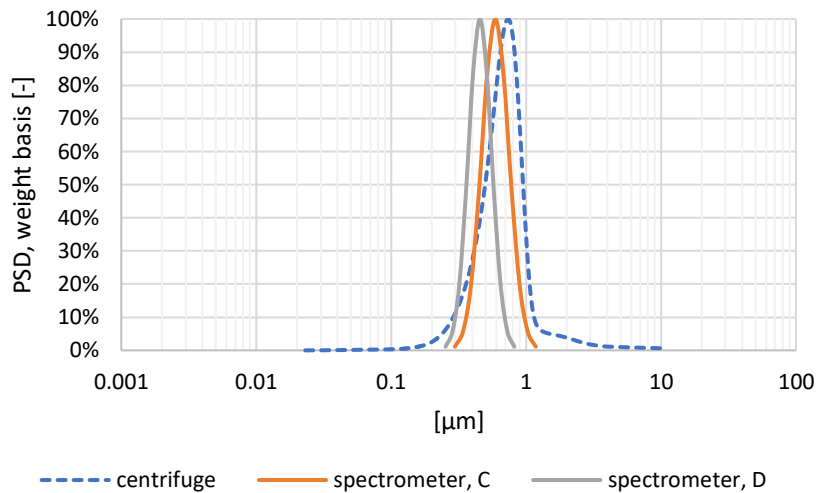
The graphs showing the PSD on weight basis (Graph 13 and Graph 14) display unimodal distributions, in a range of size that corresponds to the intermediate region detected by the spectrometer ($0.1 - 1 \mu m$). A smaller fraction of particles, positioned in the region $0.01 - 0.1 \mu m$ previously described, is visible in the PSD curves only when they are based on particle number (see Graph 14 and Graph 15). It means that, even if most of the iron particles have a tiny dimension, their presence is negligible in terms of mass.

However, in the previous graphs there is no trace of the larger fraction of particles (region $1 - 10 \mu m$) detected by the spectrometer. The best explanation for this fact is that the peak identified by the spectrometer is actually not composed of iron particles. Probably the process of preparation of the suspensions, realized through a long phase of mixing, caused the formation of air bubbles in the suspensions; the instrument then, measuring the attenuation of the sound signal, mistook the bubbles for larger agglomerates. This fact has already been observed in previous tests, and the size range of the microscopic bubbles was indeed between 1 and $10 \mu m$. This hypothesis is strengthened by the fact that the peaks in Graph 12 and Graph 13 seem to be consistent with the ones shown by the spectrometer. To verify this condition the results obtained with different instrument and analogous samples were combined, when possible. Specifically, this operation has been performed for 10 and 20 g/L NANOFE STAR suspensions in 10 g/L CMC. In order to show the two PSDs together, the values have been normalized; furthermore, the peak that seems to correspond to air bubble has been deleted. The outcome is presented below.



Graph 16 Comparison between spectrometer and disc centrifuge results; NANOFE STAR 10 g/L

20 g/L STAR in 10 g/L CMC - weight

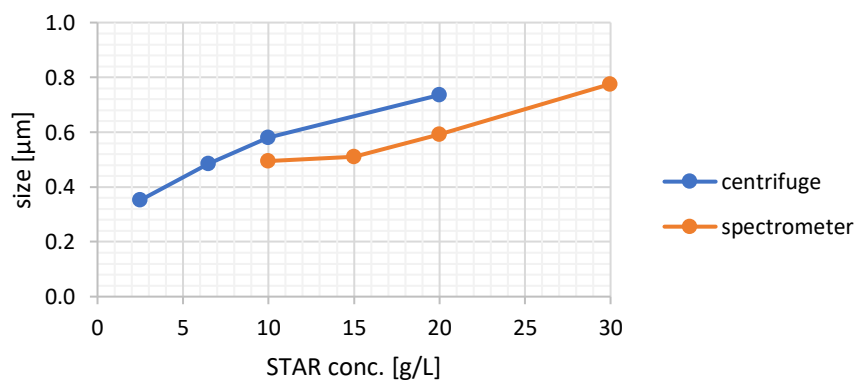


Graph 17 Comparison between spectrometer and disc centrifuge results; NANOFE STAR 20 g/L

As demonstrated from Graph 16 and Graph 17, when evaluating the weight-based PSDs on both instruments, the results obtained are coherent: the iron mass of the samples is constituted of particles with dimensions of $0.4 - 0.8 \mu m$, probably consisting on the aggregates formed by the NANOFE STAR particles. However, a finer fraction is detected by both instruments. The centrifuge reveals it only when measuring on a number basis, demonstrating its unimportance in terms of mass. The spectrometer sometimes detects this smaller fraction even on weight basis, but the interference with the air bubbles hindered a reliable measurement: it is recommended, when performing new evaluations with the acoustic spectrometer, to degas the samples prior to the measurements: in this way the peak referring to microscopic particles should not exist, allowing a more reliable investigation on the finer fractions.

In conclusion, a graph showing the peak dimension versus the iron concentration of the suspensions is provided below. The data refer to the suspensions prepared in 10 g/L CMC and to the weight-based PSDs. In case of multiple data, the mean value has been taken.

Size of the peak vs. STAR concentration



Graph 18 Mean value of peak size; comparison between spectrometer and disc centrifuge results

Both instruments show the same trend: the particle size is increasing with increasing concentration of iron; specifically, according to the previous considerations on the nature of the peaks, it is possible to affirm that larger clusters are formed when the NANOFER STAR concentration is higher.

In terms of applicability then, a smaller concentration of iron particles seems to be favorable for the mobility of particles injected in a porous medium: smaller clusters are formed. But, of course, small concentrations mean large volumes, and consequently long time and high costs. Hence, a compromise is always necessary.

5.1.5. Zeta potential – NANOFER STAR

The same samples used for the PSD determination (see Table 9) have been used at VEGAS for the evaluation of zeta potential: in effect, the spectrometer could perform the two measurements in sequence. Here too, the results were validated at Politecnico di Torino with a Zetasizer (ref. 4.2.8.3).

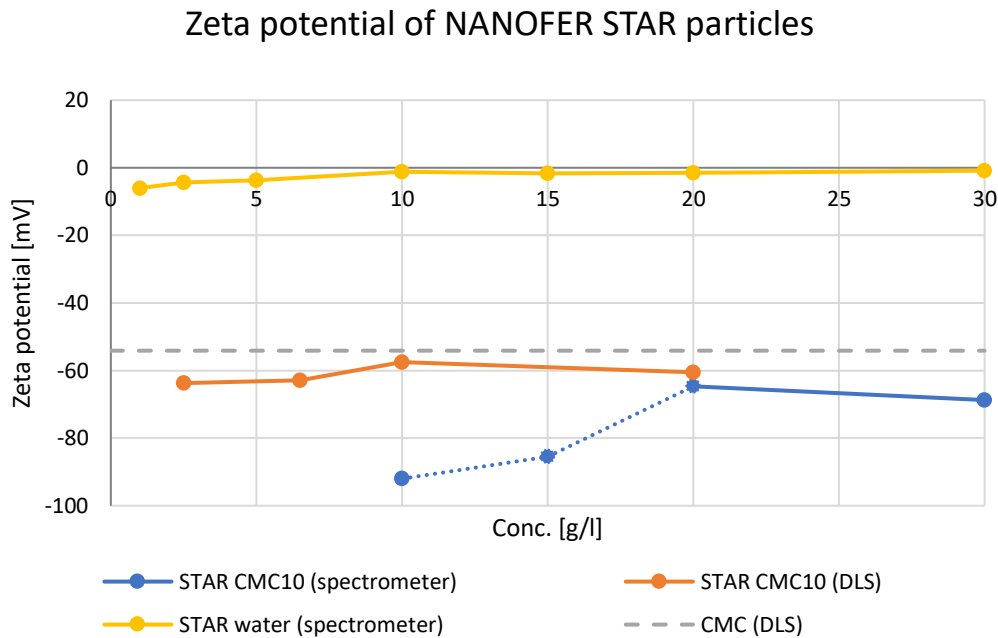
Also in this case, the spectrometer had some problems in measuring the smaller concentrations of iron: the inferior instrumental threshold of accuracy was again 10 g/L, so the results obtained with lesser concentrations were not reliable. On the other hand, however, the spectrometer allowed the measurements of more concentrated suspensions, which the Zetasizer could not measure with reliability: samples too dark impede the correct functioning of the instrument, based on light scattering.

The measurements carried out with the two instruments are the following:

- a) Zeta potential of CMC 10 g/L dissolved in VEGAS water (*background*);
- b) Zeta potential of NANOFER STAR particles (varying the concentration) in VEGAS water;
- c) Zeta potential of NANOFER STAR particles (varying the concentration) in CMC 10 g/L.

The results, showing the trend of NANOFER STAR zeta potential as a function of iron concentration, are presented below: the objective of this analysis was again to choose the best combination iron–polymer in terms of stability, to use later for the column tests. The background value of the zeta potential given by the CMC solution is also shown.

NB: The conditions in which the measurements were performed are relevant for the results. The pH of degassed VEGAS water is close to 8 (Table 2), while the pH of the suspensions approached 9. The ionic strength of the water, calculated with Eq. 12, is ca. 7 mM; the addition of 10 g/L of CMC does not have a strong influence on IS: its value remain practically unchanged. The samples were left to cool down before starting the experiments.



Graph 19 Representation of the zeta potential measurements. The grey, dashed line represents the value of potential given uniquely by the CMC dissolved in VEGAS water (background value); the blue, dotted line represents the values of the spectrometer measured close to the instrumental threshold and therefore not completely reliable

The previous graph demonstrates the influence of CMC in the stability of a colloidal system. The NANOFER STAR particles dispersed in just degassed tap water have a zeta potential very close to zero; therefore, the repulsive forces among them, according to the DLVO theory (3.3.3.3), are very weak. The preparation of the same suspensions in 10 g/L of CMC strongly improves the stability of the colloids.

Another consideration is that the zeta potential is quite constant with the concentration of iron; it is in fact a property of the single NANOFER STAR particle, not of the global suspension. In particular, Graph 19 shows that the results obtained with the DLS (orange line) fits with the one measured with the spectrometer (blue line), when the concentrations close to the spectrometer threshold of accuracy are left aside.

Lastly, it is possible to affirm that the stability improvement of the suspensions is exclusively given by the CMC addition: the potentials of particles in CMC (orange and blue line) lie just above the zeta potential measured for the CMC alone (grey, dashed line), taken as reference; no important dependency on the particle concentration is observed.

5.2. Porous medium properties

This section contains the major results regarding the determination of the properties of the porous medium. The characteristics of the packed sand columns, later used for further investigations, will be provided here.

5.2.1. Zeta potential – Sand grains

To have a quantification of the repulsive forces present between the NANOFR STAR particles and the sand grains of the solid matrix (ref. DLVO theory, section 3.3.3.3), in addition to that of particles, also the zeta potential of the medium has been measured.

In order to perform this test, the sand grains had to be milled in a mortar until they reached a very small size; in effect, since the result did not depend on the grain size distribution, the measurement has been carried out with only the Dorsilit sand. The VEGAS sand, being also made of Dorsilit, is most likely characterized by similar properties (for sand properties, see 4.1.4). The zeta potential results, obtained with a Zetasizer Nano at Politecnico di Torino, are reported in Table 11, both in VEGAS degassed water and in a 10 g/L CMC solution.

Table 11 Zeta potential of milled Dorsilit sand

Sample	ZP [mV]
Dorsilit in VEGAS water	-37.2
Dorsilit in CMC 10 g/L	-62.5

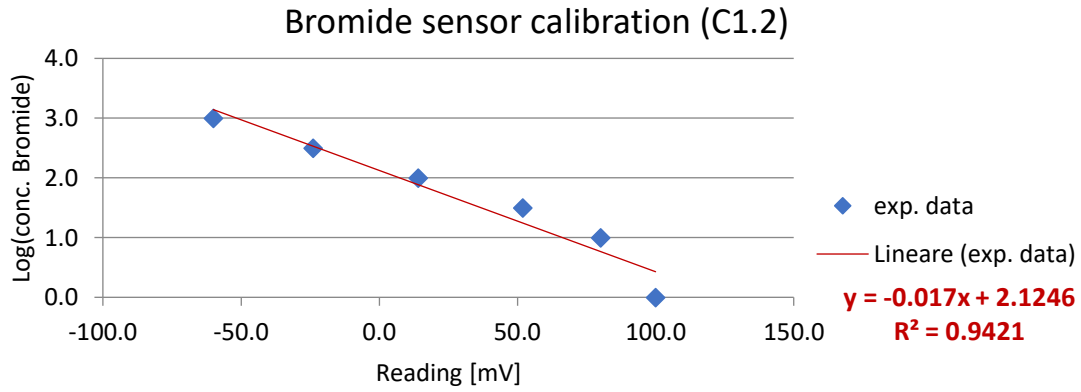
As demonstrated by the previous results, the zeta potential of Dorsilit sand was proved to be negative. This situation means that there is a certain repulsion between NANOFR STAR particles (see zeta potential results of the particles in section 5.1.5) and porous medium. Moreover, the addition of CMC seems to strengthen the repulsive interactions between particles and collector, hence improving the stability of the colloids. In general, in fact, the negative charge of both soil grain and particle surfaces is expected in usual environmental conditions ([Tirafferri, Tosco, & Sethi, 2011](#)).

5.2.2. Properties of the columns

For the evaluation of the characteristics of the sand columns, after the filling, both tracer tests and hydraulic conductivity tests have been performed (for the procedures see 4.2.10). Here, for brevity, only one example of each test will be completely explained (with reference to the column 1.2); for the other tests, only the final results will be provided.

5.2.2.1. Tracer test – column C1.2

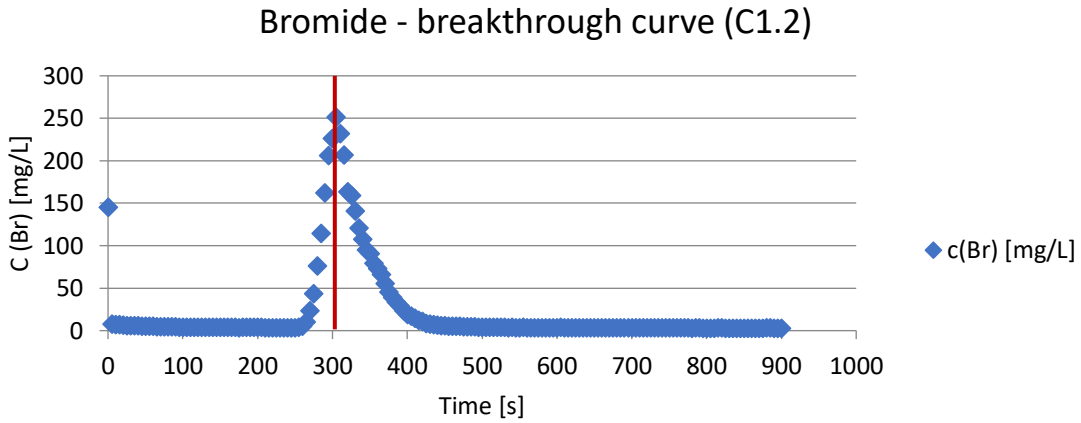
Before the execution of a tracer test, the bromide sensor had to be calibrated. To do so, known concentrations of bromide were injected in a flow cell while the sensor measured an electric potential in mV; later the concentration of Br^- was correlated with the signal using a diagram like the one reported below.



Graph 20 Calibration of bromide sensor prior to the tracer test of column C1.2

After the calibration phase, the actual test started. A concentration of 1000 mg/L of bromide was injected into the column with a pulse input, followed by degassed water; in the meanwhile, the bromide sensor was recording the signal every 5 seconds. The flow rate was chosen in such a way that about one pore volume ($1PV$) flowed through the column in five minutes. The volume corresponding to one PV, was simply estimated starting from the water content into the column, in turn evaluated by weighting the saturated and the dry column during its preparation.

The result of the tracer test was a curve like the following:



Graph 21 Breakthrough curve of the tracer test performed with column C1.2

Starting from the breakthrough curve of the tracer, evaluating the time in which the peak of concentration flowed out through the column, the effective (or pore) velocity v could be calculated as follows:

$$v = \frac{d}{t_{c.max}} \quad \text{Eq. 37}$$

where $d [L]$ represents the length of the column and $t_{c.max} [T]$ is the time corresponding to the maximum concentration of bromide registered at the outflow.

Knowing v and the Darcy's velocity q , the effective porosity ε of the column can be determined:

$$\varepsilon = \frac{q}{v} \quad \text{Eq. 38}$$

In addition, the shape of the curve and in particular its width, allowed the evaluation of the dispersivity α of the porous medium; the equations estimating the dispersivity are more complex than the ones for the determination of porosity. In this thesis the dispersivity was calculated from the longitudinal dispersion coefficient D_L as shown below:

$$\alpha = \frac{D_L}{v} \quad \text{Eq. 39}$$

In turn, the dispersion coefficient was evaluated from the tracer tests with the equation:

$$D_L = v^2 \frac{(t_{84\%} - t_{16\%})^2}{8 \cdot t_{50\%}} \quad \text{Eq. 40}$$

where $t_{16\%}$, $t_{50\%}$ and $t_{84\%}$ represent the times in which the 16%, 50% and 84% of the initial mass of the injected bromide was detected at the outflow by the sensor. These parameters basically describe the shape of the breakthrough curve, which is determined by the longitudinal dispersion coefficient.

In conclusion, effective porosity and dispersivity usually represent the objectives of a tracer test. The results of this and of the other tracer tests will be provided together in Table 13.

5.2.2.2. Hydraulic conductivity test – column C1.2

To evaluate the initial hydraulic conductivity K_0 of a column using the constant head method, Eq. 24 is applied. The section of the column A is known, as well as the length of the porous medium L . The difference in hydraulic head Δh upstream and downstream of the column is measured with a yardstick. The volume of water V that flows through the column in a certain time t is measured with a graduated cylinder.

Each measurement was repeated twice; if the results were consistent, the mean value was taken as K_0 , otherwise a third measurement was performed. An example regarding column C1.2 is shown below, while the results for all the columns are reported in the next section.

Table 12 Calculation of hydraulic conductivity for column C1.2

first test			second test		
Parameter	U.M.	Value	Parameter	U.M.	Value
A	[m ²]	0.00152	A	[m ²]	0.00152
L	[m]	0.498	L	[m]	0.498
Δh_1	[m]	0.71	Δh_2	[m]	0.71
V_1	[m ³]	4.05E-04	V_2	[m ³]	2.98E-04
t_1	[s]	150	t_2	[s]	110
K_1	[m/s]	1.24E-03	K_2	[m/s]	1.25E-03
			K_0	[m/s]	1.25E-03

The properties of the columns, calculated through the abovementioned tests, are reported in Table 13.

Table 13 Properties of the columns

Column ID	Sand	Inner Radius	Length	Cross-section	Bulk Volume	Bulk Density	Porosity	Pore Volume	Effective Porosity	Dispersivity	Initial Hydraulic Conductivity
		r	L	A	V _b	ρ _b	n	PV	ε	α	K ₀
		[m]	[m]	[m ²]	[m ³]	[kg/m ³]	[-]	[L]	[-]	[m]	[m/s]
C1.1	Dorsilit 8	2.20E-02	0.497	1.52E-03	7.56E-04	1573	0.451	0.3405	0.395	1.33E-03	9.62E-04
C1.2	Dorsilit 8	2.20E-02	0.498	1.52E-03	7.57E-04	1567	0.416	0.3149	0.404	9.44E-04	1.25E-03
C2.1	Vegas\ Dorsilit	2.20E-02	0.498	1.52E-03	7.57E-04	1841	0.337	0.2553	0.267	4.02E-03	7.34E-04
C2.2	Vegas\ Dorsilit	2.20E-02	0.490	1.52E-03	7.45E-04	1844	0.303	0.2260	0.264	7.40E-03	8.65E-04

5.3. Properties of CMC solutions

In this section the results involving the investigations on CMC rheology are reported. First, some tests with the viscometer have been performed, later some CMC column tests have been conducted for further evaluations.

5.3.1. Viscosity analysis

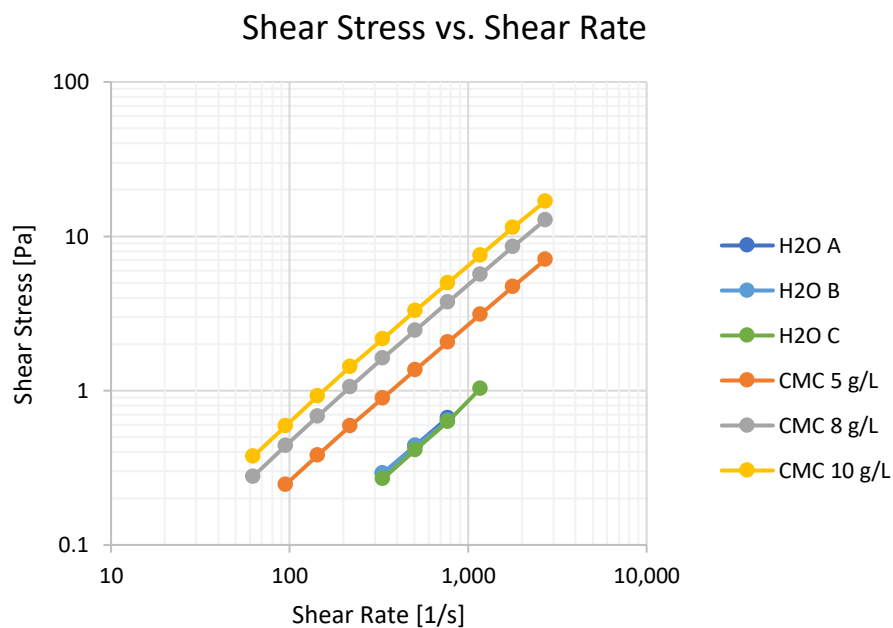
At VEGAS the evaluation of CMC rheological behavior has been conducted, at first, with a viscometer (see 4.2.11.1). Apart from the viscosity measurement, the objective of the test was to understand if the carrier of the suspended particles behaved as a shear-thinning fluid, with a viscosity that decreases with an increasing shear rate.

The samples prepared for this experiment were the following:

- Degassed VEGAS water (*background*);
- 5 g/L CMC dissolved in VEGAS water;
- 8 g/L CMC dissolved in VEGAS water;
- 10 g/L CMC dissolved in VEGAS water;

The results measured by the viscometer are represented in Graph 22, where the capital letters A, B, etc. refer to repetitions of the same experiment.

NB: Performing measurements on samples with very low viscosity is generally difficult for the viscometers; this is the reason why some samples only provided reliable results in a small range of shear rates.



Graph 22 Shear stress versus shear rate for water and different CMC concentrations

The previous graph shows that the curves shear stress versus shear rate are represented as straight lines for all fluids. These lines are typical of the behavior of a Newtonian fluid: the constant coefficient that links shear stress and shear rate is precisely the viscosity of the fluid; Eq. 41 displays Newton's law, which represents the definition of dynamic viscosity μ :

$$\mu = \frac{\tau}{\dot{\gamma}} \quad \text{Eq. 41}$$

in which τ [$M L^{-1} T^{-2}$] is the shear stress, $\dot{\gamma}$ [T^{-1}] is the shear rate.

A comparison of the previous graph is also possible with the following image, that shows the behaviors of different kinds of fluid; once again, the comportment exhibited by the samples is typically Newtonian.

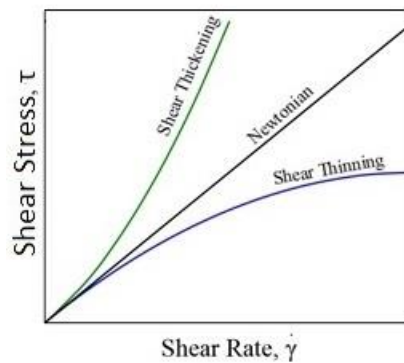
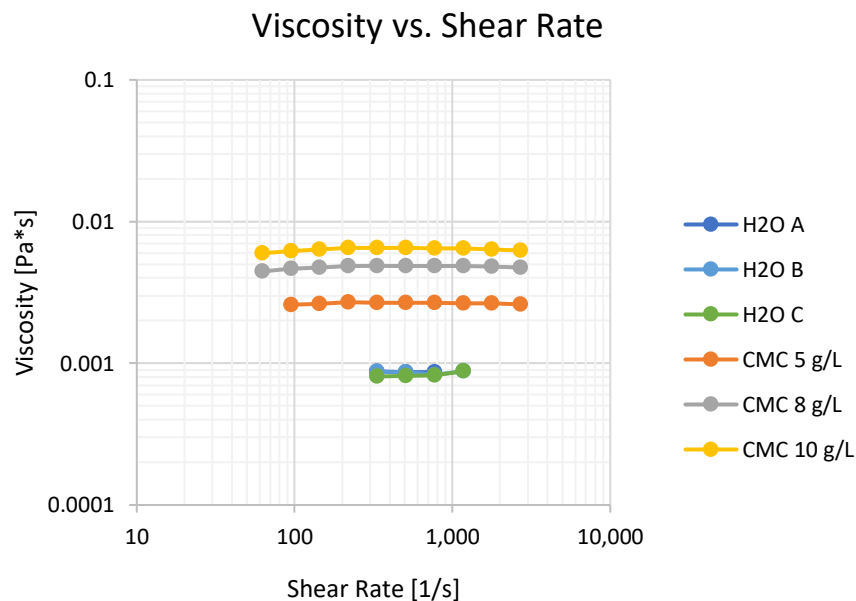


Figure 64 Shear stress vs. shear rate for different kinds of fluid (RheoSense - Simply Precise)

Moreover, the measuring system could also represent the values of viscosity versus the shear rate. These results are given below:



Graph 23 Rheogram of water and different CMC concentrations

The previous graph shows the crucial role of CMC in determining the viscosity of the solutions. In effect, for instance, it is worth noticing that the dissolution of 10 g/L CMC in water increases its viscosity of about ten times.

Also, the constant value of the viscosity with shear rate is demonstrated for all samples; one last time, this proves the Newtonian behavior of the fluids, as shown in Figure 65.

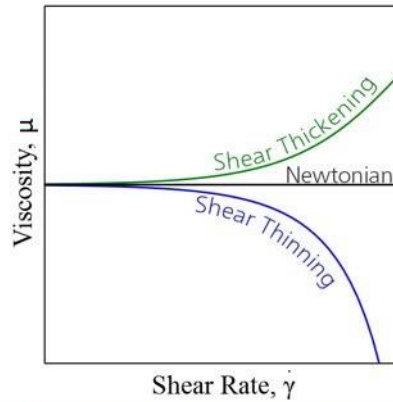


Figure 65 Viscosity vs. shear rate for different kinds of fluids (RheoSense - Simply Precise)

Despite the evident Newtonian behavior of the solutions in the viscometer, different conditions may occur inside the porous medium, when the fluid is flowing through the pores of the solid matrix. In particular, it is very complex to identify the shear rates perceived by the flowing fluid in the column. An estimate may be possible using Eq. 36, but the determination of the parameters is still complicated.

A different approach to investigate the rheological behavior of CMC solutions flowing in the porous media is described in the next section.

5.3.2. CMC column tests

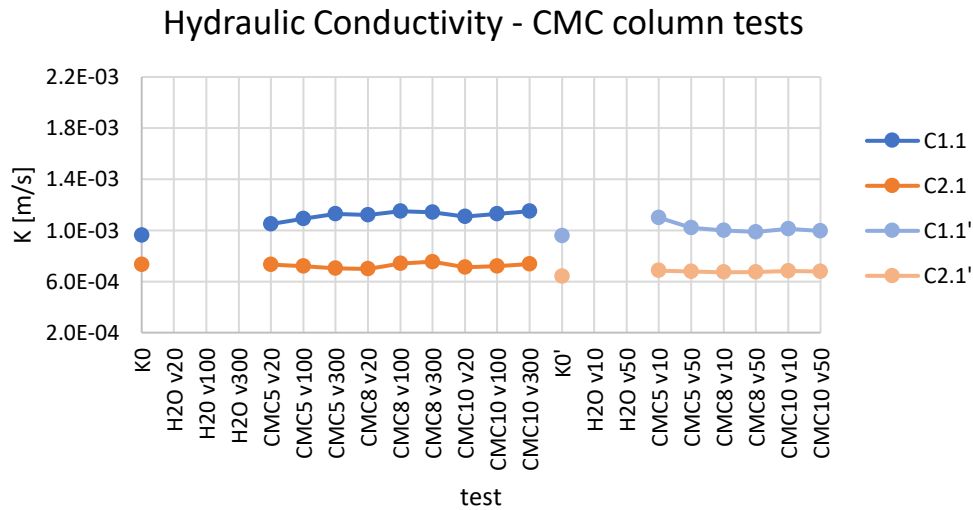
The columns C1.1 and C2.1 have been used for the injection of different concentrations of CMC with different injection velocities. The objective was to investigate the rheological behavior of the CMC solutions while flowing through the porous media. The test has been conducted in this way: for each column, 4 solutions of CMC at different concentrations (0 g/L, 5 g/L, 8 g/L and 10 g/L) have been injected with 5 different injection velocities (10 m/d, 20 m/d, 50 m/d, 100 m/d and 300 m/d, with reference to the seepage velocity). The choice of both concentrations and velocities was based on previous experiments performed at VEGAS, also trying to represent plausible field conditions. Between each injection, a hydraulic conductivity test was performed, to identify the occurrence of flow variations in the porous medium.

The experiment was carried out in two moments; at first, the CMC solutions were injected with 20, 100 and 300 m/d, later also 10 and 50 m/d were added, with the aim of investigating in detail that range of velocities.

The chronological order with which the solutions were injected can be inferred from the following graph, that shows the variations in hydraulic conductivities of the two columns after each test; the initial conductivity is expressed as K_0 .

NB: After the injection of just water, the conductivity test was not performed.

NB: The apostrophe identifies the second set of experiments.

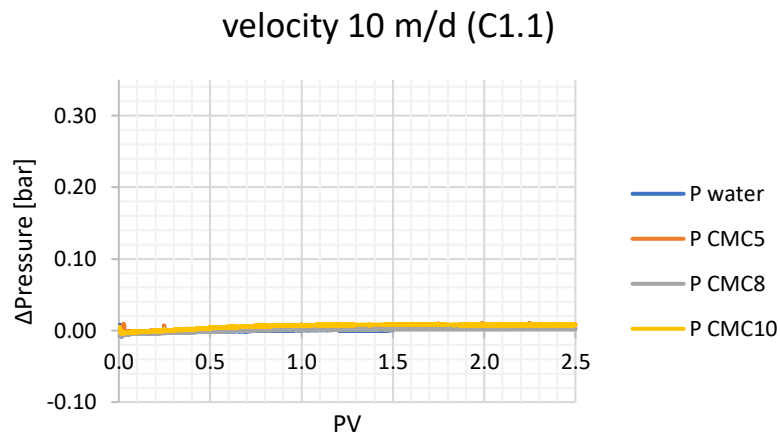


Graph 24 Trend of hydraulic conductivities. K0 and K0' represent the hydraulic conductivities before the first and the second set of experiments respectively; all the other points represent the results of the hydraulic conductivity tests performed after each CMC injection (e.g. CMC5 v20 represents the conductivity measured after the injection of 5 g/L of CMC at 20 m/d seepage velocity, and so on)

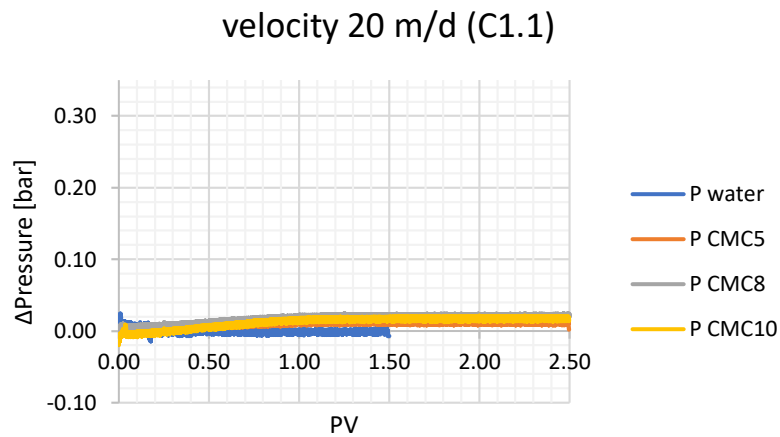
As demonstrated from the graph, the hydraulic conductivities calculated with Eq. 24 stayed almost constant during all the tests; a small decrease is visible in both columns after the conductivity test K_0' : in effect, some days passed from the conclusion of the tests *CMC10 v300* and the new set of experiments, and so the sand in the columns, left in vertical position, became more compact. The variation however is very slight.

The tests have been conducted following the procedure described in 4.2.11.2. The differential pressure between two pressure sensors, located upstream and downstream of the column was evaluated along the injection.

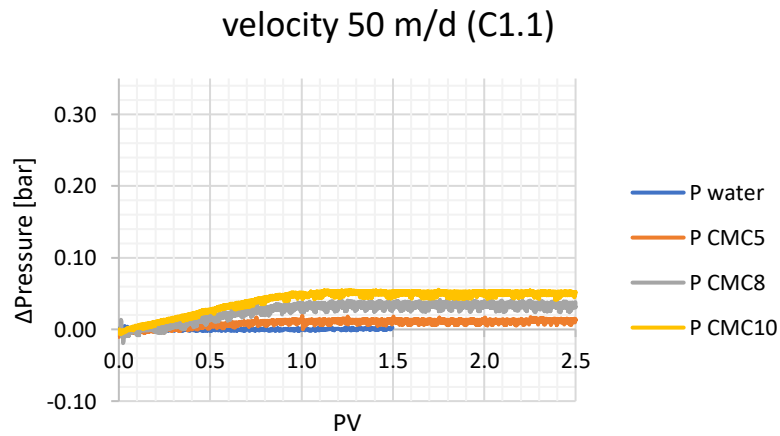
The results obtained with column C1.1, showing the comparison between different CMC concentrations, are reported below. The Y-axis is kept the same in all graphs to allow a direct comparison between one another.



Graph 25 Differential pressure caused by water and by different CMC concentrations injected in column; seepage velocity 10 m/d, column C1.1

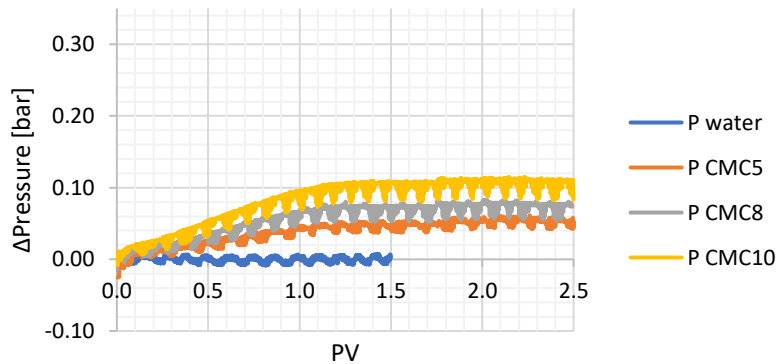


Graph 26 Differential pressure caused by water and by different CMC concentrations injected in column; seepage velocity 20 m/d, column C1.1



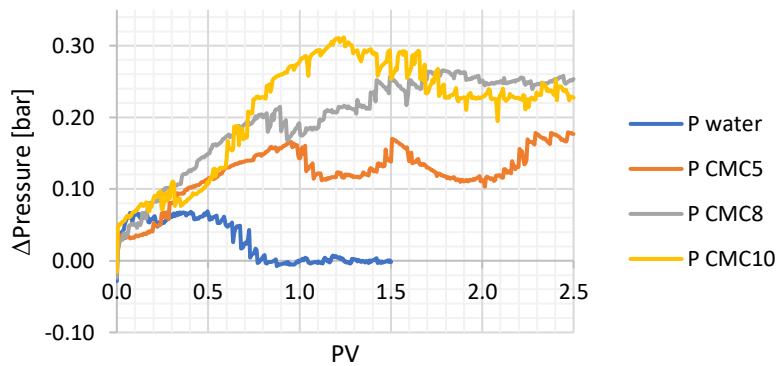
Graph 27 Differential pressure caused by water and by different CMC concentrations injected in column; seepage velocity 50 m/d, column C1.1

velocity 100 m/d (C1.1)



Graph 28 Differential pressure caused by water and by different CMC concentrations injected in column; seepage velocity 100 m/d, column C1.1

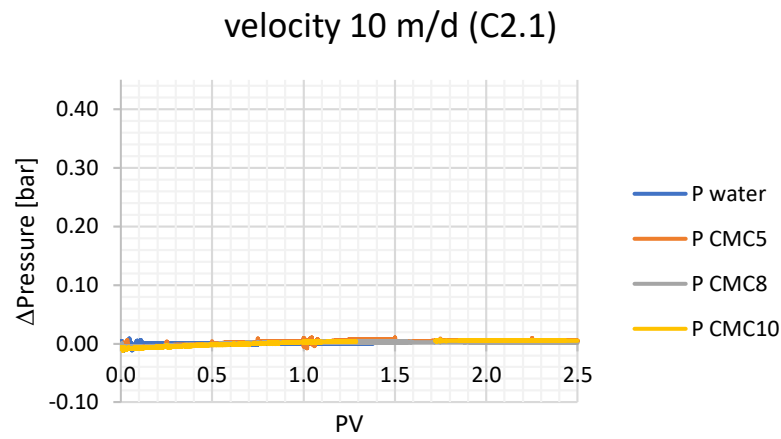
velocity 300 m/d (C1.1)



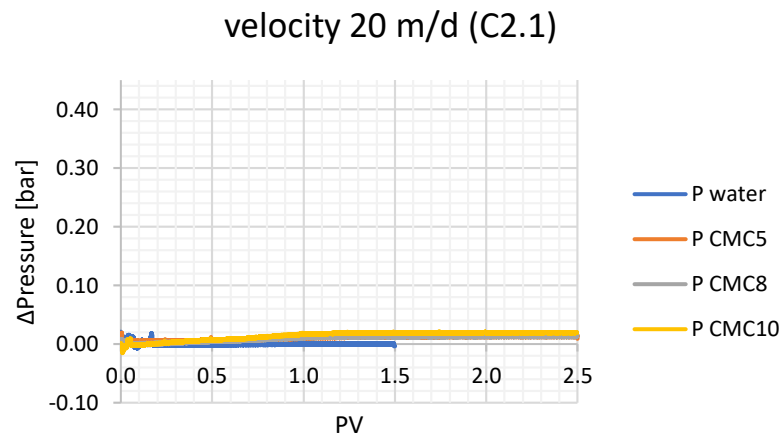
Graph 29 Differential pressure caused by water and by different CMC concentrations injected in column; seepage velocity 300 m/d, column C1.1

The results show that the differential pressure is increasing with velocity, as well as with CMC concentration of the solutions. According to Darcy's law, an increase in pressures due to an increase in the fluid viscosity has to be expected if the other conditions stay equal (ref. Eq. 25). Then, it is apparent that Graph 29 represents a strange behavior of the pressures; it might be that the high velocity of injection (300 m/d) caused the flow to exit from a Darcian regime, with impending turbulence. In effect, the calculation of the Reynolds number in this situation (ref. Eq. 26) returns values close to or higher than 1 (for instance, $Re = 1.7$ for water). For the other velocities instead, the flow is definitely within the Darcian regime.

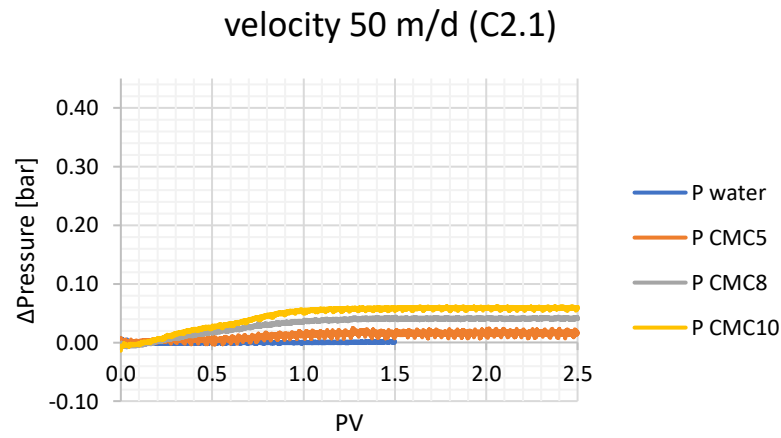
Similar considerations are possible for the results obtained with the column with VEGAS sand (C2.1), shown below. Once again, the differential pressure increases with increasing injection velocity or with increasing CMC concentration.



Graph 30 Differential pressure caused by water and by different CMC concentrations injected in column; seepage velocity 10 m/d, column C2.1

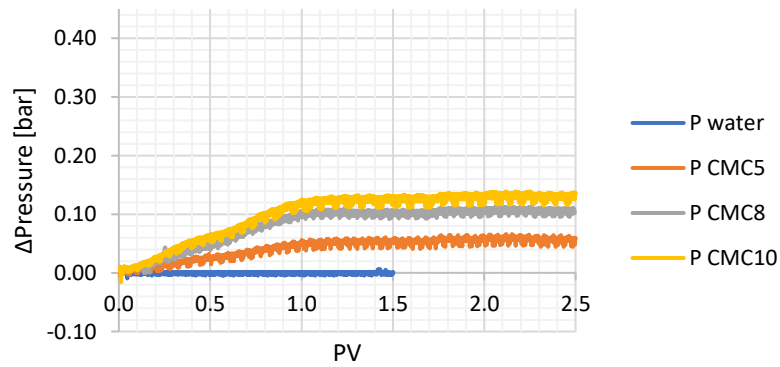


Graph 31 Differential pressure caused by water and by different CMC concentrations injected in column; seepage velocity 20 m/d, column C2.1



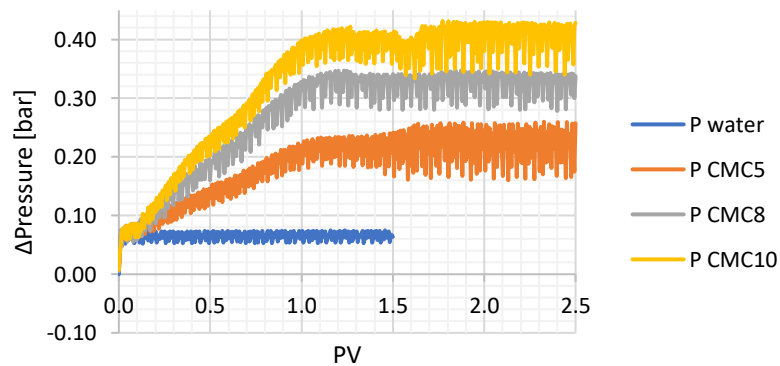
Graph 32 Differential pressure caused by water and by different CMC concentrations injected in column; seepage velocity 50 m/d, column C2.1

velocity 100 m/d (C2.1)



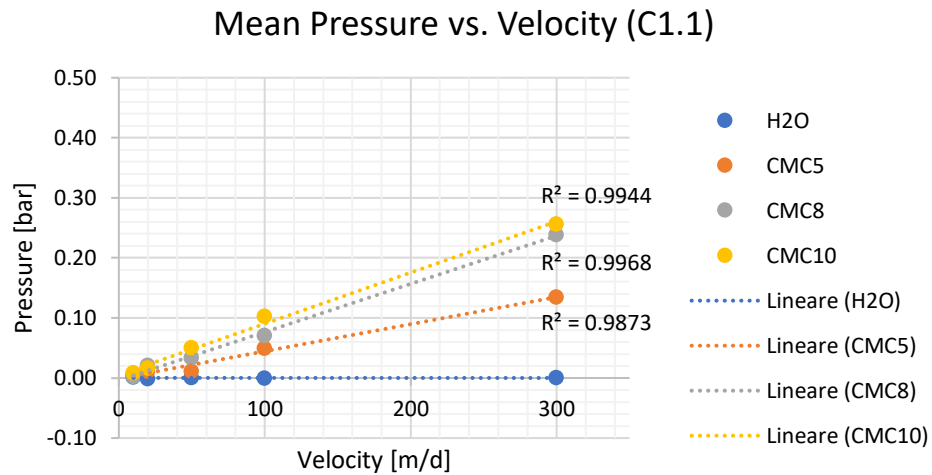
Graph 33 Differential pressure caused by water and by different CMC concentrations injected in column; seepage velocity 100 m/d, column C2.1

velocity 300 m/d (C2.1)

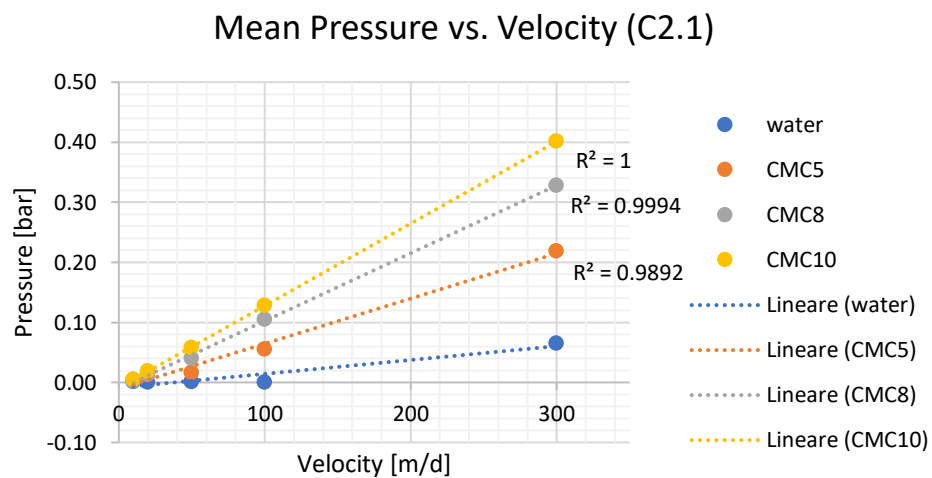


Graph 34 Differential pressure caused by water and by different CMC concentrations injected in column; seepage velocity 300 m/d, column C2.1

These experiments aimed at understanding the rheological behavior of the CMC solutions into the solid matrix. To investigate this fact, the ΔP mean value of the curve plateau has been extracted from the previous graphs and plotted as a function of the correspondent injection velocity, as explained in 4.2.11.2. The results, for both columns, are provided below.



Graph 35 Pressure corresponding to the plateau of each injection versus injection velocity, column C1.1



Graph 36 Pressure corresponding to the plateau of each injection versus injection velocity, column C2.1

The curves in the previous graphs demonstrate once again the Newtonian behavior of the injected suspensions flowing in the porous media: a change in the slope of the curves, as already explained before, would suggest a variation of the dynamic viscosity of the fluid. The straight lines on the other hand confirm that the viscosity is constant with increasing velocity and therefore also with increasing shear rates experienced by the fluid in the pores of the solid matrix (ref. Eq. 36). In fact, there is a direct proportionality between pressure and velocity, as expressed by Darcy's law (Eq. 25).

Finally, from the samples collected at the outflow, the breakthrough curves could be evaluated. These curves are represented together with the NANOFER STAR breakthrough curves, to allow an easier comparison.

5.4. NANOFER STAR column tests

In the present section the results of the transport tests performed with injection of NANOFER STAR suspensions will be presented. It is important to remind that the previous tests were oriented to better plan this experiment, choosing the best combination of particles and CMC in terms of particle size, stability of the suspensions and properties of the carrier fluid. In particular, the particles were demonstrated to form bigger aggregates when dispersed at higher concentrations (see Graph 18) and the sedimentation tests showed that higher concentrations are likely to settle faster than smaller ones (see Graph 2); on the other hand, the repulsions between suspended particles showed no evident dependence on the NANOFER STAR concentration: the zeta potential stayed almost constant (see Graph 19). Lastly, the CMC solutions exhibited a Newtonian behavior for all the concentrations analyzed (see Graph 22, Graph 23, Graph 35 and Graph 36); however, they played an important role in increasing the viscosity of the fluid and in determining a higher zeta potential for both the iron particles and the sand grains (see Graph 23, Graph 19 and Table 11).

In conclusion, the combination chosen for the following tests was 10 g/L NANOFER STAR in 10 g/L CMC. In this way the particle concentration was a good compromise between too high concentrations, proved unstable, and too low concentrations, which are not effective in a hypothetical field application. The chosen CMC concentration determined a high increase in viscosity of the suspensions, likely to hinder the sedimentation process and therefore improve the transport; at the same time however, it was proved that this concentration did not cause an excessive rise in the pressures during the column tests.

The velocity of injection instead, was chosen 100 m/d (pore velocity), based on the results obtained by Accolla (2017) in previous experiments performed at VEGAS.

The results of these tests are provided below, divided for the two different sets of columns.

5.4.1. Column 1.n – Dorsilit 8 sand

5.4.1.1. Column C1.1

The initial intention was to attempt an injection of NANOFER STAR into the columns already used for the CMC tests. However, the porous medium was probably disturbed, and some air bubbles may have entered the column during the processes of connecting and disconnecting the pipes. For these reasons, it was preferable to prepare another column, with analogous properties.

Figure 66 shows the qualitative tracer tests performed to verify the presence of preferential flow paths; the column was not suitable for being used in further tests.

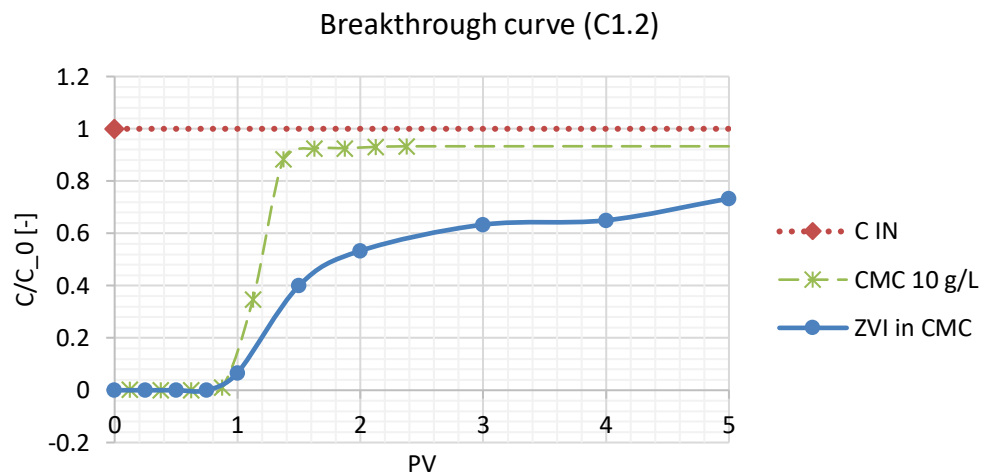


Figure 66 Qualitative tracer test

5.4.1.2. Column C1.2

The chosen suspension (10 g/L NANO FER STAR in 10 g/L CMC) was injected in column C1.2 for 10 PVs. The test was performed as explained in 4.2.12, starting with an injection of degassed VEGAS water, followed by a solution of 10 g/L CMC, and finally with the iron particles. At the end of the experiment, the column was flushed with 2 PVs of degassed water, until the outflow did not contain iron anymore.

The collection of the outflow samples along the test, allowed the representation of the breakthrough curve, reported below in comparison with the breakthrough curve obtained with the CMC test of the solution 10 g/L, injected with the same velocity in column C1.1. Only the first 5 PVs are represented, being the most interesting part of the experiment.

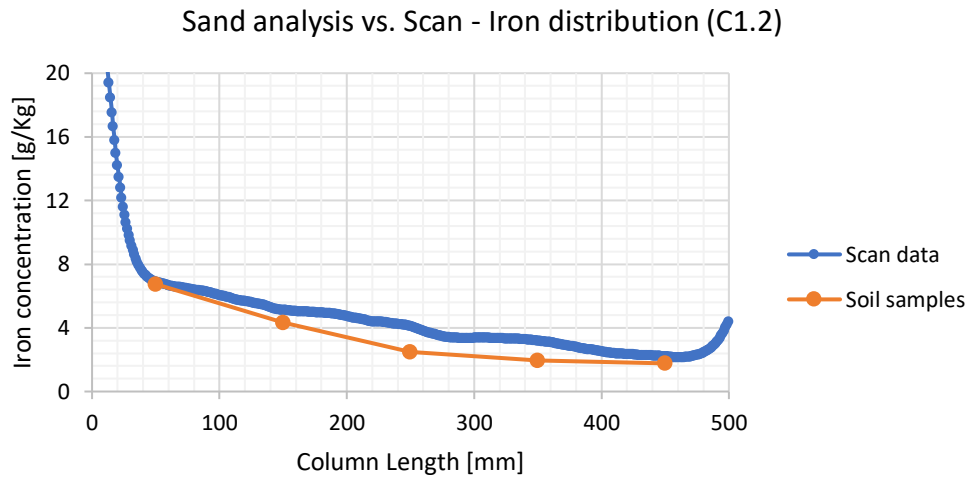


Graph 37 Breakthrough curves of particles and of CMC, column C1.2

It is important to say that, even if the suspension in the mixed tank was prepared at 10 g/L particle concentration, the injecting system caused a certain settling of the iron particles, which entered the column with a concentration of ca. 6.5 g/L. This is the reason why this specific concentration was chosen, retrospectively, in the tests conducted at Politecnico di Torino.

The breakthrough curve in Graph 37 is built from experimental data; the concentration of iron in each sample was measured with the hydrogen evolution method (see 4.2.5); the breakthrough curve for the CMC 10 g/L was evaluated during the CMC column tests, measuring the electrical conductivity of the collected samples in relation to that of the injected solution. The two curves start increasing at about 0.8 PVs, but the CMC solution almost behaves like a tracer, practically reaching the initial concentration at about 1.5 PVs; the particles instead, take about 2 – 3 PVs to reach stable conditions; the outflow concentration is ca. 60 – 70% of the starting one, meaning that the remaining part is sedimented along the column.

To understand how the iron mass inside the column was distributed, two measurements were available: the results of the magnetic susceptibility scanner and the sand samples, collected opening the column at the end of the experiment and analyzed with the hydrogen method. These two pieces of information are presented together in the graph below.



Graph 38 Iron distribution; comparison between scanner data and laboratory data, column C1.2

Graph 38 shows the results of the zerovalent iron distribution inside the column. The two methods of analysis provided consistent results. The achieved distribution of the ZVI however is definitely not optimal: the particles were deposited in high concentrations in the first centimeters of the column, being transported further only in much lower concentrations. It is possible that some of the bigger aggregates detected during the particle size analysis were immediately filtrated by the porous medium, and only a smaller fraction could effectively travel greater length into the column and finally being collected in the sampling bottles. The breakthrough curve is in fact quite high, but the bigger part of the sedimented mass is concentrated at the inlet of the column. Of course, this is not the situation desired in a field application, where a well-distributed area of iron is required for an efficient remediation of a contaminated zone.

Afterwards, the mass balance regarding the iron was calculated. From the total iron mass injected into the column, it was subtracted the amount collected at the outflow; the difference between these two values gives an esteem of the mass of iron deposited inside the column. In the calculation it was also important to consider the mass of iron flowed out of the column during the flushing phase: in this way the result of the mass balance was directly compared to the iron detected in the sand through laboratory analyses.

The procedure can be expressed with the following equation:

$$M_{IN} - M_{OUT,test} - M_{OUT,flushing} = M_{INSIDE} \quad \text{Eq. 42}$$

The mass balance referring to column C1.2 is presented in the following table; the calculations account for all the 10 PVs of the NANOFE STAR injection.

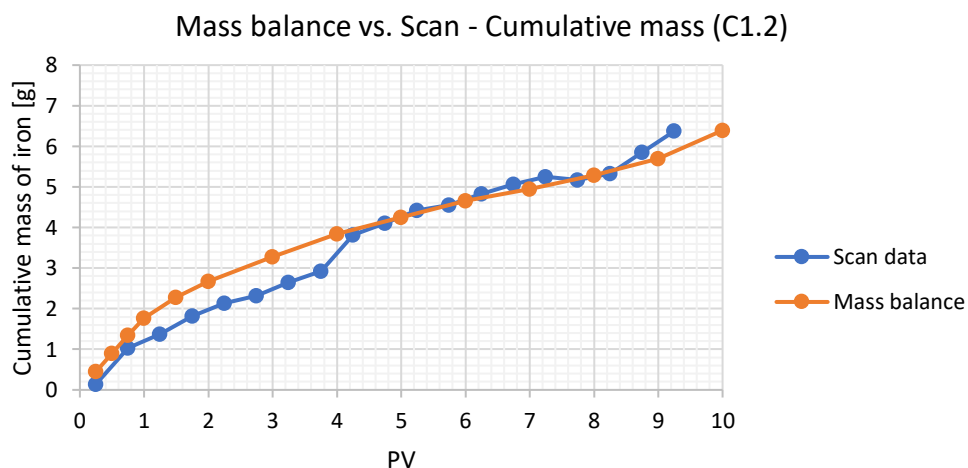
Table 14 Mass balance, column C1.2

M_{IN}	18.89 g
$M_{OUT,test}$	12.50 g
M_{INSIDE}^* , before the flushing	6.39 g
$M_{OUT,flushing}$	1.04 g
M_{INSIDE} , after the flushing	5.35 g

NB: The value of the mass inside the column before the flushing (M_{INSIDE}^) has been used for the calibration of the magnetic susceptibility scanner.*

Through the mass balance, the iron mass deposited inside the column and attached to the porous medium was evaluated to be ca. 5.35 g, while the iron mass before the flushing was 6.39 g; this value represents almost the 34% of the starting iron mass. In effect, the breakthrough curve showed that about the 65% of iron flowed through the column and about the 35% stayed inside. Then, the value of 5.35 g can directly be compared to the total mass of iron detected from the soil analyses, which reported 4.91 g.

Moreover, it is possible to evaluate the mass balance at different times and create the cumulative curve of iron deposited into the column. This curve can be compared with the results of the total mass inside the column detected by the scanner. The results are displayed below.

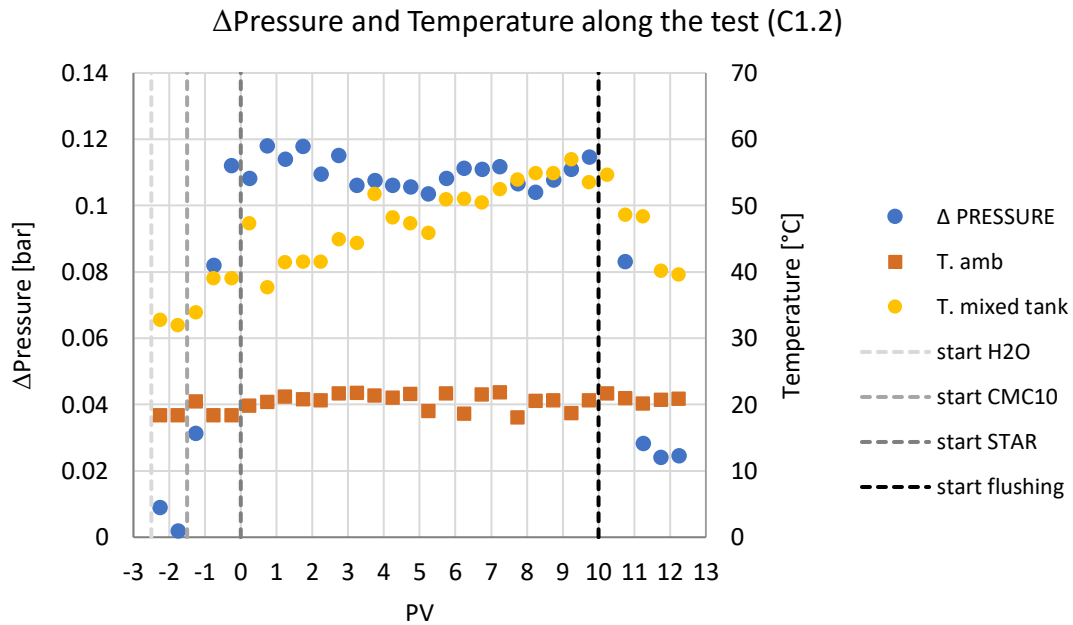


Graph 39 Cumulative mass; comparison between scanner data and mass balance, column C1.2

Then, the pressure and temperature data measured during the all test (from the injection of water to the final flushing) are reported below, in Graph 40. Some considerations can be made:

- The room temperature stayed nearly constant all along the test;
- The temperature inside the mixed tank, from which the NANO FER STAR particles were taken for the injection, increased drastically during the test, starting from a value of ca. 30°C and almost reaching 70°C. This fact is relevant, because the high temperatures may reduce the viscosity of the suspension, hence strongly reducing the stability of the colloidal system (see Graph 3). This element may have an important role in the initial deposition of the particles observed in the column;

- c) The differential pressure started to grow in the phase of injection of the CMC, reaching the same values of the CMC column test (see Graph 28); after that, when the particles were injected, it stayed almost constant, only decreasing during the final phase of flushing. This information reveals that the clogging of the porous medium did not occur, even if high concentrations of particles were deposited at the inlet of the column. However, the fact that the pressures did not reach completely the zero anymore, means that some pores were occluded by the deposited particles.



Graph 40 Parameters monitored during the NANOFE STAR test, column C1.2

Furthermore, after the injection another hydraulic conductivity test was performed, to compare the result with the one obtained before the injection. In Table 15 the two values are shown:

Table 15 Hydraulic conductivity before and after the column test, column C1.2

K_0 [m/s]	K [m/s]
1.25E-03	6.88E-04

The deposition of iron inside the column slightly modified the hydraulic conductivity. This information is in accordance to the analysis of pressures, which do not have a complete recovery after the flushing.

In conclusion, some pictures of the column are provided.

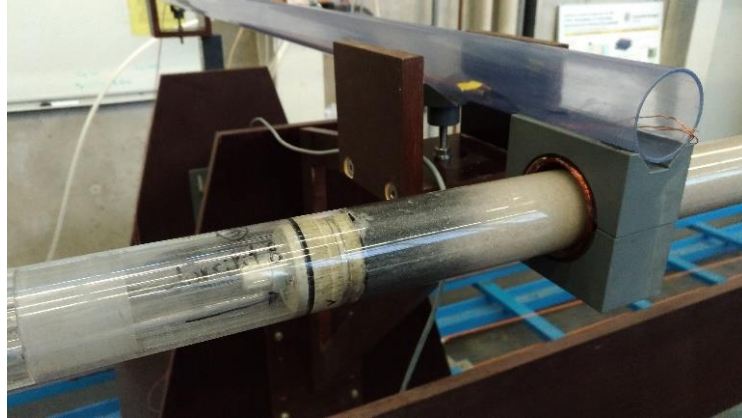


Figure 67 Initial stages of NANOfer STAR test, column C1.2

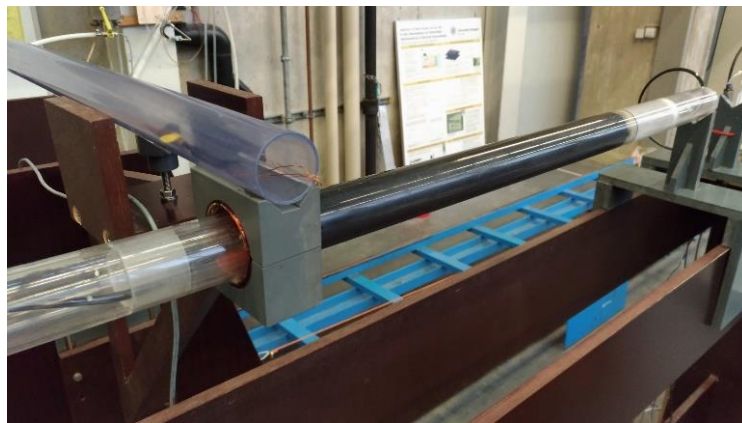


Figure 68 Final stages of NANOfer STAR test, column C1.2

5.4.2. Column 2.n – VEGAS\Dorsilit sand

5.4.2.1. Column C2.1

To demonstrate that after the CMC tests the porous medium of the column C2.1 was disturbed, the injection of NANOfer STAR particles was attempted. The particles immediately showed the presence of preferential flow paths, primarily caused by air bubbles inside the column; the experiment was stopped, and the results discarded. Thus, another column with similar properties was prepared to conduct a proper test.

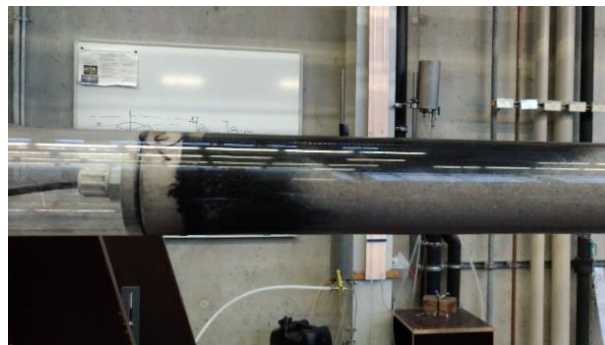
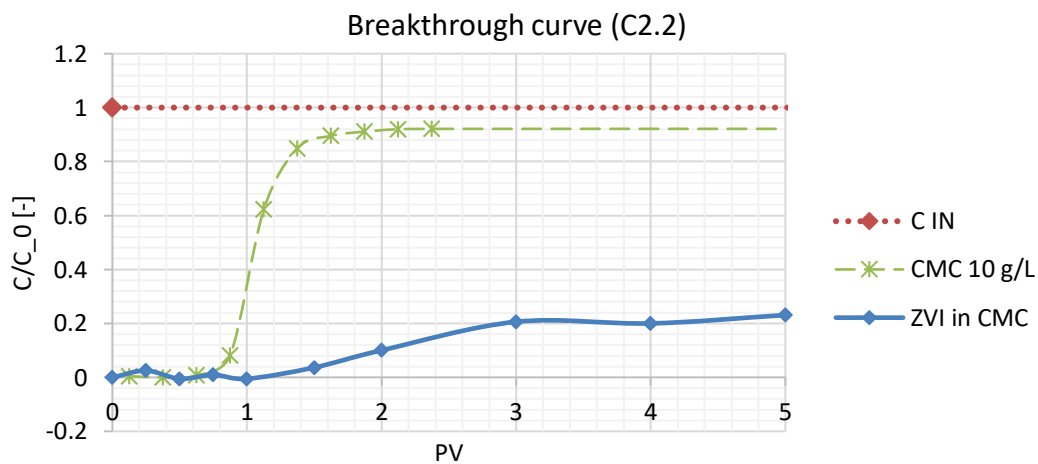


Figure 69 Transport test showing the presence of preferential flow paths

5.4.2.2. Column C2.2

Here again, the suspension 10 g/L NANOFER STAR in 10 g/L CMC was injected in column C2.2 for 10 PVs; however, as explained for the column C1.2, the actual concentration entering the column was ca. 6.5 g/L. Before the particles, degassed water and CMC were injected for 1 and 1.5 PVs respectively. At the end, 2 PVs more of degassed water were flushed, to remove the iron in the liquid phase and analyze the deposited one. Although the test was continued until the end, at about 5.25 PVs the magnetic susceptibility sensor touched the column during a scan; this event resulted in a movement of the column which fell for about 20 cm. Since it is probable that this movement altered some of the initial conditions of the test, some of the results (e.g. the breakthrough curve) will be shown just until the 5th PV; fortunately, in effect, the particle concentration reached a steady state before the incident.

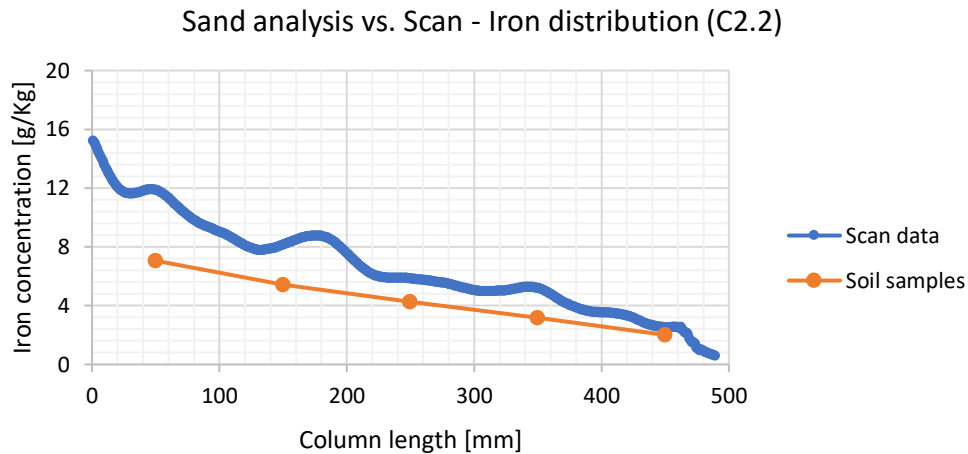
The ZVI breakthrough curve, compared with the one of just CMC 10 g/L is shown below.



Graph 41 Breakthrough curves of particles and of CMC, column C2.2

Compared to that of the other column, the ZVI breakthrough curve in Graph 41 is much lower: only about the 22% of the injected iron passes all through the column, while the greatest part is deposited along the column itself. This curve seems even lower if compared with the breakthrough curve of the CMC 10 g/L, that almost reached the initial concentration. The high retention of iron can be explained by the presence, in C2.2, of a heterogeneous medium, with a very fine fraction of sand. In this sense, the average grain size of the two sands can be misleading: it seems, in effect, that since the Dorsilit 8 has a smaller d_{50} (0.57 mm compared to ca. 1.2 mm of the VEGAS sand), it should be made of finer grains. However, if a smaller diameter is considered, d_{10} for instance, it is possible to ascertain that the VEGAS sand is composed by a fraction of very smaller grains. This fine fraction is indeed the main responsible of the filtration of NANOFER STAR particles and aggregates.

In accordance with the previous considerations, the distribution of deposited iron along the column resulted in higher concentrations, compared to those measured for the column C1.2. In this case a bigger discrepancy between the results of the scanner and the ones obtain from the soil samples was observed. However, for this column the distribution of ZVI in the sand was quite homogeneous, without the initial peak previously noticed. The data are reported below.



Graph 42 Iron distribution; comparison between scanner data and laboratory data, column C2.2

Also for this test, a mass balance was performed using Eq. 42. The same considerations made for the column C1.2 are valid; the results are listed below:

Table 16 Mass balance, column C2.2

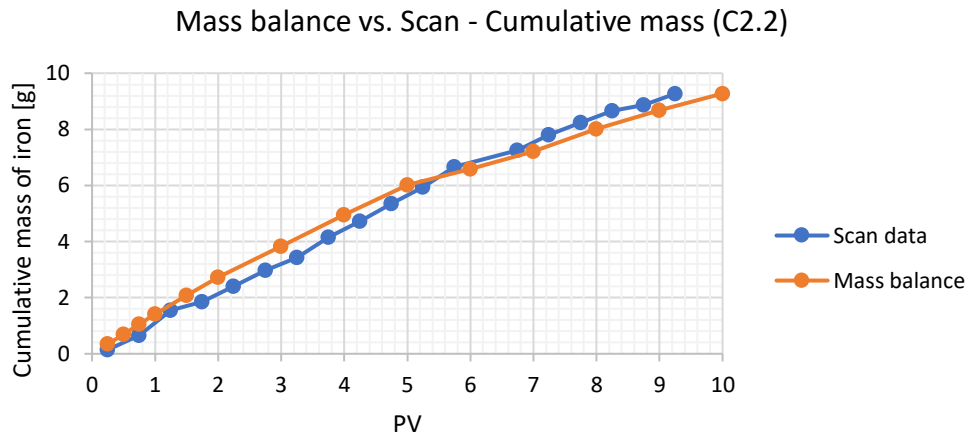
M_{IN}	14.92 g
$M_{OUT,test}$	5.64 g
M_{INSIDE}^* , before the flushing	9.28 g
$M_{OUT,flushing}$	0.57 g
M_{INSIDE} , after the flushing	8.71 g

NB: The value of the mass inside the column before the flushing M_{INSIDE}^ , has been used for the calibration of the magnetic susceptibility scanner.*

The estimated iron mass inside the column (8.71 g) was compared with the iron mass detected in the soil samples (6.59 g). Similarly to the results in Graph 42, once again the laboratory analyses gave smaller values compared to those evaluated through a different method (the magnetic sensor before, the mass balance now). Then, it is relevant to observe that the mass value calculated before the flushing (9.28 g) represent the 62% of the initial mass; the breakthrough curve, drawn for just the first 5 PVs suggests instead that 78% of the initial mass is inside the column. The discrepancy between the two values is due to the final stage of the test, where the movement of the column caused the iron outflow to considerably increase.

When comparing the data obtained from the scan and those evaluated through the mass balance, the fitting between the results is much better; however, a change in the slope of the cumulative mass is visible at the 5th PV, and this explains the disagreement of the two percentages calculated above.

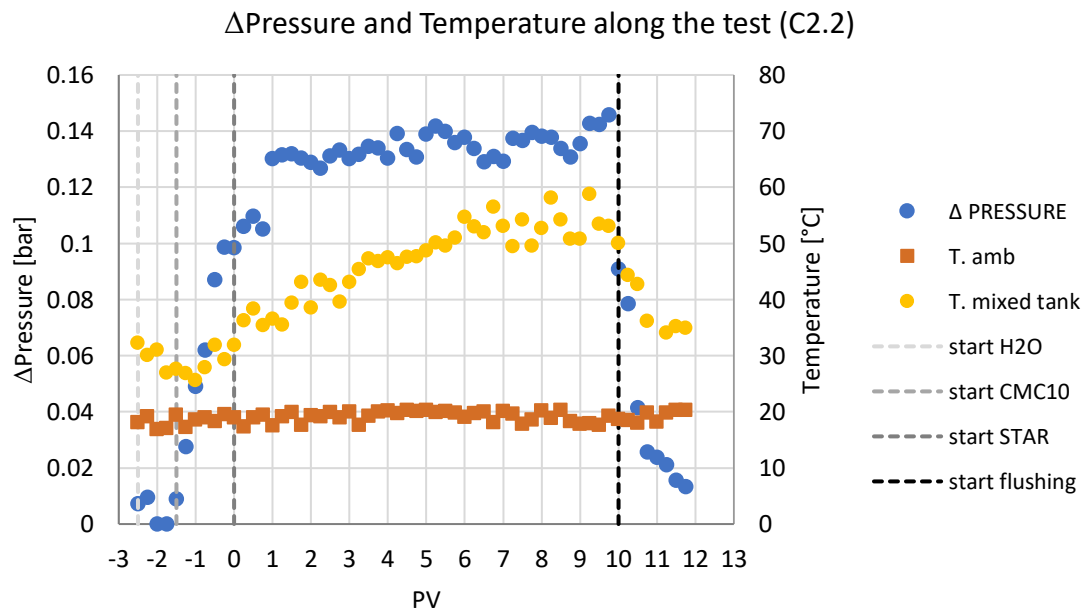
In Graph 43 the cumulative mass of iron deposited into the column is compared with the iron mass detected by the scanner inside the column.



Graph 43 Cumulative mass; comparison between scanner data and mass balance, column C2.2

Later, the pressure and temperature data of the overall test are reported, with the aim of getting some additional information. Referring to Graph 44, the following considerations can be made:

- The room temperature was almost constant for the entire test;
- The temperature inside the mixed tank, similarly to what observed for the test C1.2, increased from about 30°C until almost 60°C . Here too, the big change of temperature may have influenced the test, determining a change in the suspension viscosity; in turn, this variation may influence the stability of the NANO FER STAR particles (see Graph 3);
- The differential pressure registered by the pressure sensors began to increase during the CMC injection; it almost reached 0.12 bar , in accordance with the results of the CMC column tests (see Graph 33). Moreover, it is important to notice that the differential pressure slightly increased again when the NANO FER STAR particles were injected, reaching the $0.14 - 0.15\text{ bar}$ at the end of the test. Then, a drop of the pressures was registered during the final flushing, with a trend that seems to reach almost the starting value.



Graph 44 Parameters monitored during the NANO FER STAR test, column C2.2

Also for this column, the comparison between the hydraulic conductivity tests (before and after the injection of particles) is displayed.

Table 17 Hydraulic conductivity before and after the column test, column C2.2

K_0 [m/s]	K [m/s]
8.65E-04	5.09E-04

Here too, a variation in the hydraulic conductivity is present: some pores of the column may be occluded by the deposited particles and the flow of the water is marginally impeded.

Finally, some pictures showing the distribution of iron obtained in this test are provided below.



Figure 70 Final distribution of iron in column C2.2



Figure 71 Soil samples collected from column C2.2

5.5. Modeling with MNMs

In this section some of the tests performed will be evaluated with the software MNMs, with the aim of investigating more in detail certain aspects; moreover, some new simulation will be conducted, starting from the data measured and collected before.

5.5.1. DLVO profiles

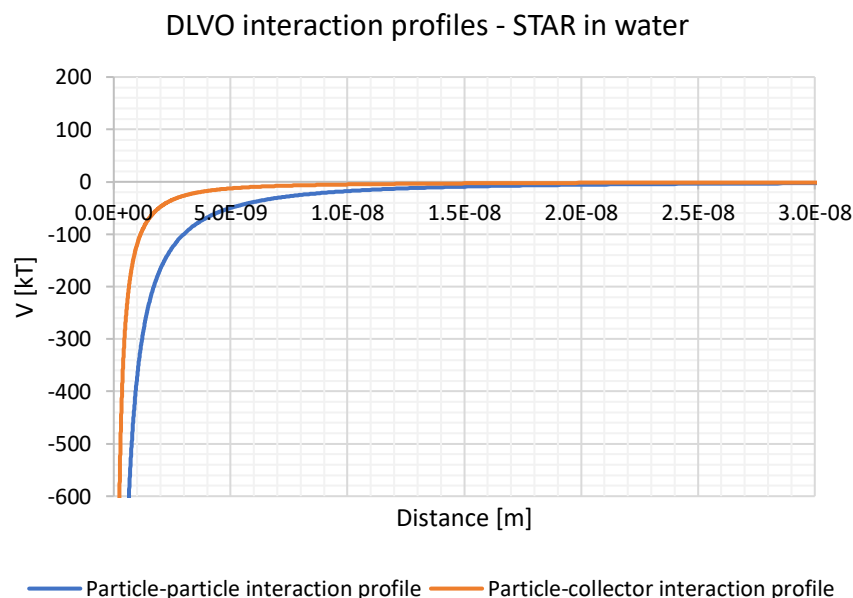
As already said, through MNMs it is possible to evaluate the DLVO energy profiles of particles and sand grains. In this way, an evaluation of the particle–particle and particle–collector interactions can be made. The fundamental information to draw these profiles is the zeta potential measurement of both the materials, reported in 5.1.5 and 5.2.1; then, it is also necessary to calculate the ionic strength of the liquid phase.

In particular the interactions have been evaluated for a suspension prepared in VEGAS degassed water, in comparison to another suspension prepared in a CMC 10 g/L solution. The results are presented in the following. In VEGAS degassed water, the calculated ionic strength and the measured zeta potentials, used for the evaluation of the DLVO energy profiles, are reported below:

Table 18 Data for DLVO profile in degassed VEGAS water

Ionic strength	Collector zeta potential - ZETASIZER	Particle zeta potential - SPECTROMETER
[mM]	[mV]	[mV]
7	-37.2	-1.2

The consequent DLVO profiles evaluated by MNMs are provided in Graph 45. It is worth noticing that the energy of repulsion is expressed as the unit kT , with k representing Boltzmann's constant ($1.381E - 23 \text{ J/K}$) and T representing the absolute temperature in Kelvin.



Graph 45 Particle–collector and particle–particle DLVO profiles in VEGAS water

It is important to observe that in VEGAS water the estimated profiles are attractive: in these conditions the particles are likely to form aggregates and to attach to the collector. The transport is expected to be extremely scarce in this case.

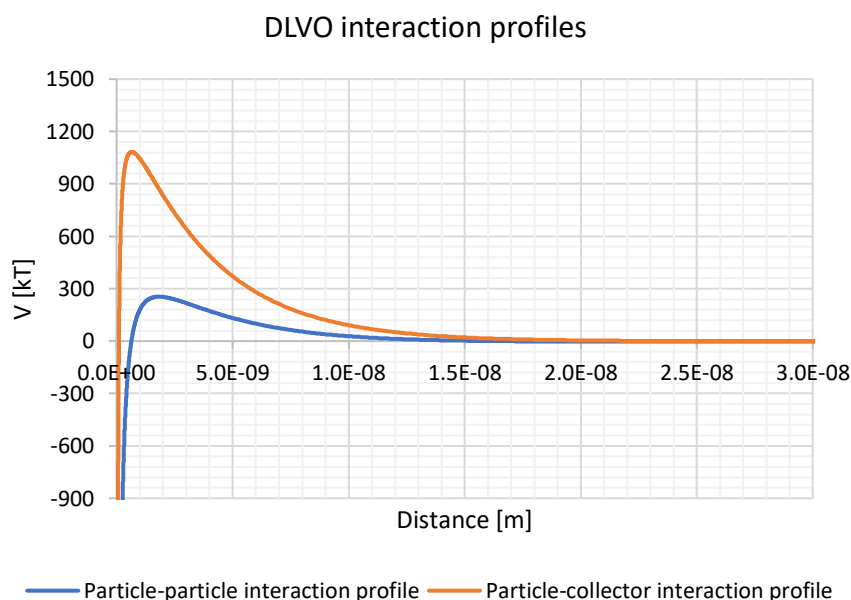
In several occasions however, also within the present thesis, the addition of CMC had favorable impacts on the colloidal stability of iron particles. For this reason, it is interesting to evaluate again the profiles, accounting now for the presence of the polymer.

The addition of 10 g/L CMC may also entail a change in ionic strength; in effect, the presence of a Na^+ ion in the sodium carboxymethyl cellulose molecule, together with an anionic chain, may have a certain influence. The calculations through Eq. 12 however demonstrate that the influence of CMC on IS is extremely low: its value practically does not change. The data used for the evaluation of DLVO profiles in CMC are reported below:

Table 19 Data for DLVO profile in a 10 g/L CMC solution

Ionic strength	Collector zeta potential - ZETASIZER	Particle zeta potential - SPECTROMETER
[mM]	[mV]	[mV]
7	-62.5	-57.5

Moreover, to account for the presence of the polymer adsorbed on the particle and sand surfaces, it is relevant to extend the DLVO theory including the steric interactions (see 3.3.3.4); in this case the default parameters of MNMs have been used. The results are displayed below.



Graph 46 Particle-collector and particle-particle DLVO profiles in CMC 10 g/L

Graph 46 demonstrates that the dissolution of the CMC determines more stable conditions for the iron colloids. In particular it is relevant to observe the high energetic barrier between sand grains and particles; a smaller barrier is also present between two particles: a fraction of colloids may have enough energy to overcome it and therefore form aggregates.

Overall, the addition of the polymer seems to strongly enhance the stability of NANOFE STAR colloidal systems, and these tests confirm this hypothesis. This situation was in effect observed throughout the experiments, in particular when evaluating the presence of ZVI inside the suspensions (ref. 5.1.1). In that occasion, the difference between the suspensions prepared in water and those prepared in CMC was evident; after ca. 10 hours from the mixing, the suspensions in water were completely sedimented, while those in CMC still looked darker for the presence of suspended iron particles. A photo showing this experimental evidence is reported in Figure 72.



Figure 72 Qualitative comparison between the suspensions prepared in water (the first three from the left) and those prepared in a certain concentration of CMC (the remaining five on the right)

NB: In both the previous cases, the magnetic interaction between particles were neglected. This contribution may actually be important, because the unmodified ZVI are known to be magnetic. However, the estimation of this phenomenon for NANOFE STAR particles requires specific parameters, not determined in this thesis.

5.5.2. Single-collector contact efficiency

MNMs allows the calculation of the single-collector contact efficiency η_0 , which quantifies the transport of the suspended particles to the collector surface. Depending on the attachment efficiency α then, the particles may or may not attach on the collector's surface.

It is worth reminding that the formulation of the single-collector contact efficiency is in many cases simply an approximation of the real situation. In effect it is based on the hypotheses that one particle does not perceive the presence of the others, the collision of particles occurs on an isolated collector and the deposition happens through mainly three independent mechanisms (see 3.3.2). In a real application, the lack of these conditions can have a strong influence on the deposition process.

The estimation of η_0 given by MNMs is presented below, using Yao's formulation.

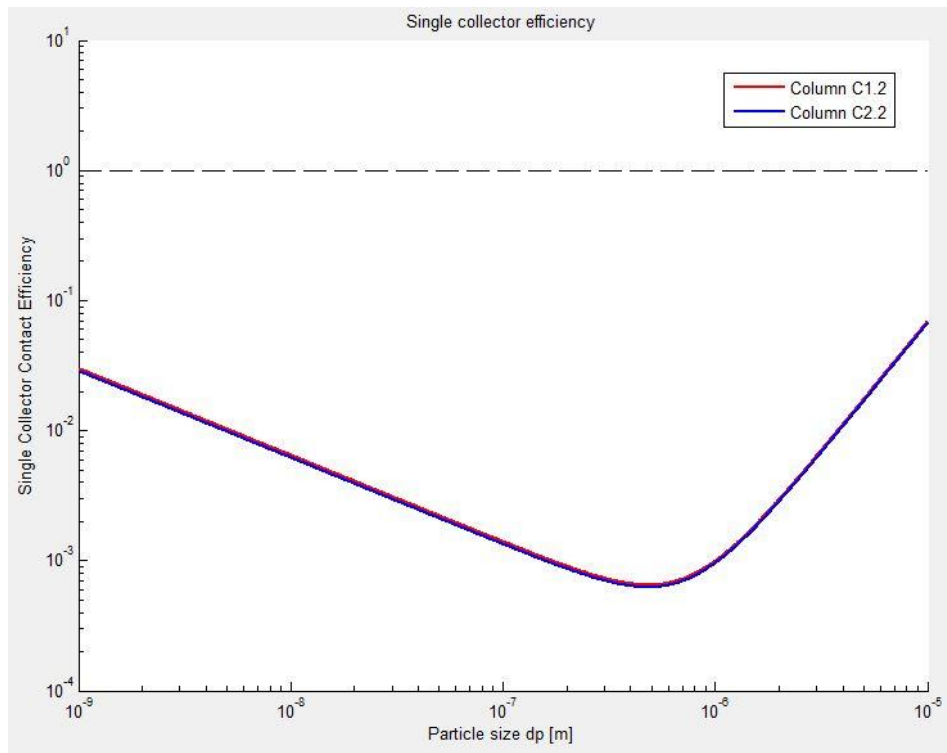


Figure 73 Evaluation of the single-collector contact efficiency, for both columns C1.2 and C2.2 (MNMs©, 2018)

According to the particle size characterization, the particle dimension is ca. $0.6 \mu m$; this means that the evaluated single-collector contact efficiency is about 0.067% for C1.2 and 0.065% for C2.2. The very low results depend largely on the quite high pore velocity used during the experiments.

These estimates of η_0 will be used in section 5.5.5 to simulate a radial injection.

5.5.3. Evaluation of tracer tests

As explained in 4.3.3.1, MNMs can be used to describe the motion of a solute inside a porous medium. A tracer is indeed a conservative solute, not subject to adsorption; hence, it is possible to evaluate a tracer test to obtain important parameters of a column, such as effective porosity and dispersivity.

A screenshot taken from the software is displayed below. It shows, with reference to column C2.2, that the analytical solution (blue curve) tries to fit the experimental data to provide the correspondent porous medium parameters. The output of the program is reported in Figure 75: the estimated parameters are given.

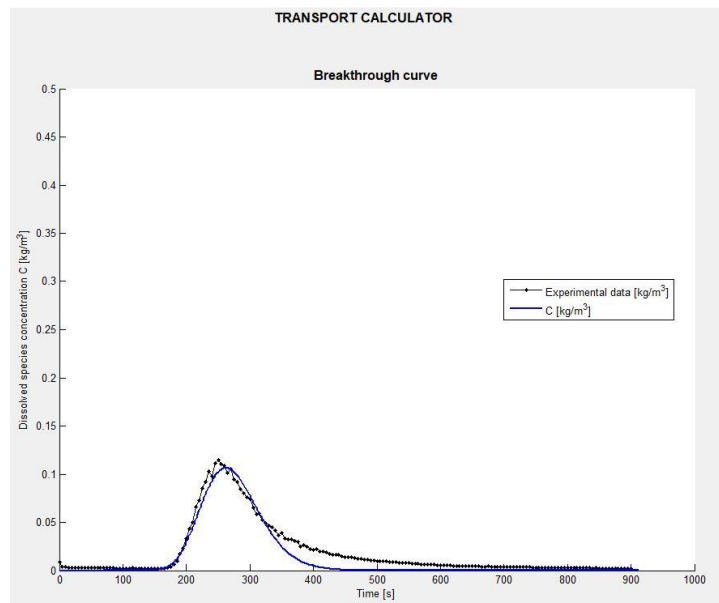


Figure 74 Tracer test evaluation, column C2.2 (MNM's©, 2018)

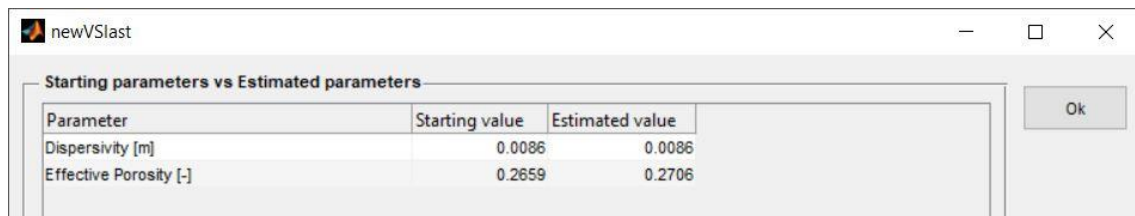


Figure 75 Output of the tracer test, column C2.2 (MNM's©, 2018)

Finally, all the parameters estimated through the software are compared below with the values calculated with the tracer tests. The results obtained are effectively comparable.

Table 20 Effective porosity and dispersivity evaluated with MNMs

Column ID	Sand	Effective Porosity (tracer test)	Dispersivity (tracer test)	Effective Porosity (MNM's)	Dispersivity (MNM's)
		ϵ [-]	α [m]	ϵ [-]	α [m]
C1.1	Dorsilit 8	0.395	1.33E-03	0.385	1.30E-03
C1.2	Dorsilit 8	0.404	9.44E-04	0.424	1.10E-03
C2.1	Vegas\Dorsilit	0.267	4.02E-03	0.285	4.90E-03
C2.2	Vegas\Dorsilit	0.264	7.40E-03	0.271	8.60E-03

5.5.4. Evaluation of NANOFER STAR tests

An important elaboration with MNMs was the evaluation of the column tests performed at VEGAS, with the objectives of understanding the attachment mechanisms of the NANOFER STAR particles on the porous media and quantifying these processes.

The simulation was started with the column C1.2, for which a more complete breakthrough curve was available. After having understood the main mechanisms occurring in this column, the same processes have been used to model the injection in the column C2.2. During the modeling, it was always important to match the experimental concentration profiles with the profiles estimated by MNMs.

In the following, the evaluations for the two columns are presented.

5.5.4.1. Column C1.2

All the experimental data collected during the experiment C1.2 have been used to model this injection through the software MNMs. As already said, the test consisted in the injection of 10 PVs of a 10 g/L suspension of NANOFER STAR particles, which nevertheless entered the column with a concentration of about 6.5 g/L. The carrier was CMC at 10 g/L.

The shape of the breakthrough curve, which smoothly reaches a plateau, suggested that one of the attachment mechanisms to include in the model was *blocking* (see 3.3.5); in effect, it seems like the deposition process slowly reaches saturation. In addition to blocking, the phenomenon of *linear attachment* has been included, also because the concentration profile data suggested the occurring of simple filtration.

The fitting of the experimental data with the MNMs model is shown below, both for the breakthrough curve and for the concentration profiles, which represent the moments after the particle injection and after the flushing.

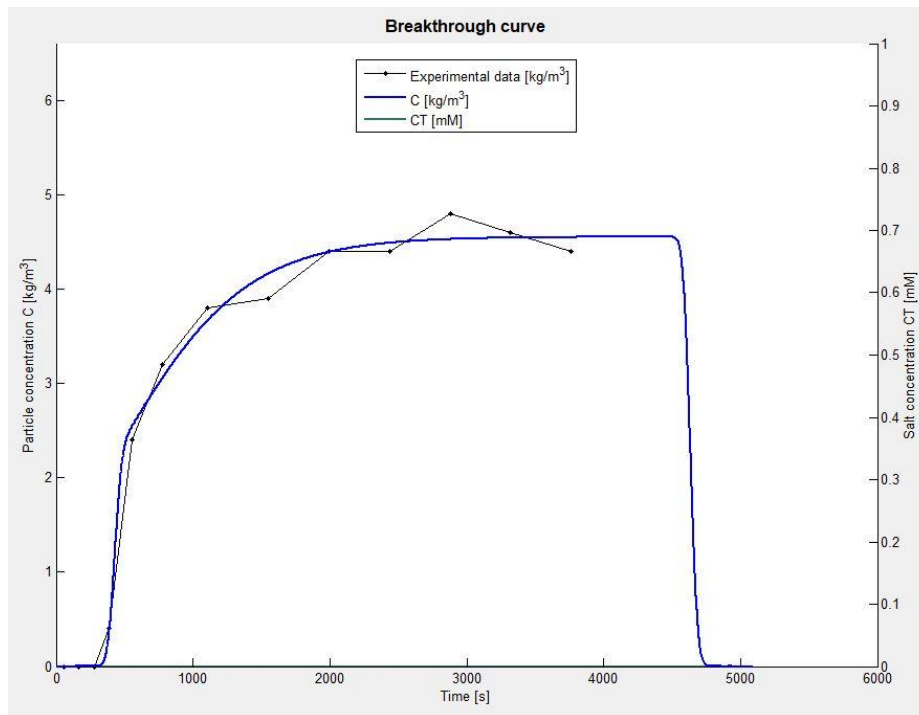


Figure 76 Fitting of breakthrough curve, column C1.2 (MNMs©, 2018)

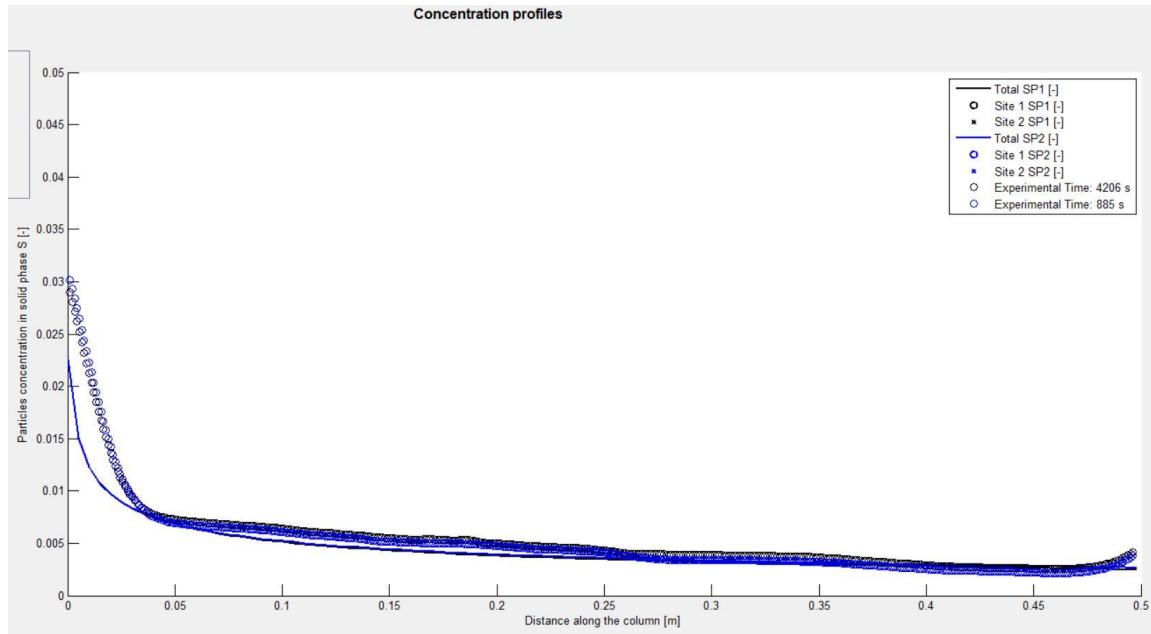


Figure 77 Fitting of concentration profiles, column C1.2 (MNM_s©, 2018)

Figure 76 and Figure 77 show the fitting between the experimental data and the MNMs model, described through the deposition mechanisms of blocking and linear attachment. It is important to notice that these mechanisms are considered irreversible: no detachment can occur. In effect the experimental profile of concentration after the flushing does not change much if compared with the one before the flushing. The software provided the coefficients that quantify these processes, based on the transport model. The output is reported below.

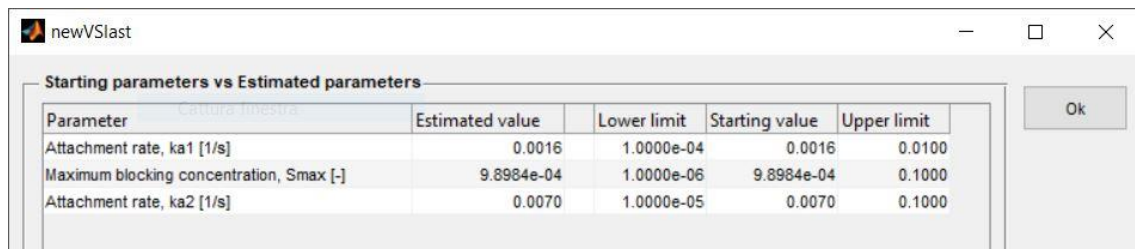


Figure 78 Estimated parameters via fitting, column C1.2 (MNM_s©, 2018)

These parameters will be used to simulate a field application in radial geometry in section 5.5.5.

5.5.4.2. Column C2.2

As already mentioned, the experiment with column C2.2 can be considered reliable just until the 5th pore volume: after this point a movement of the column occurred; therefore, this evaluation will consider the test until that moment.

The evaluation of the column C2.2 was attempted with the same deposition mechanisms chosen for C1.2. In effect the two porous media are quite similar: first of all, both are made of Dorsilit; then, the granulometric distributions are not that far. For these reasons it is probable that the deposition processes are similar to those previously observed.

The modeling of the injection in column C2.2 is reported in the following, showing both the fitting of the breakthrough curve and that of the concentration profiles.

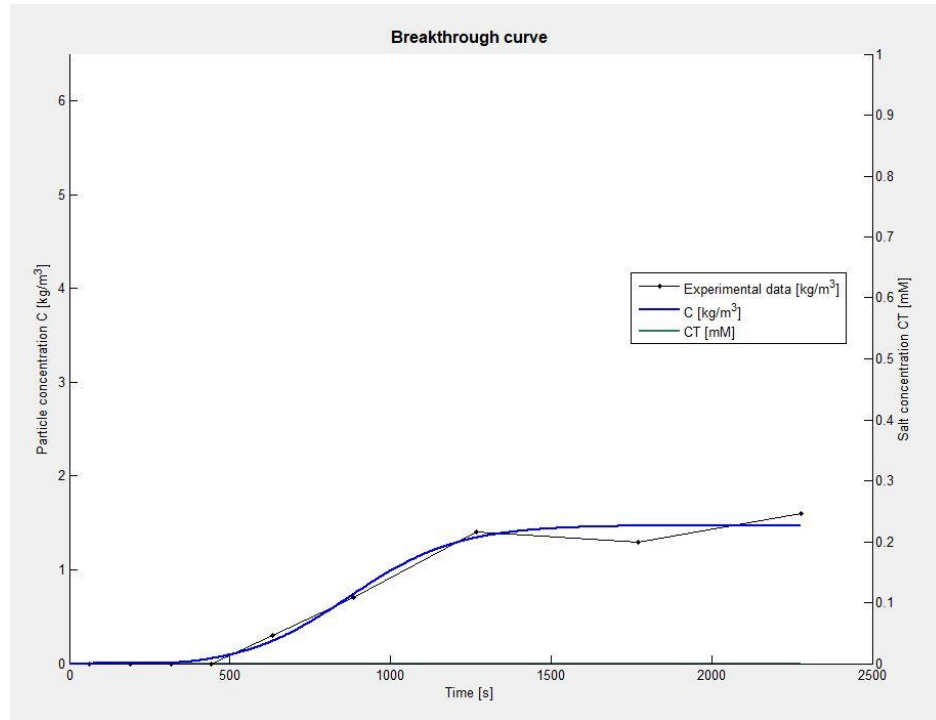


Figure 79 Fitting of breakthrough curve, column C2.2 (MNM's©, 2018)

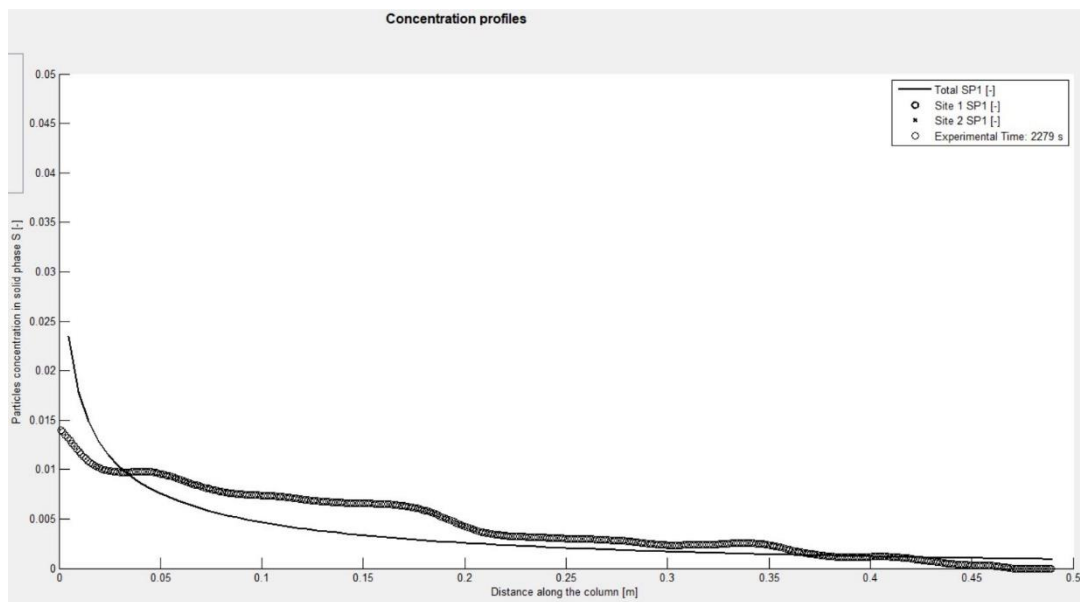
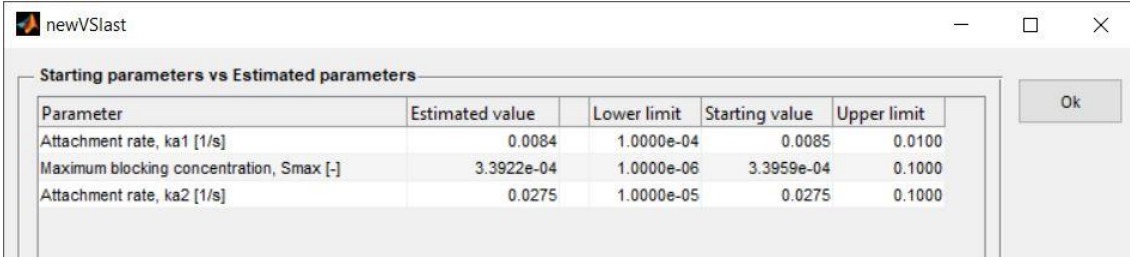


Figure 80 Fitting of concentration profiles, column C2.2 (MNM's©, 2018)

As demonstrated from the previous figures, the good fitting of the breakthrough curve is not matched by an equally good fitting of the concentration profile. However, the gap between experimental data and the curve given by the model is not generally excessive.

Once again, the estimated parameters of the model are reported below; they will be used for the simulation of a field application in section 5.5.5.



Parameter	Estimated value	Lower limit	Starting value	Upper limit
Attachment rate, k_{a1} [1/s]	0.0084	1.0000e-04	0.0085	0.0100
Maximum blocking concentration, S_{max} [-]	3.3922e-04	1.0000e-06	3.3959e-04	0.1000
Attachment rate, k_{a2} [1/s]	0.0275	1.0000e-05	0.0275	0.1000

Figure 81 Estimated parameters via fitting, column C2.2 (MNM_s©, 2018)

Comparing the parameters in Figure 81 with those in Figure 78, it is possible to make some considerations. First, it is worth noticing that in both the tests, the attachment rate of the blocking phenomenon is definitely smaller than the one regarding the linear attachment: the latter mechanism has a central role in the process of deposition of the particles in these two column tests. Next, both the k_a coefficients of the first test, resulted lower than the ones from the second test. In effect, considering the two breakthrough curves, it is apparent that in VEGAS sand the deposition mechanisms are much more intense than the ones occurring in Dorsilit 8, where a higher percentage of the inflowing iron mass managed to flow throughout the all column. Last, the maximum blocking concentration resulted of the same order of magnitude for the two evaluations, with a higher value for the Dorsilit 8 test: a greater concentration of particles could be deposited within this sand according to this deposition mechanism.

5.5.5. Simulation of field application in radial geometry

MNM_s allows the simulation of a field injection, to predict which outcome would occur if the previous conditions were applied in a real situation, supposing a radial symmetry domain. The model used by MNM_s is shown in Eq. 20, in which two attachment mechanisms have been chosen: the blocking phenomenon and the linear attachment, matching the ones identified during the evaluation of the column tests. The clogging of the porous medium, since it was not observed in the columns, will not be considered in these simulations. The modeling requires several parameters, most of them determined within this thesis; they are summarized in the following table.

Table 21 Estimated parameters, used for the radial injection simulation

Dorsilit 8 sand				VEGAS\Dorsilit sand			
single-collector contact efficiency	Attachment rate, site 1	Maximum blocking concentration	Attachment rate, site 2	single-collector contact efficiency	Attachment rate, site 1	Maximum blocking concentration	Attachment rate, site 2
η_0 [-]	$k_{a,1}$ [T^{-1}]	$S_{max,1}$ [-]	$k_{a,2}$ [T^{-1}]	η_0 [-]	$k_{a,1}$ [T^{-1}]	$S_{max,1}$ [-]	$k_{a,2}$ [T^{-1}]
0.067%	0.0016	9.90E-04	0.007	0.065%	0.0085	3.40E-04	0.0275

NB: site 1 refers to blocking phenomenon, site 2 to linear attachment.

Moreover, starting from the previous variables and using Eq. 22 and Eq. 23, the empirical parameters C_a and C_d (see 3.3.5) need to be calculated for at least one velocity and one attachment rate; they contain the influence of the phenomena not evaluated during the previous tests, like ionic strength, pH, etc. Knowing these coefficients, MNMs will calculate at every time step the correspondent k_a and k_d , for each velocity v , which is now changing hyperbolically with the distance from the point of injection.

In particular, however, in the previous evaluations the attachment was considered irreversible, so k_d and C_d are zero. The calculation that needs to be performed is the one for C_a ; the equation for the evaluation of this parameter (Eq. 22) is proposed again below. Each interaction mechanism has a different C_a , so this calculation has to be performed multiple times.

$$k_a = C_a \frac{\eta_0}{d_{50}} v \quad \text{Eq. 22}$$

The results of the different C_a , which represent the starting values set as parameters in the model, are shown in Table 22.

Table 22 Empirical coefficients C_a for both the kinds of sand

Dorsilit 8 sand		VEGAS\Dorsilit sand	
Coefficient C_a , site 1	Coefficient C_a , site 2	Coefficient C_a , site 1	Coefficient C_a , site 2
$C_{a,1}$ [-]	$C_{a,2}$ [-]	$C_{a,1}$ [-]	$C_{a,2}$ [-]
1.17	5.13	11.14	35.81

NB: site 1 refers to blocking phenomenon, site 2 to linear attachment.

In addition, the initial permeability of porous medium needs to be evaluated. Having measured the hydraulic conductivity, the permeability can be calculated as follows:

$$k = K \frac{\mu}{\rho g} \quad \text{Eq. 43}$$

where:

- k [L^2] is the permeability of the solid medium;
- K [$L T^{-1}$] is the hydraulic conductivity of the solid medium;
- μ [$M L^{-1} T^{-1}$] is the viscosity of the liquid fluid;
- ρ [$M L^{-3}$] is the density of the fluid
- g [$L T^{-2}$] is the gravitational acceleration.

The results are provided in the following table:

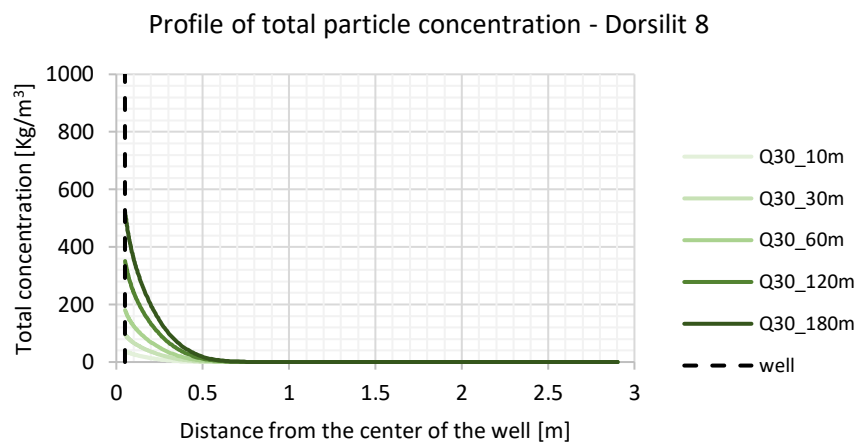
Table 23 Initial intrinsic permeabilities of the two kinds of sand

Dorsilit 8 sand	VEGAS\Dorsilit sand
k [m^2]	k [m^2]
8.27E-10	5.72E-10

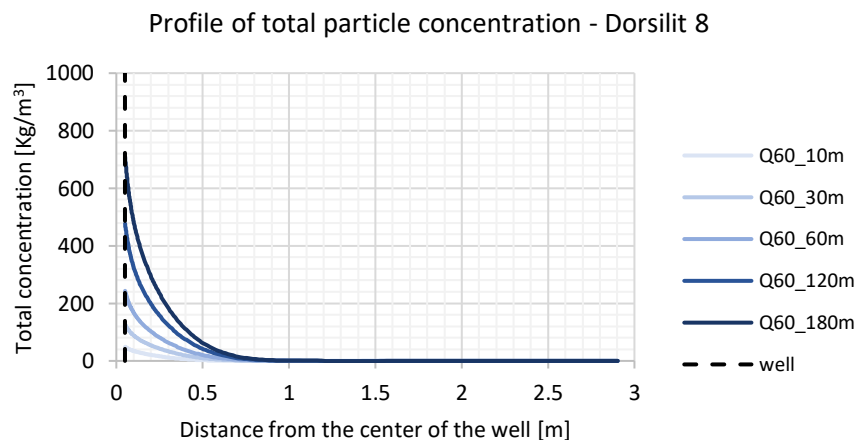
Finally, some geometric parameters have to be selected: the radius of the injection well is considered 0.05 m , while the simulation is evaluated for a radial domain of three meters.

With the previous parameters, the injection of 6.5 g/L NANOFER STAR suspension in 10 g/L CMC is simulated for the two porous media, with different discharge rates (30 , 60 and 120 L/min) and at different times. The discharge rates have been chosen to reproduce real applications. The results are presented after 10 , 30 , 60 , 120 and 180 minutes from the beginning of the injection, in order to understand the evolution of the conditions over time. The spatial distributions of the deposited iron evaluated through the simulation are reported below, divided between Dorsilit 8 sand and VEGAS\Dorsilit sand.

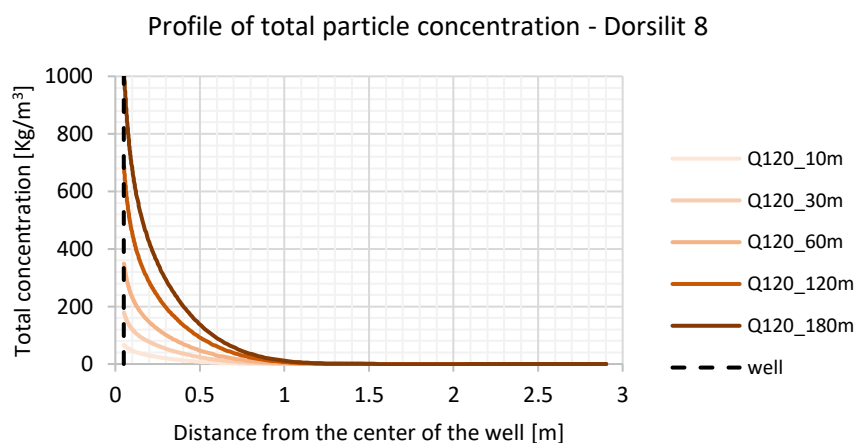
Dorsilit 8 sand:



Graph 47 Profile of total particle concentration after 10, 30, 60, 120 and 180 minutes of injection; NANOFER STAR concentration 6.5 g/L , CMC concentration 10 g/L , flow rate 30 L/min , Dorsilit 8 sand

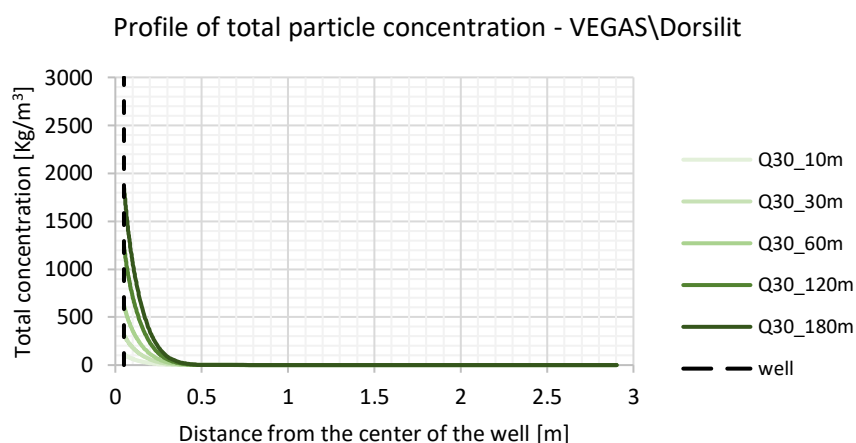


Graph 48 Profile of total particle concentration after 10, 30, 60, 120 and 180 minutes of injection; NANOFER STAR concentration 6.5 g/L , CMC concentration 10 g/L , flow rate 60 L/min , Dorsilit 8 sand

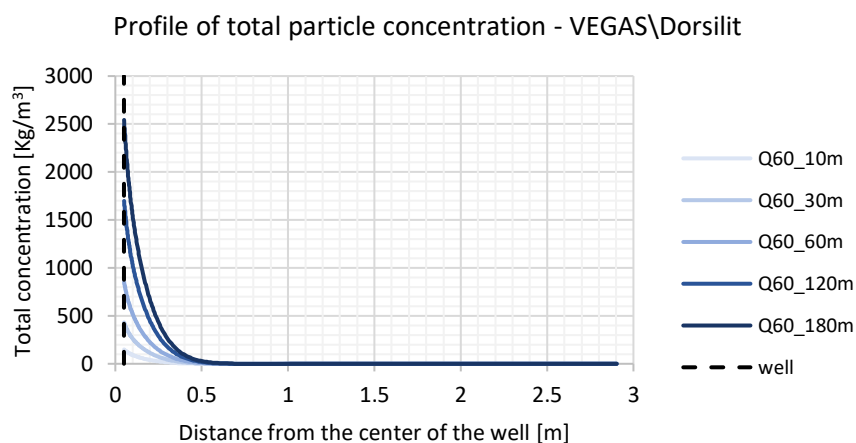


Graph 49 Profile of total particle concentration after 10, 30, 60, 120 and 180 minutes of injection; NANOFER STAR concentration 6.5 g/L, CMC concentration 10 g/L, flow rate 120 L/min, Dorsilit 8 sand

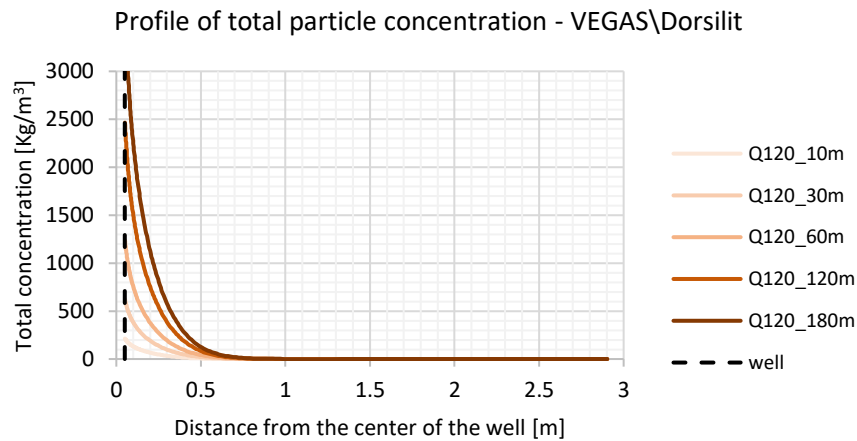
VEGAS\Dorsilit sand:



Graph 50 Profile of total particle concentration after 10, 30, 60, 120 and 180 minutes of injection; NANOFER STAR concentration 6.5 g/L, CMC concentration 10 g/L, flow rate 30 L/min, VEGAS sand

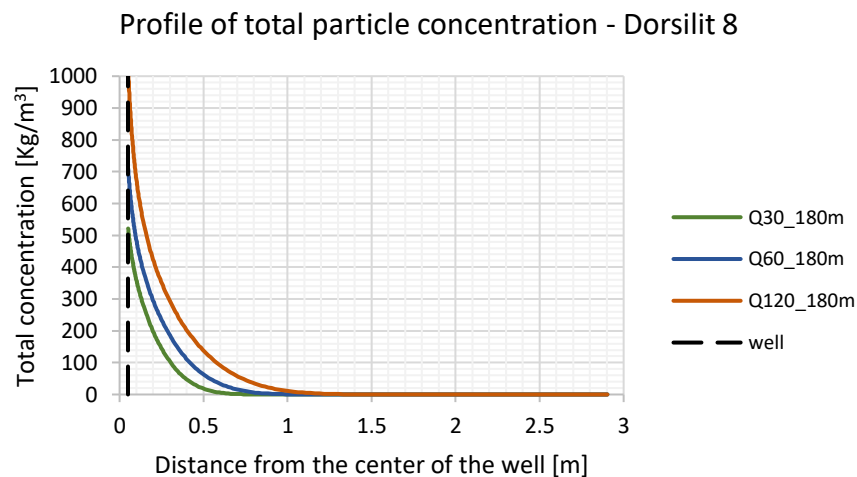


Graph 51 Profile of total particle concentration after 10, 30, 60, 120 and 180 minutes of injection; NANOFER STAR concentration 6.5 g/L, CMC concentration 10 g/L, flow rate 60 L/min, VEGAS sand



Graph 52 Profile of total particle concentration after 10, 30, 60, 120 and 180 minutes of injection; NANOFER STAR concentration 6.5 g/L, CMC concentration 10 g/L, flow rate 120 L/min, VEGAS sand

The previous graphs show the spatial distribution of particles reached via simulated injections. It is relevant to notice that a higher discharge rate causes the particles to travel greater distances, because the velocity of the carrier fluid is higher. This consideration is well-explained by Graph 53, which compares the final distributions (after three hours of injection) obtained with the three flow rates (30, 60, 120 L/min) in Dorsilit 8 sand.



Graph 53 Comparison of the three final iron distributions obtained with the injection of 6.5 g/L of NANOFER STAR particles suspended in 10 g/L of CMC for 180 minutes, at different flow rates (30, 60, 120 L/min); Dorsilit 8 sand

However, when the flow rate of injection increases, also the pressure buildup increases and may cause soil fracturing. This fact is demonstrated by the following two figures, showing the pressure variation over time caused by the injections at 30 and 120 L/min in Dorsilit 8 sand. In the modeling the pressure variation is simulated as a drop at 0.5, 1 and 3 meters from the center of the injection well.

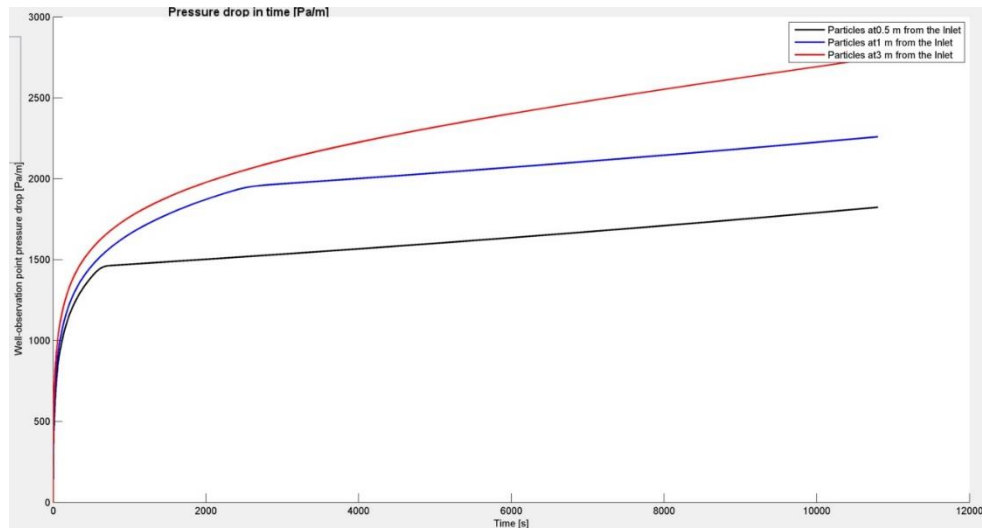


Figure 82 Simulated pressure drop at 0.5, 1 and 3 meters from the center of the well during the injection of 6.5 g/L of NANO FER STAR and 10 g/L CMC in Dorsilit 8 sand with flow rate equals to 30 L/min (refer to Graph 47) (MNM's©, 2018)

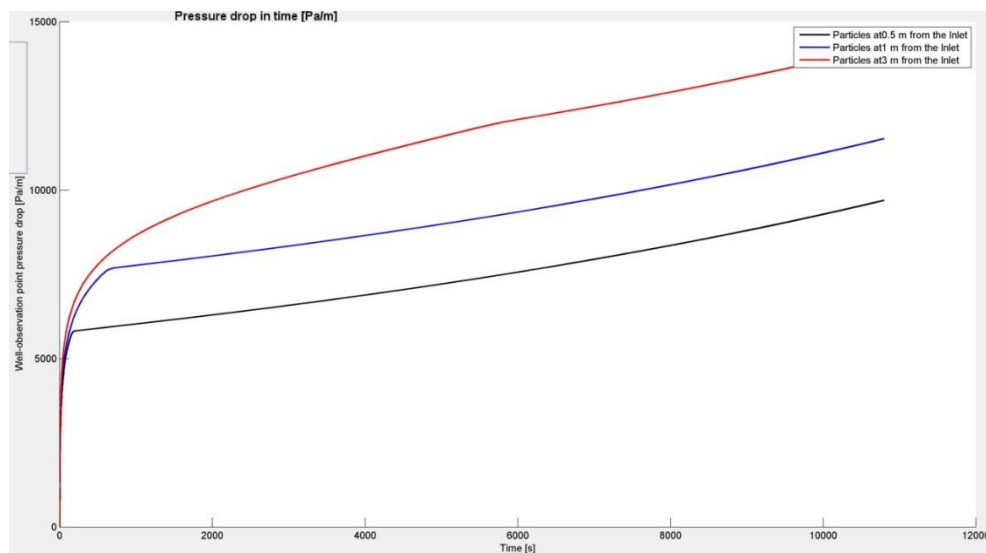
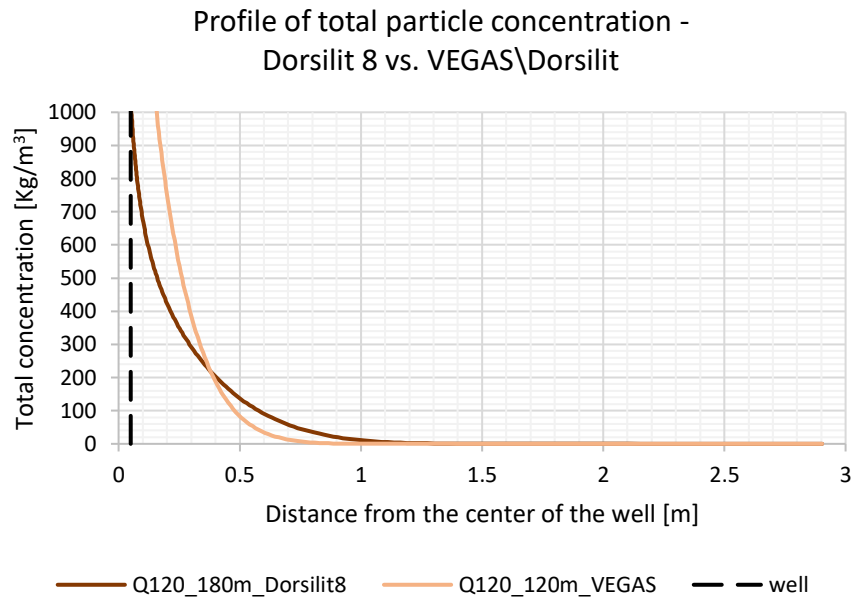


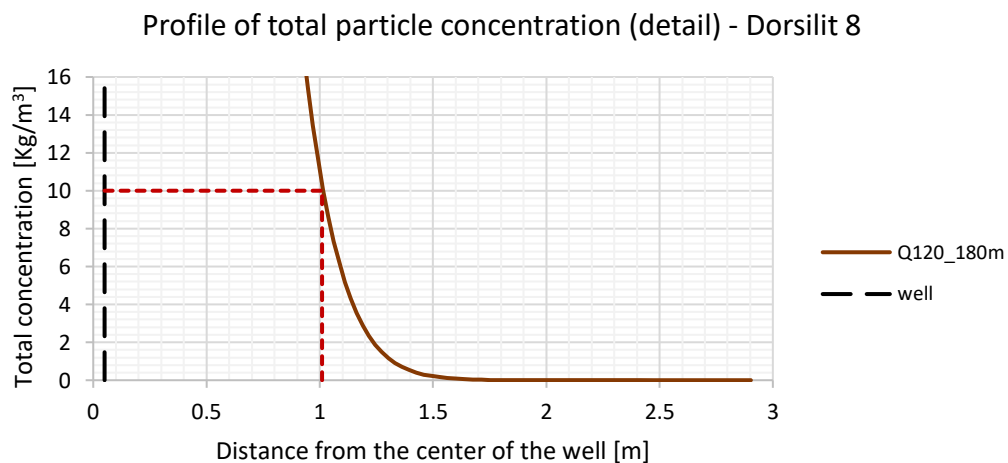
Figure 83 Simulated pressure drop at 0.5, 1 and 3 meters from the center of the well during the injection of 6.5 g/L of NANO FER STAR and 10 g/L CMC in Dorsilit 8 sand with flow rate equals to 120 L/min (refer to Graph 49) (MNM's©, 2018)

It is also possible to make a comparison between the two porous media. In this case it is obvious that the iron distributions obtained through the simulations are quite poor, with the one for the heterogeneous medium (VEGAS sand) even worse than the other. The graph comparing the two different sands is reported below, displaying only the results achieved simulating the injection with a flow rate of 120 L/min, after three hours of simulation.

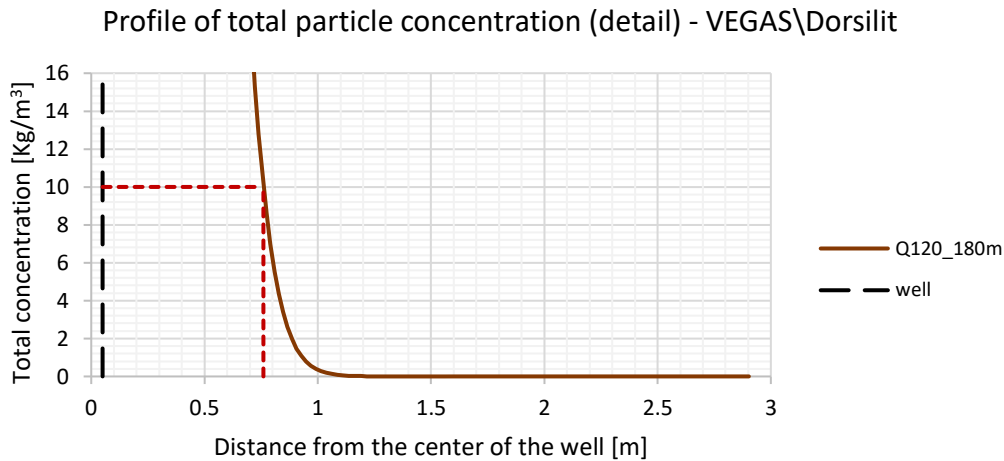


Graph 54 Simulation of iron distributions in the two porous media. NANOFE STAR 6.5 g/L in CMC 10 g/L, flow rate 120 L/min, Dorsilit 8 and VEGAS sands

Focusing the attention on the iron spatial distribution, it is relevant to point out that the previous simulations do not provide completely satisfactory results, especially for VEGAS sand. If a concentration of 10 g/L (or 10 Kg/m³) is established as the target iron concentration for the remediation of a contaminated area, it is possible to observe that only within a distance of 0.95 m (for Dorsilit 8 sand) and 0.71 m (for VEGAS sand) from the well this value is reached, with a flow rate of 120 L/min. The following graphs demonstrate in detail what just mentioned.



Graph 55 Distance reached by a hypothetical ZVI target concentration of 10 g/L after 180 minutes of injection; NANOFE STAR 6.5 g/L, CMC concentration 10 g/L, flow rate 120 L/min, Dorsilit 8 sand. Detail of Graph 49



Graph 56 Distance reached by a hypothetical ZVI target concentration of 10 g/L after 180 minutes of injection; NANOFE STAR 6.5 g/L, CMC concentration 10 g/L, flow rate 120 L/min, VEGAS sand. Detail of Graph 52

Since the previous distributions do not seem satisfactory, an improvement of the NANOFE STAR particle mobility is now sought via modeling. Previous experiments show that the stability of the suspensions and the particle transport are strongly influenced by the addition of CMC. For this reason, a considerably higher CMC concentration is simulated: 40 g/L. This value of CMC also modifies the rheological behavior of the suspensions because an evident shear-thinning comportment is now exhibited. This specific concentration was chosen because the parameters of the Cross model describing the rheological properties of this fluid had been measured at Politecnico di Torino with a rheometer (Anton Paar Physica MCR 301).

Table 24 Parameters of the Cross model for the 40 g/L CMC solution

Parameter		Value	U.M.
Zero-shear Newtonian plateau viscosity	μ_0	0.1626	[Pa·s]
High-shear Newtonian plateau viscosity	μ_∞	0.001	[Pa·s]
Cross time constant	ϑ	0.00025	[s]
Cross rate constant	χ	0.75	[-]

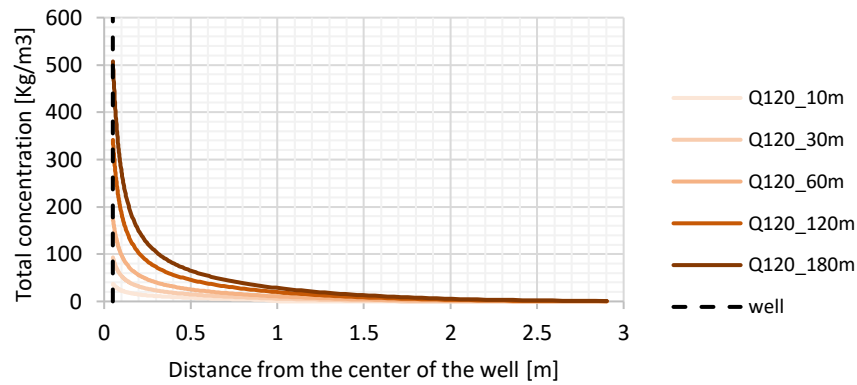
The equation describing the Cross model is proposed again:

$$\mu_m = \mu_\infty + \frac{\mu_0 - \mu_\infty}{1 + (\vartheta \dot{\gamma})^\chi} \quad \text{Eq. 35}$$

The modeling was repeated, to see if the increase in CMC concentration would have a positive effect on the transport of NANOFE STAR particles. All the other parameters, apart from those concerning the polymer, have been supposed constant. Even the initial values of C_a , considering the utilization of the same CMC just at higher concentration, have been considered unchanged. The results obtained are reported below, focusing the attention on the discharge rate of 120 L/min to directly compare it to the previous findings. The results are divided for the two porous media; later a comparison with the previous conditions is provided.

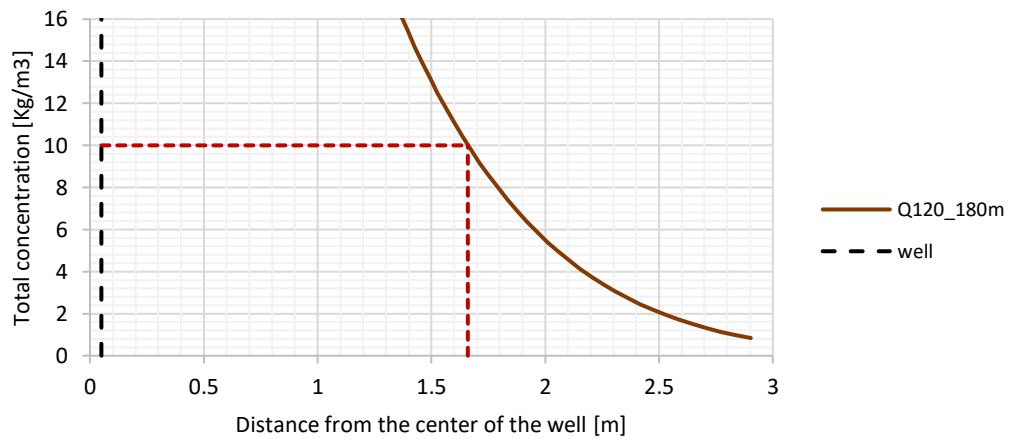
Dorsilit 8 sand:

Profile of total particle concentration - Dorsilit 8



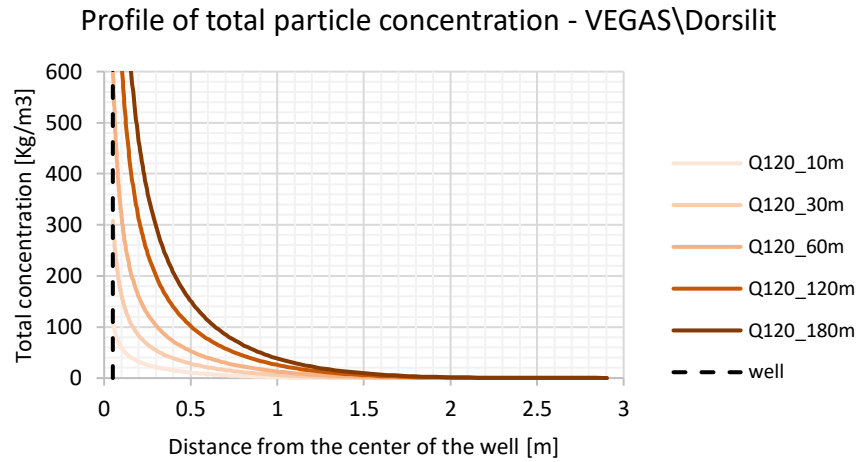
Graph 57 Profile of total particle concentration after 10, 30, 60, 120 and 180 minutes of injection; NANOFER STAR concentration 6.5 g/L, CMC concentration 40 g/L, flow rate 120 L/min, Dorsilit 8 sand

Profile of total particle concentration (detail) - Dorsilit 8

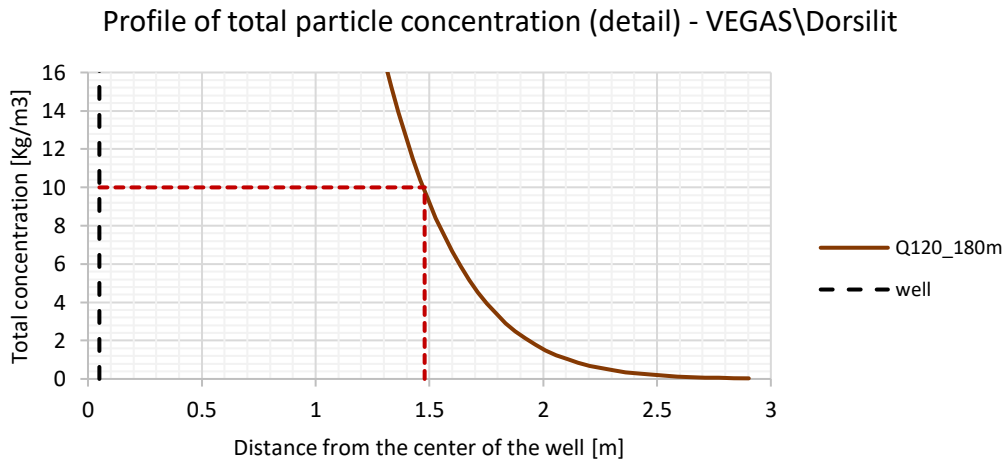


Graph 58 Distance reached by a hypothetical ZVI target concentration of 10 g/L after 180 minutes of injection; NANOFER STAR 6.5 g/L, CMC concentration 10 g/L, flow rate 120 L/min, Dorsilit 8 sand. Detail of Graph 57

VEGAS\Dorsilit sand:



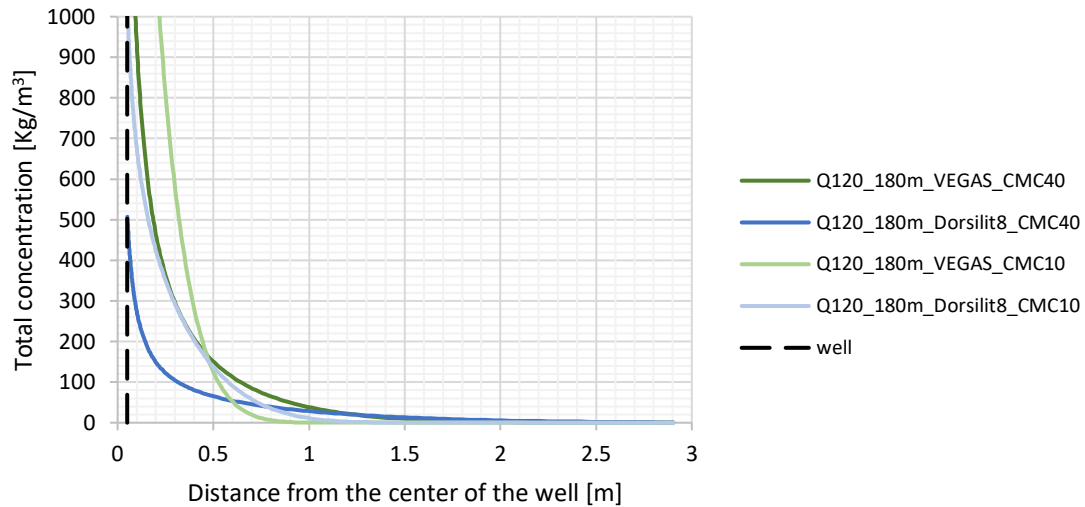
Graph 59 Profile of total particle concentration after 10, 30, 60, 120 and 180 minutes of injection; NANOFER STAR concentration 6.5 g/L, CMC concentration 40 g/L, flow rate 120 L/min, VEGAS sand



Graph 60 Distance reached by a hypothetical ZVI target concentration of 10 g/L after 180 minutes of injection; NANOFER STAR 6.5 g/L, CMC concentration 40 g/L, flow rate 120 L/min, VEGAS sand. Detail of Graph 59

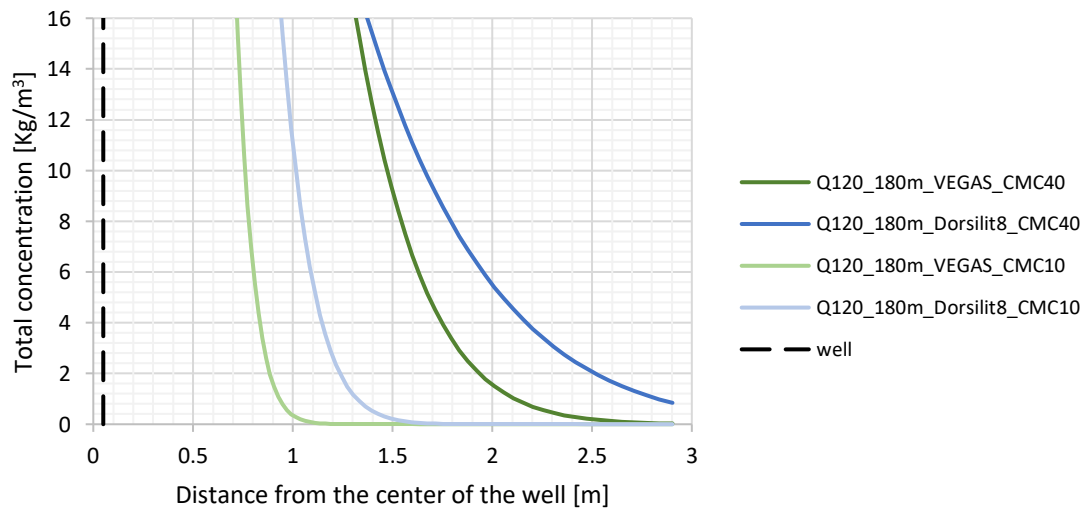
Comparison between the porous media and the two CMC concentrations:

Profile of total particle concentration -
Dorsilit 8 vs. VEGAS\Dorsilit



Graph 61 Comparison between the iron distributions in the two porous media with different CMC concentrations (10 g/L and 40 g/L) after 180 minutes of injection; NANOFE STAR 6.5 g/L, flow rate 120 L/min

Profile of total particle concentration (detail) -
Dorsilit 8 vs. VEGAS\Dorsilit



Graph 62 Comparison between the iron distributions in the two porous media with different CMC concentrations (10 g/L and 40 g/L) after 180 minutes of injection; NANOFE STAR 6.5 g/L, flow rate 120 L/min. Detail of Graph 61

From Graph 58 and Graph 60 it is possible to observe that now the target concentration of iron (10 g/L) is guaranteed for ca. 1.61 m and 1.43 m around the well, respectively for the Dorsilit 8 and the VEGAS sand; the creation of an iron suspension in a CMC solution with higher concentration seems to considerably improve the transport of the NANO FER STAR particles, as demonstrated by Graph 61 and Graph 62. The addition of CMC causes the viscosity to be generally higher than before, for this reason it is also important to check the pressure variation due to the injection. To easily compare the results with Figure 83, the simulation of the pressure drop will focus on the injection of the suspension (6.5 g/L NANO FER STAR in 40 g/L CMC) in the Dorsilit 8 sand, with a flow rate of 120 L/min . The results are shown below, in Figure 84.

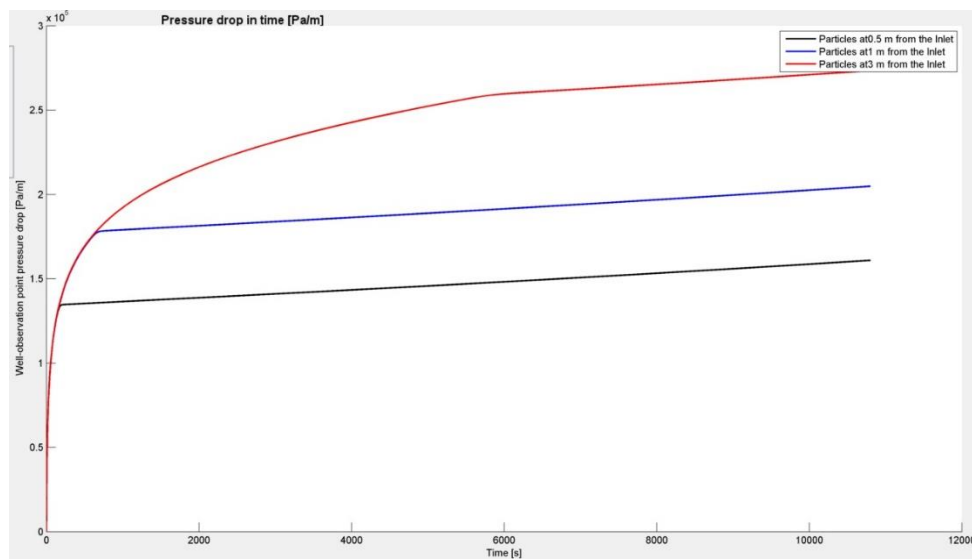


Figure 84 Simulated pressure drop at 0.5, 1 and 3 meters from the center of the well during the injection of 6.5 g/L of NANO FER STAR and 40 g/L CMC in Dorsilit 8 sand with flow rate equals to 120 L/min (refer to Graph 57) (MNM's©, 2018)

In this case the variation of the pressures is considerably higher than before, because of the much higher viscosity of the fluid; however, the shear-thinning behavior of the carrier now plays an important role in maintaining moderate the variation of pressures due to the injection: at high shear rates, near to the injection point, the viscosity of the fluid decreases, hence the pressure does not increase excessively. The viscosity profile around the well is also calculated by MNMs using the coefficients of the Cross model; its representation is shown in Figure 85. This characteristic of the carriers is extremely important and must be exploited during field applications. Nevertheless, further experimental tests should be performed with higher CMC concentrations to validate the results obtained through the previous simulations.

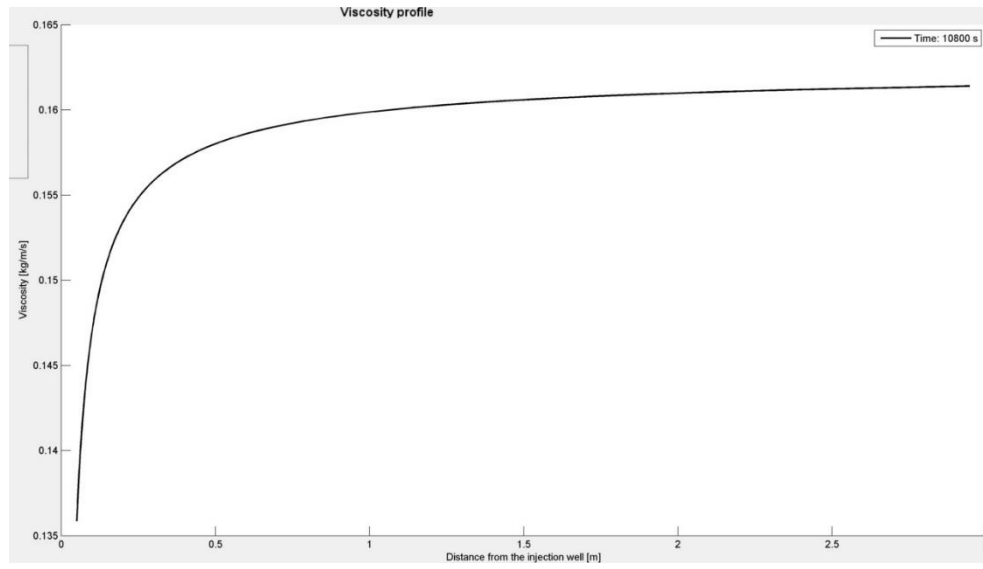


Figure 85 Viscosity profile around the well, after 180 minutes of injection; NANOFE STAR concentration 6.5 g/L, CMC concentration 40 g/L, flow rate 120 L/min, Dorsilit 8 sand (MNM©, 2018)

6. Conclusions

With the objective of identifying a combination of NANOFER STAR nZVI particles and CMC (*Walocel CRT 30 GA*) that could be successfully used in a field application, different laboratory tests have been performed within this thesis. An important part of the experimental work focused on the determination of the iron suspension properties, of the characteristics of two different porous media and of the rheological behavior of the carrier solutions. Afterwards, a selected combination of particles and CMC was used to conduct column tests, with the objective of understanding the attachment mechanisms of the particles onto the sand grains and obtaining fundamental parameters that regulate these processes. These parameters, together with many others determined during the experimental work, have been used to simulate a field, radial injection through the software MNMs.

In the present section the major findings of this thesis are summarized; for the sake of clarity, the results will be gathered into different parts, which correspond to the paragraphs of the chapter *Results and discussion*. At the end, some general conclusions are made.

Particle and suspension characterization

The analysis of the ZVI content in the suspensions prepared with NANOFER STAR particles (5, 8 and 10 g/L) and a certain concentration of CMC (0, 5, 8 and 10 g/L) revealed that only the 62% circa of the total iron is actually Fe⁰. During the process of activation of the powder, the initial 77% of Fe⁰ claimed by the producer is probably partly corroded into iron oxides. However, it has been demonstrated that this percentage of zerovalent iron does not significantly decrease over time: conserved in glass, airtight bottles at room temperature, it stayed quite constant for a month.

The sedimentation tests performed at Politecnico di Torino showed that the higher the concentration of iron in a suspension, the faster the particles will settle. In fact, in higher concentrations the particles are more likely to form bigger aggregates and later sediment faster, according to Stokes' law. This test has been carried out for four different NANOFER STAR concentrations (2.5, 6.5, 10 and 20 g/L) in a 10 g/L solution of CMC.

Moreover, the comparison of the tests with hot and cooled samples showed that the viscosity decrement of the suspensions due to high temperatures entails a faster sedimentation of the iron particles. This experimental observation is again in accordance with Stokes' law.

The evaluation of the particle size distribution has been performed on several combinations of NANOFER STAR particles and CMC, both at VEGAS and at Politecnico di Torino. During the evaluation of the results, it was fundamental to understand that some of the data from the acoustic spectrometer were affected by errors, caused by two reasons. First of all, the measured concentrations were very close to the inferior accuracy threshold of the instrument, and sometimes even lower. Secondly, the detection of microscopic air bubbles inside the samples misled the readings of the instrument. This last finding was evidenced by comparing the spectrometer results to those of the disc centrifuge. However, after some adjustments, the data from the two devices resulted consistent. It would be advisable, the next time the spectrometer

is used, to adopt some measures for the removal of the trapped air from the samples (e.g. using a vacuum pump).

The final data showed that the iron mass has a narrow size distribution, centered around a peak value that is increasing with increasing concentrations of iron. The suspension of NANOFER STAR 10 g/L in CMC 10 g/L, chosen for the column injections, registered a peak at about 500 – 600 nm. Another fraction of particle having a much smaller size (40 – 50 nm) has been detected by the centrifuge and sometimes by the acoustic spectrometer. However, as the centrifuge results demonstrate, this fraction does not account at all in terms of iron mass, but it is relevant only in terms of number of particles.

The zeta potential results demonstrated the role of the CMC in the colloidal stability of iron particles. It has been proved that NANOFER STAR particles simply dispersed in water have a value of zeta potential close to zero: there are no repulsive forces between them and they are likely to form aggregates and settle. The addition of CMC into the suspensions provided much higher (in absolute value) values of zeta potential (-57.5 mV for a 10 g/L NANOFER STAR suspension in 10 g/L CMC), meaning that the repulsive forces are now relevant and an energy barrier hindering particle aggregation is formed.

No significant variations of zeta potential with the particle concentration have been registered, stressing the fact that it is a property of the single particle.

Properties of CMC solutions

At first, the rheological properties of water and of three CMC solutions (5, 8 and 10 g/L) have been investigated with a viscometer. The addition of the polymer increased considerably the viscosity of the solutions, which in turn, according to Stokes' law, should have resulted in an increase of the stability of the colloids dispersed in that fluid.

The fluids exhibited a Newtonian behavior in the range of shear rates of the analysis.

The rheological behavior of the same solutions when injected in the porous medium has been studied also through CMC column tests, showing a good agreement with bulk rheological measurements.

Ultimately, up to 10 g/L the CMC in use does not display a shear-thinning behavior; however, when reaching 40 g/L, it behaves as a shear-thinning fluid, which can be described using the Cross rheological model.

NANOFER STAR column tests

The injection of NANOFER STAR in columns packed with two different porous media gave different results. The test performed with Dorsilit 8 sand (column C1.2) showed a rather high breakthrough curve that reached 65% circa of the iron at the inlet. The distribution of the iron inside the column was quite poor because the major part was concentrated only in the first 5 cm. In the rest of the column the iron did not attach much: probably only the bigger aggregates were deposited at the beginning of the column, while most of the rest traveled until the outflow. On the other hand, the test with VEGAS\Dorsilit sand (column C2.2) had a much lower breakthrough curve (22%) and a better distribution of the iron inside the column. The

heterogeneous medium with a finer fraction may have caused a greater deposition of the iron in this case.

Pressures measurements demonstrated that the clogging of the porous medium did not occur during the tests.

The final flushing of the two columns proved that the detachment of the particles was minimum, and the pressures almost had a complete recovery, especially for C2.2.

The hydraulic conductivity tests performed before and after the injection of particles revealed a change in the flow conditions, which resulted slightly worsened after the experiments (ref. Table 15 and Table 17) .

Modeling with MNMs

The software MNMs has been used to further investigate some aspects of the previous tests and to simulate a field application.

The DLVO profiles drawn by MNMs demonstrated the role of the CMC in increasing the repulsive forces among colloidal particles and between particles and collector. In VEGAS water the energy profiles were attractive (ref. Graph 45), hence the colloids were likely to aggregate in clusters and then to deposit. In a 10 g/L solution of CMC instead, the profiles showed the presence of an energy barrier (higher for the particle–collector interactions, lower for the particle–particle ones; see Graph 46), which causes repulsion among particles and with the collector, impeding both aggregation and deposition phenomena.

The column tests with iron particles have been modeled via MNMs. This allowed the determination of the deposition mechanisms occurring inside the columns during the tests and the estimation of the parameters which regulate them. The blocking phenomenon and the linear attachment seem to provide a good description of the deposition process in both the sands, with the latter mechanism having a greater relevance than the former (as demonstrated by the comparison of the k_a coefficients, ref. Table 21); since both the sands are composed of Dorsilit, it was expected that similar deposition phenomena occurred. Moreover, the attachment rates concerning the VEGAS porous medium had higher values than those of Dorsilit 8 sand; this is in accordance with the experimental breakthrough curves obtained from the column tests.

The estimation of the k_a coefficients allowed the determination of the parameters C_a , required by the software to simulate injections in a radial domain.

The radial simulations of an injection of 6.5 g/L NANOFE STAR dispersed in 10 g/L CMC resulted in poor outcomes for both the sands. In particular, focusing on the iron distribution around the injection well and supposing a target concentration of deposited iron of 10 g/L, it is possible to observe that this value is guaranteed for less than one meter around the well in both the porous media, even injecting with a quite high flow rate 120 L/min. Via modeling, an improvement of the conditions is sought through the addition of a considerably higher quantity of CMC in the suspensions, reaching a concentration of 40 g/L, which possesses a higher viscosity and presents shear-thinning behavior.

The new radial simulations provided much better results, estimating that now the target concentration may reach or even pass a distance of ca. 1.5 m from the well in both the porous media. With these values it is possible to start thinking of a real field application; however,

further experimental tests need to be conducted on this higher CMC concentrations, also evaluating the pressure drops that arise when injecting a more viscous fluid. In effect, a decisive increase in the pressure drop has been estimated by MNMs when simulating the injection of 40 g/L CMC in Dorsilit 8 sand (ref. Figure 84); the carrier shear-thinning behavior however, may play a fundamental role in keeping moderate the pressure variations in the proximity of the injection well: this advantageous property needs to be further investigated and then exploited.

In general, studying the characteristics of the iron suspensions, some critical aspects for the application of the nanoremediation technology emerged. Specifically, the sedimentation tests demonstrated that a higher NANOFE STAR concentration in the suspensions causes a faster sedimentation of the particles. Moreover, PSD results showed that the iron particles, when dispersed in higher concentrations, form bigger aggregates, which are more likely to sediment out of the suspension or to be filtrated by the porous medium. These two experimental evidences can pose some difficulties in the choice of the suitable concentration for a field application; a compromise between the stability of the suspensions and the volumes required to reach the desired concentration of iron in the soil must be found.

In addition, the stabilizing role of the CMC towards the NANOFE STAR particles has been proved fundamental by the zeta potential results and by the simple experimental observation (ref. Figure 72): its use seems therefore essential for a successful field application. However, some drawbacks have arisen during the experiments and the simulations performed in this thesis. The main concern regards the strong increase in the pressures caused by the injection of a viscous fluid, which may lead to fracturing of the soil. On the other hand, a positive property of the concentrated CMC solutions seems to be able to mitigate the pressure buildup in the porous medium: the shear-thinning behavior exhibited by the 40 g/L CMC solution during the radial injection simulation contributed to not rise excessively the pressures in that test.

In effect, an important role for the success of this remediation technique seems to be played by the carrier fluid. It would be relevant to study more in detail the rheological behavior of different CMC solutions with concentrations in the range 10 g/L and 40 g/L, used in this thesis. In this way, it would be possible to assess the transition between Newtonian and shear-thinning behavior of the fluid. Moreover, it would be interesting to study how, with increasing CMC concentrations, the pressures in the porous medium would reflect the opposing contributions of an increased viscosity and of an intensified the shear-thinning behavior.

Further investigations should also focus on suspension properties. In fact, during the determination of particle size, it was noticed that the NANOFE STAR particles, which according to the producer have a nominal dimension of 50 nm, have much larger dimensions when dispersed in a suspension (600 nm ca.) Finding a way of preventing the iron particles from creating aggregates when dispersed in water is a crucial point of the technology, and can be achieved both by the designing new and improved iron particles or by finding new strategies of enhancing the repulsive forces among the ones already available. Also the activation process may influence this aspect, therefore it could be useful to test different procedures.

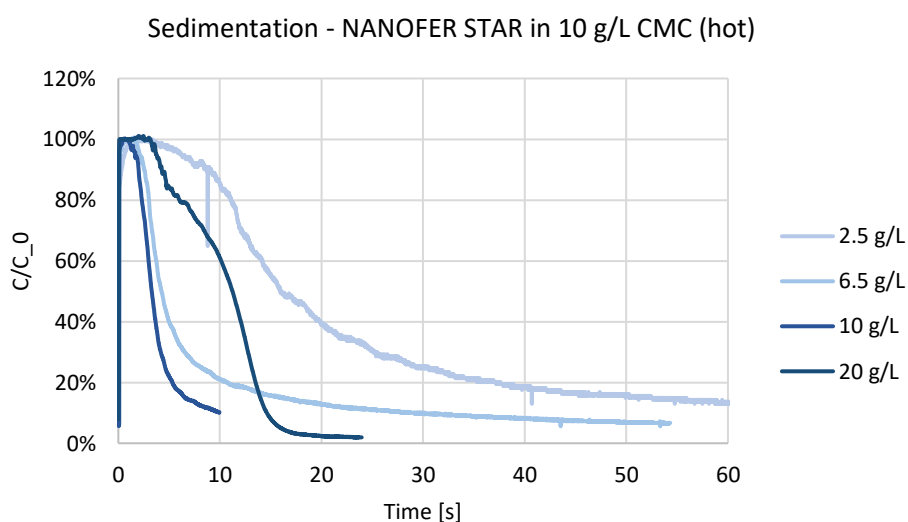
Appendix A

Other results

Particle and suspension characterization

Sedimentation tests

Another sedimentation test has been performed at higher temperatures (immediately after the preparation of the suspensions):



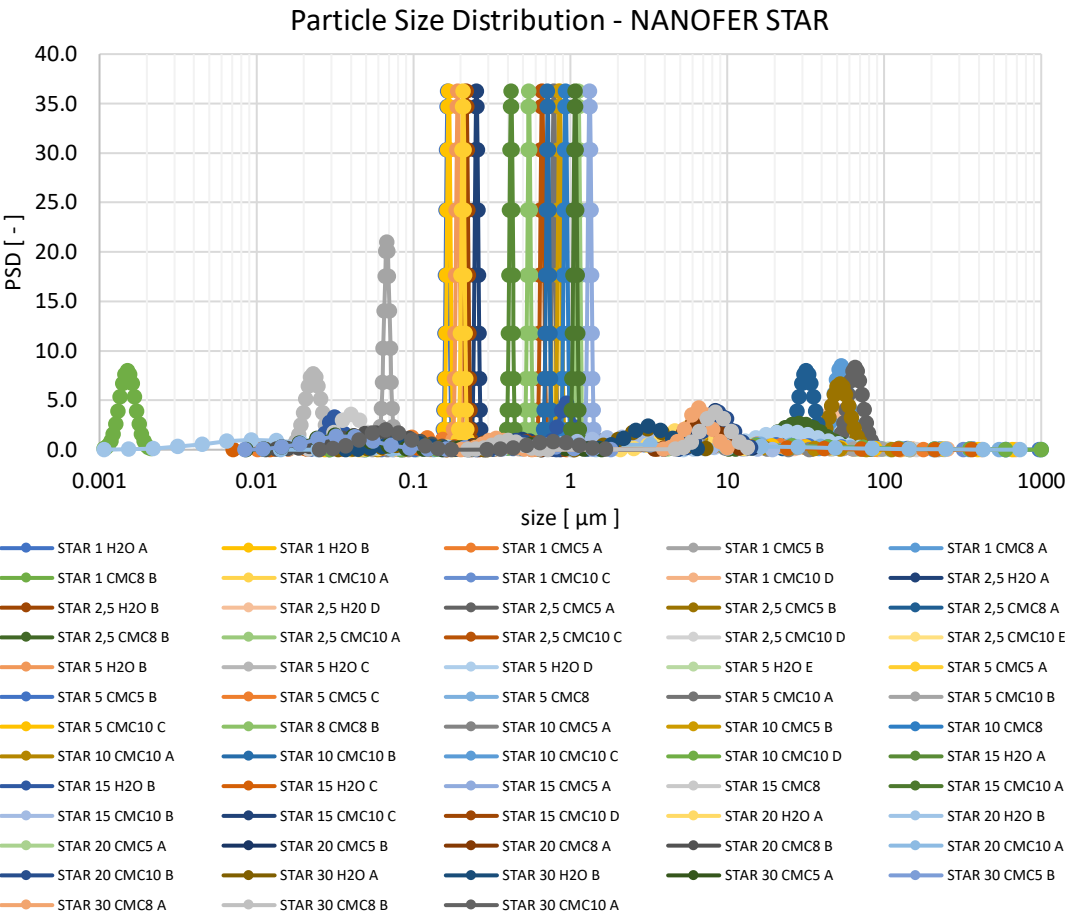
Graph A 1 Results of sedimentation test with hot samples

Table A 1 Times in which the NANOFER STAR concentrations halved during the sedimentation tests

STAR conc. [g/L]	T _{1/2} [min.]
2.5	15.9
6.5	4.3
10	3.3
20	11.3

Particle size distribution

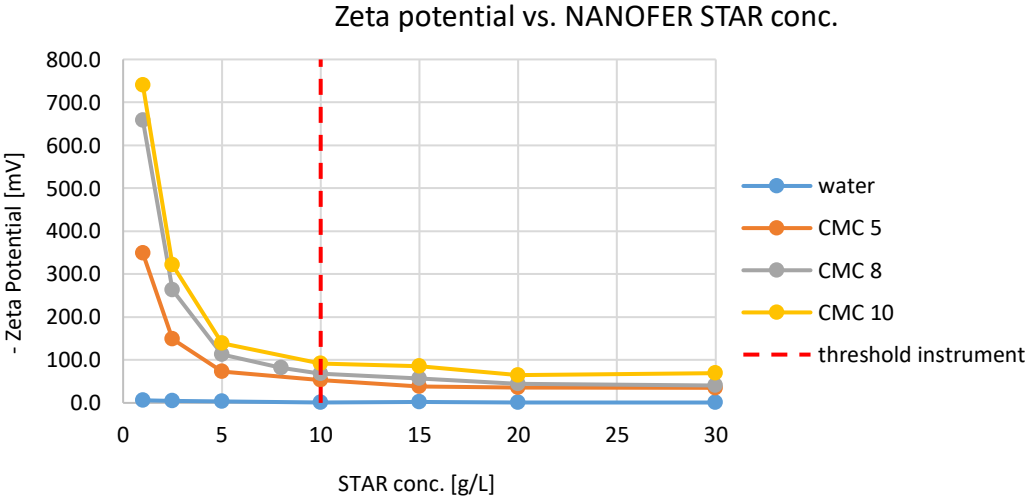
Several other measurements have been carried out with the acoustic spectrometer; however, the proximity to the instrumental accuracy threshold, caused high fitting errors between experimental data and theoretical models of the instrument; all the experimental data are reported in the following:



Graph A 2 PSD curves given by the acoustic-electroacoustic spectrometer, including the results with low reliability

Zeta potential

All the measurements of zeta potential are reported below, even those performed underneath the instrumental accuracy threshold.



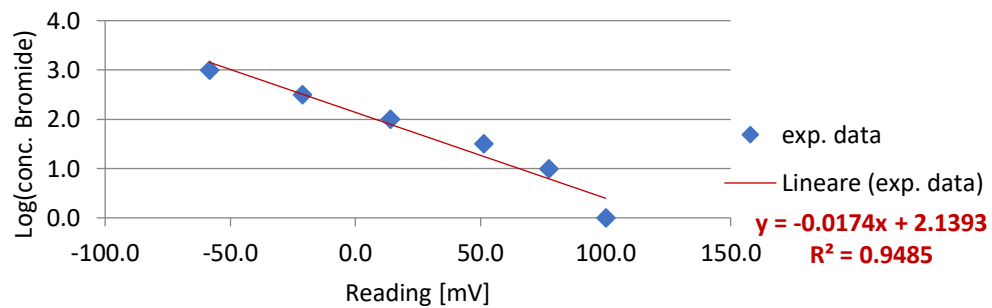
Graph A 3 Zeta potentials given by the acoustic-electroacoustic spectrometer, including the results with low reliability

Porous medium properties

Tracer tests

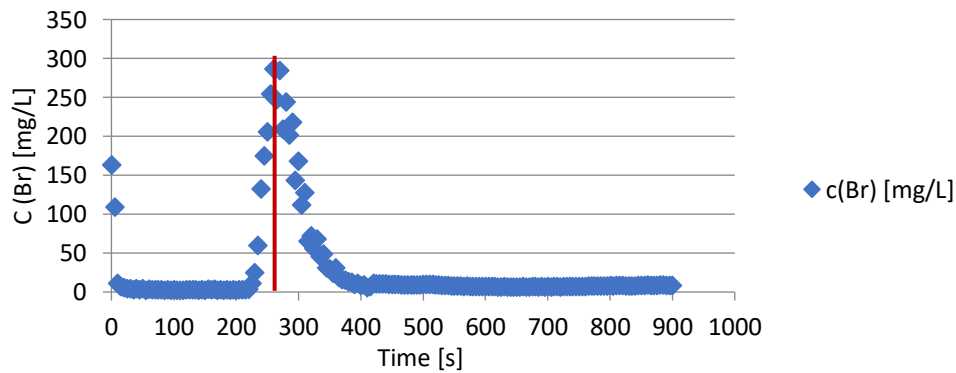
The results of tracer tests not previously shown, are reported below:

Bromide sensor calibration (C1.1 & C2.1)



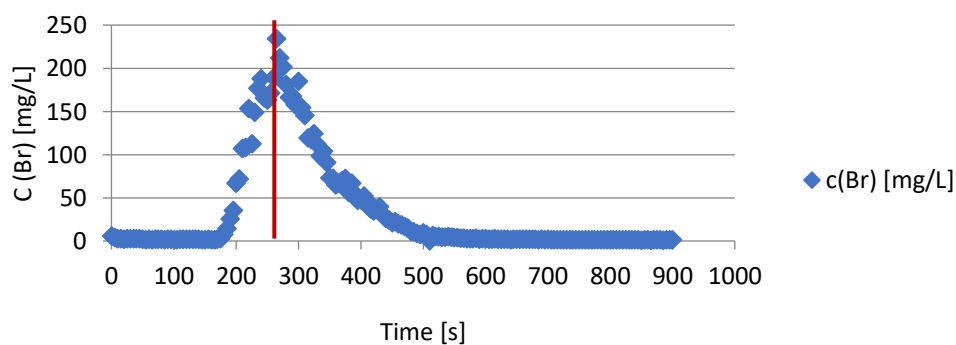
Graph A 4 Calibration of bromide sensor prior to the tracer tests of column C1.1 and C2.1

Bromide - breakthrough curve (C1.1)

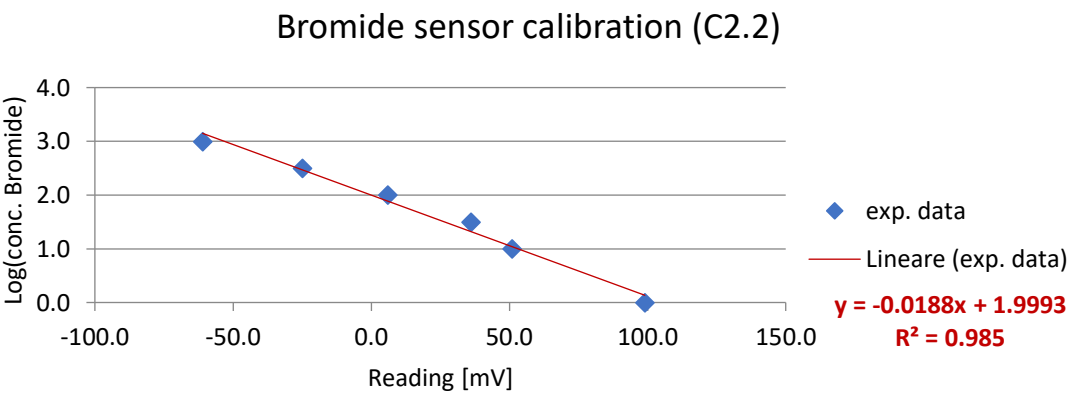


Graph A 5 Breakthrough curve of tracer test for column C1.1

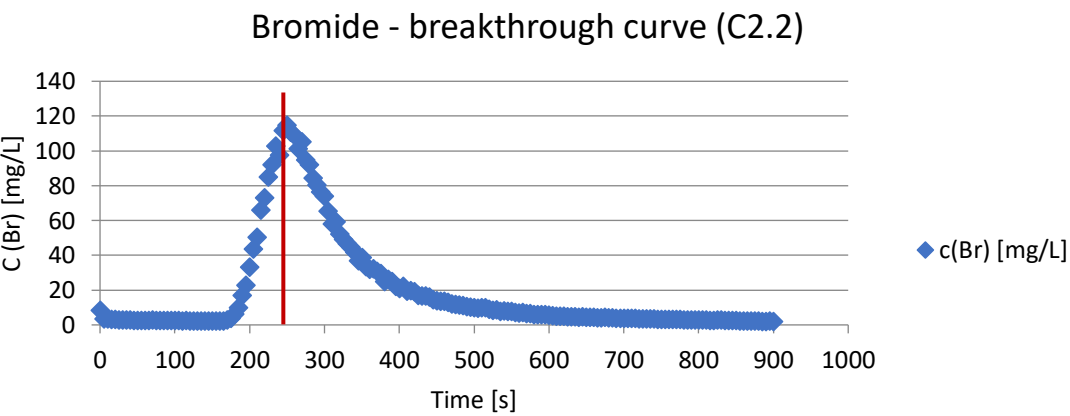
Bromide - breakthrough curve (C2.1)



Graph A 6 Breakthrough curve of tracer test for column C2.1



Graph A 7 Calibration of bromide sensor prior to the tracer test of column C.2



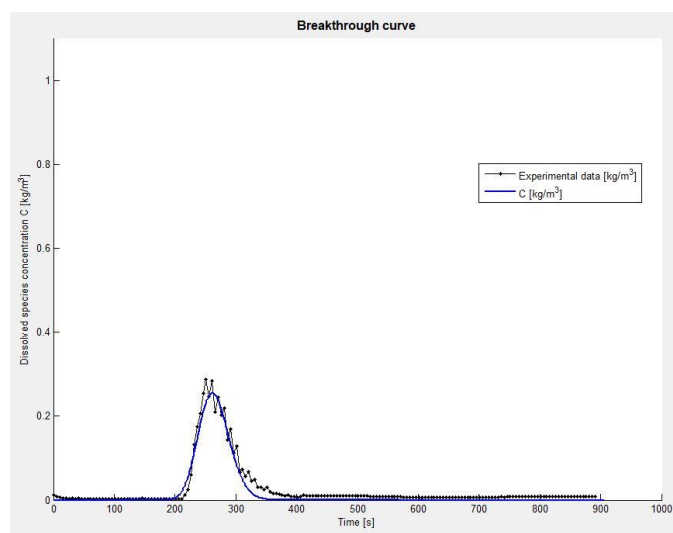
Graph A 8 Breakthrough curve of tracer test for column C2.2

Modeling with MNMs

Evaluation of tracer tests

The evaluation through MNMs of the other tracer tests is reported below.

Column C1.1:

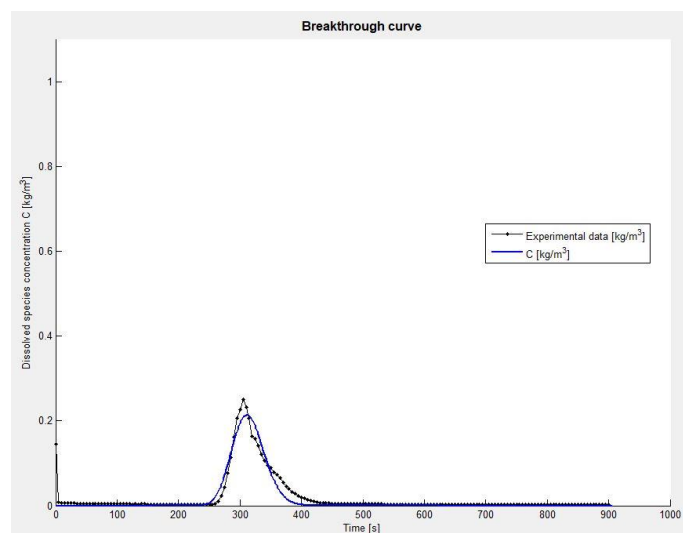


Graph A 9 Evaluation of tracer test via software, column C1.1 (MNM©, 2018)

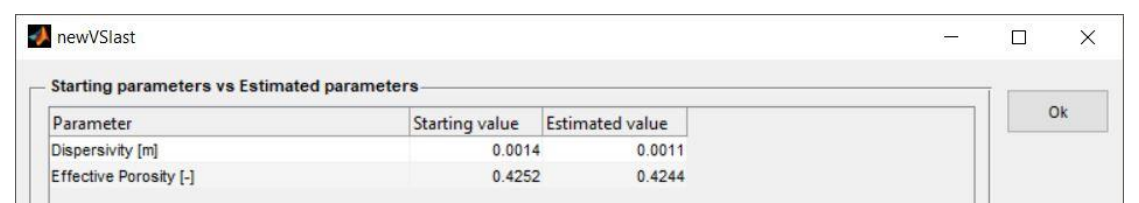
Starting parameters vs Estimated parameters			Ok
Parameter	Starting value	Estimated value	
Dispersivity [m]	0.0023	0.0013	
Effective Porosity [-]	0.3841	0.3849	

Graph A 10 Parameters estimated from the tracer test, column C1.1 (MNM©, 2018)

Column C1.2:

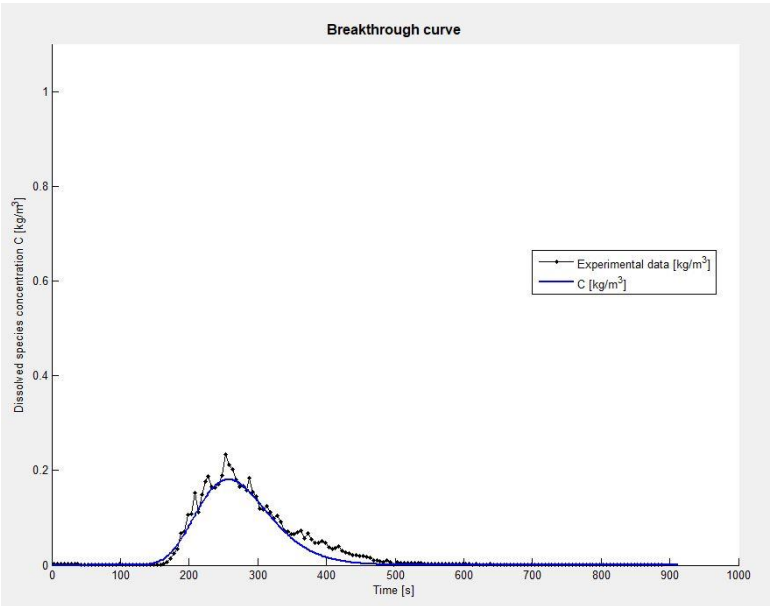


Graph A 11 Evaluation of tracer test via software, column C1.2 (MNM©, 2018)

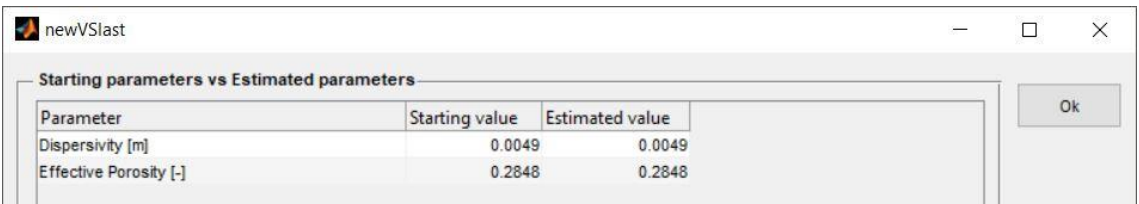


Graph A 12 Parameters estimated from the tracer test, column C1.2 (MNM_s©, 2018)

Column C2.1:



Graph A 13 Evaluation of tracer test via software, column C2.1 (MNM_s©, 2018)



Graph A 14 Parameters estimated from the tracer test, column C2.1 (MNM_s©, 2018)

Simulation of field application in radial geometry

The simulated pressure drops occurring in VEGAS sand during the injection of 6.5 g/L NANOER STAR in 10 g/L and 40 g/L CMC for 180 minutes, are shown below:

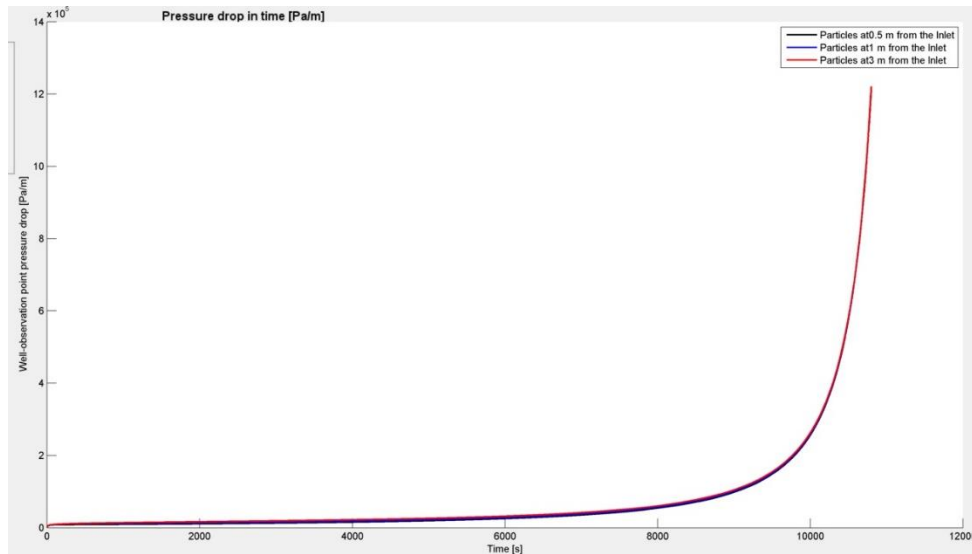


Figure A 1 Simulated pressure drop at 0.5, 1 and 3 meters from the center of the well during the injection of a suspension of 6.5 g/L of NANOER STAR and 10 g/L CMC in VEGAS sand, with flow rate equals to 120 L/min

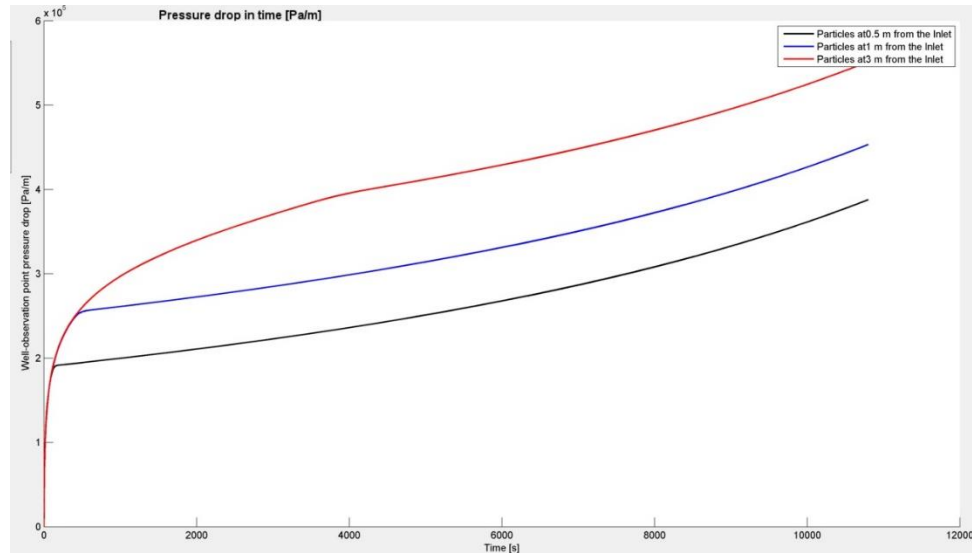


Figure A 2 Simulated pressure drop at 0.5, 1 and 3 meters from the center of the well during the injection of a suspension of 6.5 g/L of NANOER STAR and 40 g/L CMC in VEGAS sand, with flow rate equals to 120 L/min

References

- Accolla, S. (2017). *Mechanisms to investigate the transport of different nano iron particles in porous media*. Master's thesis. Politecnico di Torino, Torino.
- American Meteorological Society. (2012). *Glossary of Meteorology - breakthrough curve*. Retrieved February 18, 2018, from Meteorology Glossary: <http://glossary.ametsoc.org>
- ANSYS Fluent. (n.d.). *Viscosity for Non-Newtonian Fluids*. Retrieved March 5, 2018, from SharcNet website: www.sharcnet.ca
- Arnold, W. A., & Roberts, A. L. (2000). Pathways and kinetics of chlorinated ethylene and chlorinated acetylene reaction with Fe (0) particles. *Environmental Science & Technology*, 34(9), pp. 1794-1805.
- ATSDR - Agency for Toxic Substances and Disease Registry. (2018). Retrieved January 20, 2018, from ATSDR website: www.atsdr.cdc.gov
- Bai, F., Yang, X., Yin, A., & Zeng, G. (2014). Modified Cross model for predicting long-term creep behavior of sand asphalt. *Construction and Building Materials*, 65, pp. 43-50.
- Barnes, K. (n.d.). *What is the Steric Effect in Organic Chemistry? - Definition & Examples*. Retrieved January 26, 2018, from Study.com website: www.study.com
- Benchabane, A., & Bekkour, K. (2008). Rheological properties of carboxymethyl cellulose (CMC) solutions. *Colloid and Polymer Science*, 286(10), p. 1173.
- Bianco, C., Tosco, T., & Sethi, R. (2018). MNMs 2018, Micro- and Nanoparticles transport, filtration and clogging Model - Suite. *MNMs 2018 user manual*.
- Bird, R. B. (2002). Transport phenomena. *Applied Mechanics Reviews*, 55(1), pp. R1-R4.
- Bonet, M., Quijada, C., Muñoz, S., & Cases, F. (2005). The roles of the degree of substitution and the degree of polymerization on the behaviour of cellulose ethers applied as adhesives for artwork conservation. *Journal of adhesion science and technology*, 19(2), pp. 95-108.
- Bradford, S. A., Simunek, J., Bettahar, M., van Genuchten, M. T., & Yates, S. R. (2003). Modeling colloid attachment, straining, and exclusion in saturated porous media. *Environmental science & technology*, 37(10), pp. 2242-2250.
- Chen, X., Ji, D., Wang, X., & Zang, L. (2017). Review on Nano zerovalent Iron (nZVI): From Modification to Environmental Applications. *IOP Conference Series: Earth and Environmental Science*, 51(1).
- Christiansen, C. M., Damgaard, I., Broholm, M., Kessler, T., Klint, K. E., Nilsson, B., & Bjerg, P. L. (2010). Comparison of delivery methods for enhanced in situ remediation in clay till. *Groundwater Monitoring & Remediation*, 30(4), pp. 107-122.
- CityChlor. (2013). *In-situ Chemical Reduction using Zero-valent Iron injection - A technique for the remediation of source zones*. Retrieved January 30, 2018, from <https://rwsenvironment.eu>
- Comba, S., & Braun, J. (2012). A new physical model based on cascading column experiments to reproduce the radial flow and transport of micro-iron particles. *Journal of contaminant hydrology*, 140, pp. 1-11.
- CPS Instruments Europe. (n.d.). *CPS Instruments - Disc Centrifuge*. Retrieved February 23, 2018, from CPS Instruments website: www.cpsinstruments.eu
- Crane, R. A., & Scott, T. B. (2012). Nanoscale zero-valent iron: future prospects for an emerging water treatment technology. *Journal of hazardous materials*, 211, pp. 112-125.
- C-vac. (n.d.). Retrieved February 19, 2018, from C-vac website: www.c-vac.com
- Cwiertny, D. M., Handler, R. M., Schaefer, M. V., Grassian, V. H., & Scherer, M. M. (2008). Interpreting nanoscale size-effects in aggregated Fe-oxide suspensions: reaction of Fe (II) with goethite. *Geochimica et Cosmochimica Acta*, 72(5), pp. 1365-1380.

References

- Dalla Vecchia, E., Luna, M., & Sethi, R. (2009). Transport in porous media of highly concentrated iron micro-and nanoparticles in the presence of xanthan gum. *Environmental Science & Technology*, 43(23), pp. 8942-8947.
- De Vicente, J., Delgado, A. V., Plaza, R. C., Durán, J. D., & González-Caballero, F. (2000). Stability of cobalt ferrite colloidal particles. Effect of pH and applied magnetic fields. *Langmuir*, 16(21), pp. 7954-7961.
- Debye, P. (1933). A method for the determination of the mass of electrolytic ions. *The Journal of Chemical Physics*, 1(1), pp. 13-16.
- Di Molfetta, A., & Sethi, R. (2012). *Ingegneria degli acquiferi*. Italy: Springer. doi:10.1007/978-88-470-1851-8
- Dispersion Technology Inc. (n.d.). *DT - Dispersion Technology. MODEL DT-1202*. Retrieved February 23, 2018, from DT website: www.dispersion.com
- Dukhin, A. S., & Goetz, P. J. (2001). Acoustic and electroacoustic spectroscopy for characterizing concentrated dispersions and emulsions. *Advances in Colloid and Interface Science*, 92(1-3), pp. 73-132.
- Dukhin, A. S., & Goetz, P. J. (2010). *Characterization of liquids, nano-and microparticulates, and porous bodies using ultrasound* (Vol. 24). Elsevier.
- Elimelech, M., Gregory, J., & Jia, X. (2013). *Particle deposition and aggregation: measurement, modelling and simulation*. Butterworth-Heinemann.
- EPA. (1996). *Pump-and-Treat Ground-Water Remediation: A Guide for Decision Makers and Practitioners*. Office of Research and Development, Washington DC.
- FAO monograph. (1992). *FAO - Food and Agriculture Organization of the United States. SODIUM CARBOXYMETHYL CELLULOSE*. Retrieved February 20, 2018, from FAO website: www.fao.org
- Fetter, C. W., Boving, T., & Kremer, D. (2017). *Contaminant Hydrogeology* (Third Edition ed.). United States of America: Waveland Press, Inc.
- Fitts, D. D. (1966). Statistical mechanics: a study of intermolecular forces. *Annual Review of Physical Chemistry*, 17(1), pp. 59-82.
- Frieser-München. (2011). *Dorfner Dorsilit®8 FG 0,3-0,8 mm - Technisches datenblatt*. Retrieved February 22, 2018, from Frieser-München GmbH website: www.frieser-muenchen.de
- Furakawa, Y., Kim, J. W., Watkins, J., & Wilkin, R. T. (2002). Formation of ferrihydrite and associated iron corrosion products in permeable reactive barriers of zero-valent iron. *Environmental Science & Technology*, 36(24), pp. 5469-5475.
- Gastone, F., Tosco, T., & Sethi, R. (2014a). Guar gum solutions for improved delivery of iron particles in porous media (Part 1): Porous medium rheology and guar gum-induced clogging. *Journal of contaminant hydrology*, 166, pp. 23-33.
- Gastone, F., Tosco, T., & Sethi, R. (2014b). Green stabilization of microscale iron particles using guar gum: bulk rheology, sedimentation rate and enzymatic degradation. *Journal of colloid and interface science*, 421, pp. 33-43.
- Geoprobe Systems. (n.d.). *Geoprobe Machines*. Retrieved January 19, 2018, from Geoprobe website: www.geoprobe.com
- Ghali, E. (2010). *Corrosion resistance of aluminum and magnesium alloys: understanding, performance, and testing* (Vol. 12). John Wiley & Sons.
- Giannelli, G. (2014). *Small Flume Experiment for the Transport Evaluation of Carbo-Iron Particles in a Confined Aquifer*. Master's thesis. Politecnico di Torino, Torino.
- Giotti, F. (2017). *Determination of key parameters controlling transport and reactivity of metal particles for groundwater remediation*. Master's thesis. Politecnico di Torino, Torino.
- Grieger, K. D., Fjordbøge, A., Hartmann, N. B., Eriksson, E., Bjerg, P. L., & Baun, A. (2010). Environmental benefits and risks of zero-valent iron nanoparticles (nZVI) for in situ

- remediation: risk mitigation or trade-off? *Journal of Contaminant Hydrology*, 118(3-4), pp. 165-183.
- Hamby, D. M. (1996). Site remediation techniques supporting environmental restoration activities—a review. *Science of the Total Environment*, 191(3), pp. 203-224.
- He, F., Zhang, M., Qian, T., & Zhao, D. (2009). Transport of carboxymethyl cellulose stabilized iron nanoparticles in porous media: Column experiments and modeling. *Journal of colloid and interface science*, 334(1), pp. 96-102.
- Helmenstine, A. M. (2017). *Adsorption Definition*. Retrieved January 26, 2018, from ThoughtCo. website: www.thoughtco.com
- Helmholtz, H. V. (1853). Ueber einige Gesetze der Vertheilung elektrischer Ströme in körperlichen Leitern mit Anwendung auf die thierisch-elektrischen Versuche. *Annalen der Physik*, 165(6), pp. 211-233.
- Herbillon, A. J. (1988). Introduction to the surface charge properties of iron oxides and oxidic soils. In J. W. Stucki, B. A. Goodman, & U. Schwertmann, *Iron in Soils and Clay Minerals. NATO ASI Series* (Vol. 217). Springer, Dordrecht. doi:10.1007/978-94-009-4007-9_10
- Hetterschijt, R. A., Stroet, C. T., & Bosma, T. N. (2000). Estimation of sequential degradation rates of perchloroethylene by "history matching". *IAHS PUBLICATION*, 468-473.
- Hollabaugh, C. B., Burt, L. H., & Walsh, A. P. (1945). Carboxymethylcellulose. Uses and applications. *Industrial & Engineering Chemistry*, 37(10), pp. 943-947.
- Huling, S. G., & Weaver, J. W. (1991). *Ground water issue: dense nonaqueous phase liquids*. US Environmental Protection Agency.
- IARC - International Agency for Research on Cancer. (2018). Retrieved January 20, 2018, from IARC website: <http://monographs.iarc.fr/ENG/Classification>
- Indian Institute of Technology. (n.d.). *IIT - Lecture: Hydraulic Conductivity*. Retrieved from Indian Institute of Technology (Banaras Hindu University), Varanasi: www.iitbhu.ac.in
- Israelachvili, J. N. (2011). *Intermolecular and surface forces*. Academic press.
- Jang, M. H., Lim, M., & Hwang, Y. S. (2014). Potential environmental implications of nanoscale zero-valent iron particles for environmental remediation. *Environmental health and toxicology*, 29.
- Kruczek, B. (2014). Carman–Kozeny Equation. In E. Drioli, & L. Giorno, *Encyclopedia of Membranes*. Berlin, Heidelberg: Springer.
- Kueper, B. H., Stroo, H. F., Vogel, C. M., & Ward, C. H. (2014). *Chlorinated solvent source zone remediation*. Springer.
- LAR - Process Analysers AG. (n.d.). *Total Organic Carbon (TOC)*. Retrieved February 15, 2018, from LAR website: www.lar.com
- Lin, Y. H., Tseng, H. H., Wey, M. Y., & Lin, M. D. (2010). Characteristics of two types of stabilized nano zero-valent iron and transport in porous media. *Science of the Total Environment*, 408(10), pp. 2260-2267.
- Logan, B. E. (2012). *Environmental transport processes*. John Wiley & Sons.
- Logan, B. E., Jewett, D. G., Arnold, R. G., Bouwer, E. J., & O'Melia, C. R. (1995). Clarification of clean-bed filtration models. *Journal of Environmental Engineering*, 121(12), pp. 869-873.
- London, F. (1930). Zur theorie und systematik der molekularkräfte. *Zeitschrift für Physik*, 63(3-4), pp. 245-279.
- Lopez, X., Valvatne, P. H., & Blunt, M. J. (2003). Predictive network modeling of single-phase non-Newtonian flow in porous media. *Journal of Colloid and Interface Science*, 264(1), pp. 256-265.
- Malvern Instruments. (2015). *Zeta potential - An introduction in 30 minutes*. Malvern. Retrieved January 30, 2018, from www.malvern.com
- Malvern Instruments. (n.d.). *Malvern - Zetasizer Nano Range*. Retrieved February 23, 2018, from Malvern website: www.malvern.com/en

References

- McNaught, A. D., & Wilkinson, A. (1997). *IUPAC Compendium of Chemical Terminology* ("Gold Book"). Cambridge, UK: Royal Society of Chemistry.
- Mercer, J. W., Skipp, D. C., & Giffin, D. (1990). *Basics of pump-and-treat ground-water remediation technology*. Ada OK 74820: US Environmental Protection Agency.
- Messina, F., Marchisio, D. L., & Sethi, R. (2015). An extended and total flux normalized correlation equation for predicting single-collector efficiency. *Journal of colloid and interface science*, 446, pp. 185-193.
- Mezger, T. G. (2015). *Applied Rheology: With Joe Flow on Rheology Road*. Anton Paar.
- Miyajima, K. (2015). *Taking Nanotechnological Remediation Processes from Lab Scale to End User Applications for the Restoration of a Clean Environment*. WP8: Up-Scaling, Risk and Sustainability. NanoRem.
- MNMs©. (2018). Micro- and Nanoparticles transport, filtration and clogging Model - Suite. *Software*.
- Moraci, N., & Calabrò, P. S. (2010). Heavy metals removal and hydraulic performance in zero-valent iron/pumice permeable reactive barriers. *Journal of Environmental Management*, 91(11), pp. 2336-2341.
- Mueller, N. B., & Nowack, B. (2010). Nanoparticles for remediation: solving big problems with little particles. *Elements*, 6(6), pp. 395-400.
- Mueller, N. C., Braun, J., Bruns, J., Černík, M., Rissing, P., Rickerby, D., & Nowack, B. (2012). Application of nanoscale zero valent iron (NZVI) for groundwater remediation in Europe. *Environmental Science and Pollution Research*, 19(2), pp. 550-558.
- Mumford, K. A., Rayner, J. L., Snape, I., & Stevens, G. W. (2014). Hydraulic performance of a permeable reactive barrier at Casey Station, Antarctica. *Chemosphere*, 117, pp. 223-231.
- NANO IRON s.r.o. - NANO FER STAR manual. (n.d.). *NANO IRON FUTURE TECHNOLOGY - Manual for preparation of an aqueous suspension from dry stabilized iron*. Retrieved February 21, 2018, from NANO IRON website: <http://nanoiron.cz/en>
- NANO IRON s.r.o. (n.d.). *NANO IRON FUTURE TECHNOLOGY - Zero-Valent Iron Nanoparticles (NZVI)*. Retrieved February 21, 2018, from NANO IRON website: <http://nanoiron.cz/en>
- NanoRem. (n.d.). Retrieved January 08, 2018, from NanoRem website: www.nanorem.eu
- National Research Council. (1984). *Groundwater Contamination*. Washington, DC: The National Academies Press. doi:10.17226/1770
- National Science Foundation. (2018, January 21). *Oxidation-Reduction Reactions*. Retrieved from Chemistry - LibreTexts website: <https://chem.libretexts.org>
- Ninham, B. W., & Parsegian, V. A. (1970). Van der Waals forces: special characteristics in lipid-water systems and a general method of calculation based on the Lifshitz theory. *Biophysical journal*, 10(7), pp. 646-663.
- Obiri-Nyarko, F., Grajales-Mesa, S. J., & Malina, G. (2014). An overview of permeable reactive barriers for in situ sustainable groundwater remediation. *Chemosphere*, 111, pp. 243-259.
- Orth, W. S., & Gillham, R. W. (1995). Dechlorination of trichloroethene in aqueous solution using Fe⁰. *Environmental Science & Technology*, 30(1), pp. 66-71.
- Parker, E. A., Rippey, M. A., Mehring, A. S., Winfrey, B. K., Ambrose, R. F., Levin, L. A., & Grant, S. B. (2017). Predictive Power of Clean Bed Filtration Theory for Fecal Indicator Bacteria Removal in Stormwater Biofilters. *Environmental Science & Technology*, 51(10), pp. 5703-5712.
- Particle Analytical. (n.d.). *Particle Analytical - Analysis for the Pharmaceutical Industry*. BET. Retrieved February 22, 2018, from Particle Analytical website: www.particle.dk
- PEN - The Project on Emerging Nanotechnologies. (n.d.). Retrieved January 08, 2018, from PEN website: www.nanotechproject.org

- Phenrat, T., Saleh, N., Sirk, K., Tilton, R. D., & Lowry, G. V. (2007). Aggregation and sedimentation of aqueous nanoscale zerovalent iron dispersions. *Environmental Science & Technology*, 41(1), pp. 284-290.
- Physica - a Company by Antoon Paar. (n.d.). *Anton Paar - Viscometer; Technical Specification*. Retrieved February 24, 2018, from Anton Paar website: www.anton-paar.com
- Powell, R. M., Blowes, D. W., Gillham, R. W., Schultz, D., Sivavec, T., Puls, R. W., . . . Landis, R. (1998). *Permeable Reactive Barrier Technologies for Contaminant Remediation*. US Environmental Protection Agency.
- Prakash, S., & Yeom, J. (2014). *Nanofluidics and microfluidics: systems and applications*. William Andrew.
- Purdue University. (n.d.). *Purdue Science - London Dispersion Forces*. Retrieved February 2, 2018, from Purdue University - Department of Chemistry website: www.chem.purdue.edu
- QUARZSANDE. (2012). *QUARZSANDE DORSILIT® Nr. 8 - Produktdatenblatt*. Retrieved February 22, 2018, from QUARZSANDE website: www.quarzsande.at
- Quinn, J., Geiger, C., Clausen, C., Brooks, K., Coon, C., O'Hara, S., & Holdsworth, T. (2005). Field demonstration of DNAPL dehalogenation using emulsified zero-valent iron. *Environmental Science & Technology*, 39(5), pp. 1309-1318.
- Rad, N. S., & Tumay, M. T. (1987). Factors affecting sand specimen preparation by raining. *Geotechnical Testing Journal*, 10(1), pp. 31-37.
- Raychoudhury, T., Tufenkji, N., & Ghoshal, S. (2012). Aggregation and deposition kinetics of carboxymethyl cellulose-modified zero-valent iron nanoparticles in porous media. *Water research*, 46(6), pp. 1735-1744.
- RheoSense - Simply Precise. (n.d.). *Viscosity of Newtonian and non-Newtonian Fluids*. Retrieved March 2, 2018, from RheoSense website: www.rheosense.com
- Saberinasr, A., Rezaei, M., Nakhaei, M., & Hosseini, S. M. (2016). Transport of CMC-Stabilized nZVI in Saturated Sand Column: the Effect of Particle Concentration and Soil Grain Size. *Water, Air, & Soil Pollution*, 227(10), p. 394.
- Saleh, N., Kim, H. J., Phenrat, T., Matyjaszewski, K., Tilton, R. D., & Lowry, G. V. (2008). Ionic strength and composition affect the mobility of surface-modified Fe⁰ nanoparticles in water-saturated sand columns. *Environmental Science & Technology*, 42(9), pp. 3349-3355.
- Schlimm, C., & Heitz, E. (1996). Development of a wastewater treatment process: reductive dehalogenation of chlorinated hydrocarbons by metals. *Environmental Progress & Sustainable Energy*, 15(1), pp. 38-47.
- Shannazari, D. (2015). *Optimization of the Migration Properties of Nanofer 25s Nanoparticles in Porous Media using Cascading Columns*. Master's thesis. Universität Stuttgart, Stuttgart.
- Solomon, T. (2001). The definition and unit of ionic strength. *Journal of Chemical Education*, 78(12), p. 1691.
- SPE International. (2015). *PetroWiki - Estimating permeability based on Kozeny-Carman equation*. Retrieved February 28, 2018, from PetroWiki website: www.petrowiki.org
- St. Petersburg State University. (n.d.). *Zeta potential measurement principle (Laser Doppler Electrophoresis)*. Retrieved February 23, 2018, from Center for optical and laser materials: www.laser.spbu.ru/en
- StreamSim Technologies, Inc. (n.d.). *History Matching - What is History Matching?* Retrieved January 20, 2018, from StreamSim website: www.streamsim.com
- Sun, Y. P., Li, X. Q., Cao, J., Zhang, W. X., & Wang, H. P. (2006). Characterization of zero-valent iron nanoparticles. *Advances in colloid and interface science*, 120(1-3), pp. 47-56.
- Suresh, S. (2009). Reductive remediation of pollutants using metals. *Open Waste Management Journal*, 2, pp. 6-16.

References

- Suthersan, S. S., Horst, J., Schnobrich, M., Welty, N., & McDonough, J. (2016). *Remediation engineering: design concepts*. CRC Press.
- The DOW Chemical Company. (n.d.). *DOW - Carboxymethylcellulose*. Retrieved February 20, 2018, from DOW website: www.dow.com
- Tiraferrri, A., & Sethi, R. (2009). Enhanced transport of zerovalent iron nanoparticles in saturated porous media by guar gum. *Journal of Nanoparticle Research*, 11(3), p. 635.
- Tiraferrri, A., Tosco, T., & Sethi, R. (2011). Transport and retention of microparticles in packed sand columns at low and intermediate ionic strengths: experiments and mathematical modeling. *Environmental Earth Sciences*, 63(4), pp. 847-859.
- Tosco, T., & Sethi, R. (2009). MNM1D: A numerical code for colloid transport in porous media: Implementation and validation. *American Journal of Environmental Sciences*, 5(4), pp. 516-524.
- Tosco, T., & Sethi, R. (2010). Transport of non-Newtonian suspensions of highly concentrated micro-and nanoscale iron particles in porous media: a modeling approach. *Environmental science & technology*, 44(23), pp. 9062-9068.
- Tosco, T., Gastone, F., & Sethi, R. (2014). Guar gum solutions for improved delivery of iron particles in porous media (Part 2): Iron transport tests and modeling in radial geometry. *Journal of contaminant hydrology*, 166, pp. 34-51.
- Tosco, T., Papini, M. P., Viggi, C. C., & Sethi, R. (2014). Nanoscale zerovalent iron particles for groundwater remediation: a review. *Journal of Cleaner Production*, 77, pp. 10-21.
- Tosco, T., Tiraferrri, A., & Sethi, R. (2009). Ionic strength dependent transport of microparticles in saturated porous media: Modeling mobilization and immobilization phenomena under transient chemical conditions. *Environmental Science & Technology*, 43(12), pp. 4425-4431.
- US EPA. (2004). *Cleaning up the nation's waste sites: markets and technology trends*. US Environmental Protection Agency.
- Velimirovic, M., Tosco, T., Uyttebroek, M., Luna, M., Gastone, F., De Boer, C., & Braun, J. (2014). Field assessment of guar gum stabilized microscale zerovalent iron particles for in-situ remediation of 1, 1, 1-trichloroethane. *Journal of contaminant hydrology*, 164, pp. 88-99.
- Xue, D., & Sethi, R. (2012). Viscoelastic gels of guar and xanthan gum mixtures provide long-term stabilization of iron micro-and nanoparticles. *Journal of nanoparticle research*, 14(11), p. 1239.
- Yang, J., Meng, L., & Guo, L. (2017). In situ remediation of chlorinated solvent-contaminated groundwater using ZVI/organic carbon amendment in China: field pilot test and full-scale application. *Environmental Science and Pollution Research*, pp. 1-12.
- Yao, K. M., Habibian, M. T., & O'Melia, C. R. (1971). Water and waste water filtration. Concepts and applications. *Environmental science & technology*, 5(11), pp. 1105-1112.
- Yu, R. F., Chen, H. W., Cheng, W. P., Lin, Y. J., & Huang, C. L. (2014). Monitoring of ORP, pH and DO in heterogeneous Fenton oxidation using nZVI as a catalyst for the treatment of azo-dye textile wastewater. *Journal of the Taiwan Institute of Chemical Engineers*, 45(3), pp. 947-954.
- Zeng, Z., & Grigg, R. (2006). A criterion for non-Darcy flow in porous media. *Transport in porous media*, 63(1), pp. 57-69.
- Zhang, W. X. (2003). Nanoscale iron particles for environmental remediation: an overview. *Journal of nanoparticle Research*, 5(3-4), pp. 323-332.
- Ziegler, G. J. (1989). Remediation through groundwater recovery treatment. *Pollution Engineering*, 21(7), pp. 75-79.